

University of Windsor

Scholarship at UWindor

Electronic Theses and Dissertations

Theses, Dissertations, and Major Papers

11-7-2015

Ferritic Nitrocarburizing of Plain Carbon Steels

Madhavan Manivannan
University of Windsor

Follow this and additional works at: <https://scholar.uwindsor.ca/etd>

Recommended Citation

Manivannan, Madhavan, "Ferritic Nitrocarburizing of Plain Carbon Steels" (2015). *Electronic Theses and Dissertations*. 5486.

<https://scholar.uwindsor.ca/etd/5486>

This online database contains the full-text of PhD dissertations and Masters' theses of University of Windsor students from 1954 forward. These documents are made available for personal study and research purposes only, in accordance with the Canadian Copyright Act and the Creative Commons license—CC BY-NC-ND (Attribution, Non-Commercial, No Derivative Works). Under this license, works must always be attributed to the copyright holder (original author), cannot be used for any commercial purposes, and may not be altered. Any other use would require the permission of the copyright holder. Students may inquire about withdrawing their dissertation and/or thesis from this database. For additional inquiries, please contact the repository administrator via email (scholarship@uwindsor.ca) or by telephone at 519-253-3000ext. 3208.

Ferritic Nitrocarburizing of Plain Carbon Steels

By

Madhavan Manivannan

A Dissertation
Submitted to the Faculty of Graduate Studies
through the Department of **Mechanical, Automotive and Materials Engineering**
in Partial Fulfillment of the Requirements for
the Degree of **Doctor of Philosophy**
at the University of Windsor

Windsor, Ontario, Canada

2015

© 2015 Madhavan Manivannan

Ferritic Nitrocarburizing of Plain Carbon Steels

by

Madhavan Manivannan

APPROVED BY:

K. Li, External Examiner
Oakland University

J. Johrendt
Department of Mechanical, Automotive and Materials Engineering

R.J. Bowers
Department of Mechanical, Automotive and Materials Engineering

W. Altenhof
Department of Mechanical, Automotive and Materials Engineering

D. O. Northwood, Co-Advisor
Department of Mechanical, Automotive and Materials Engineering

V. Stoilov, Co-Advisor
Department of Mechanical, Automotive and Materials Engineering

13th May 2015

DECLARATION OF CO-AUTHORSHIP / PREVIOUS PUBLICATION

This dissertation includes [4] original papers that have been previously published/submitted for publication in peer reviewed journals, as follows:

Dissertation Chapter	Publication title/full citation	Publication status
Chapter 4,5	<i>Finite Element Simulations of Geometric Distortions in Ferritic Nitrocarburized SAE 1010 Plain Carbon Steel/Manivannan, M., Stoilov, V., and Northwood, D.O., Proceedings of the 5th International Conference on Thermal Process Modeling and Computer Simulation, pp. 139-144, June 16, 2014, Orlando, FL, USA</i>	“published”
Chapter 4,5	<i>The Use of Navy C-rings to Study, and Predict, Distortion in Heat Treated Components: Experimental Measurements and Computer Modeling/Manivannan, M., Northwood, D.O., and Stoilov, V., 2014, International Heat Treatment and Surface Engineering, 8(4), pp. 168-175</i>	“published”
Chapter 6	<i>Ferritic Nitrocarburizing of SAE 1010 Plain Carbon Steel Parts/Manivannan, M., Stoilov, V., and Northwood, D.O., 2015, SAE International Journal of Materials and Manufacturing, 8(2), pp. 482-486</i>	“published”
Chapter 6	<i>Numerical Model of the Ferritic Nitrocarburizing of SAE 1010 Plain Carbon Steel/Manivannan, M., Stoilov, V., and Northwood, D.O., European Conference on Heat Treatment 2015 & 22nd IFHTSE Congress, May 20-22, 2015, Venice, Italy</i>	“published”

I hereby declare this dissertation incorporates the outcome of a joint research under the supervision of Dr. Derek O. Northwood and Dr. Vesselin Stoilov. I am aware of the University of Windsor Senate Policy on Authorship and I certify that I have properly acknowledged the contribution of other researchers to my dissertation, and have obtained written permission from each of the co-authors to include the above material in my dissertation.

I certify that, with the above qualification, this dissertation, and the research to which it refers, is the product of my own work.

I certify that I have obtained a written permission from the copyright owner(s) to include the above published material(s) in my thesis. I certify that the above material describes work completed during my registration as graduate student at the University of Windsor.

I declare that, to the best of my knowledge, my dissertation does not infringe upon anyone's copyright nor violate any proprietary rights and that any ideas, techniques, quotations, or any other material from the work of other people included in my dissertation, published or otherwise, are fully acknowledged in accordance with the standard referencing practices. Furthermore, to the extent that I have included copyrighted material that surpasses the bounds of fair dealing within the meaning of the Canada Copyright Act, I certify that I have obtained a written permission from the copyright owner(s) to include such material(s) in my dissertation.

I declare that this is a true copy of my dissertation, including any final revisions, as approved by my dissertation committee and the Graduate Studies office, and that this

dissertation has not been submitted for a higher degree to any other University or Institution.

ABSTRACT

Nitrocarburizing is a case hardening process which improves the hardness and wear resistance of a component, but results in geometric distortions. Torque converter pistons (automotive component) and Navy C-ring specimens (measuring tool) made from SAE 1010 plain carbon steel were used for the distortion analysis. Navy C-rings are generally used for studying the dimensional changes of a material before analyzing the dimensional changes of the actual component. Navy C-rings of varying thicknesses were used to analyze the effect of distortions with the change in thickness. Finite element simulations of Navy C-rings and torque converter pistons were developed to study the effect of nitrocarburizing process on distortions. For thinner specimens, the predicted distortions compare favorably with the experimental values. However, the thicker C-ring specimens showed high prediction error. To better understand the prediction difference of the different C-rings and TC pistons, an empirical ratio (bulk volume to nitrocarburized volume (V/V_N)) was introduced. The V/V_N ratio will not only help to separate the nitrocarburized surface dominant and bulk dominant specimens, but also provide a better comparison of the C-ring size with the actual component.

The reduction of bulk volume to nitrocarburized volume (V/V_N) ratio led to a decrease in both the C-ring's inner diameter (ID) and gap width (GW) distortion, and a small increase in outer diameter (OD) distortion.

A composition-depth profile simulation model was also developed to predict the local distortion due to nitrocarburized phases. The local distortion results showed that the γ' -phase (Fe_4N) in the diffusion zone dominates the overall magnitude of distortion.

The residual stress distribution for 1-step nitrocarburizing treatment was successfully modeled and validated against the experimental stress. The surface stress for one-step nitrocarburizing treatment was found to be tensile in nature. This tensile (surface) residual stress was further reduced by introducing 2-step nitrocarburizing treatments.

Using the nitrogen profile model for 2-step nitrocarburizing, it was found that the additional γ' -Fe₄N phase at the surface resulted in a notable residual (tensile) stress reduction. Also, the simulated 2-step nitrocarburizing treatments produced a same level of distortion as 1-step nitrocarburizing treatments. Therefore, the proposed 2-step nitrocarburizing treatments could potentially improve both the surface quality and fatigue resistance.

DEDICATION

This dissertation is dedicated to my family

ACKNOWLEDGEMENTS

First, I would like to thank my academic supervisors, Dr. Derek O. Northwood and Dr. Vesselin Stoilov for their time, technical support and guidance during my graduate studies.

I would like to extend my thanks to the committee members, Dr. William Altenhof, Dr. Randy Bowers, and Dr. Jennifer Johrendt for their support and advice.

I would also like to acknowledge the support of Mr. Andy Jenner, and Dr. Gang Li.

Finally, the financial support of the Natural Sciences and Engineering Research Council of Canada (NSERC), the Queen Elizabeth II Graduate Scholarship in Science and Technology (QEII-GSST) program and the University of Windsor (A.R. & E.G. Ferriss Graduate Endowment Award, Dr. Ross H. Paul Scholarship) are graciously acknowledged.

TABLE OF CONTENTS

DECLARATION OF CO-AUTHORSHIP / PREVIOUS PUBLICATION..... III

ABSTRACT..... VI

DEDICATION..... VIII

ACKNOWLEDGEMENTS IX

LIST OF TABLES XIV

LIST OF FIGURES XVI

LIST OF APPENDICES XXIV

LIST OF ABBREVIATIONS/SYMBOLS..... XXV

NOMENCLATURE..... XXVI

CHAPTER 1 INTRODUCTION.....1

1.1 Research Objectives and Approach.....3

1.2 Dissertation Outline.....3

CHAPTER 2 LITERATURE REVIEW.....5

2.1 Ferritic Nitrocarburizing (FNC).....5

2.1.1 Ion or plasma nitrocarburizing9

2.1.2 Fluidized bed nitrocarburizing.....10

2.1.3 Salt bath nitrocarburizing11

2.1.4 Gas nitrocarburizing13

2.1.5 Vacuum nitrocarburizing.....	14
2.2 Residual stress	15
2.3 Distortion.....	19
2.3.1 Distortion prevention methods	22
2.4 Types and use of Navy C-rings	23
2.5 Modeling	27
2.5.1 Distortion modeling.....	30
2.5.2 Composition-Depth profiles: experimental and modeling	37
2.5.3 Residual Stress Modeling	43
CHAPTER 3 ANALYTICAL APPROACH	47
3.1 Distortion reduction.....	48
3.1.1 Navy C-ring geometry	49
3.1.2 Materials.....	49
3.1.4 Heat treatment conditions	51
3.1.5 Sample preparation and optical microscopy.....	52
3.1.6 Nano-indentation measurements	53
3.1.7 Experimental distortion measurements	54
3.1.8 Numerical (FEM) distortion prediction	55
3.1.9 Composition-depth profile numerical simulation.....	56
3.1.10 Composition-depth profile measurements (experimental)	57

3.2 Reduction in surface residual stress	58
CHAPTER 4 NUMERICAL SIMULATIONS FOR NAVY C-RINGS AND TORQUE CONVERTER PISTONS	59
4.1 Material Properties.....	59
4.2 Navy C-ring Probe.....	60
4.3 Navy C-ring Finite Element Models	61
4.3.1 Boundary Conditions.....	62
4.3.2 Discretization of the C-ring models.....	63
4.4 Simulation Procedure of C-ring models	64
4.5 Axisymmetric Torque Converter Piston Model.....	65
4.6 Simulation procedure of axisymmetric TC piston model.....	66
CHAPTER 5 VALIDATION OF THE FINITE ELEMENT MODELS.....	68
5.1 Distortion results of Navy C-rings.....	68
5.2 Bulk Volume/Nitrocarburized Volume Ratio	74
5.3 Distortion results of torque converter (TC) pistons.....	76
CHAPTER 6 COMPOSITION-DEPTH PROFILE SIMULATION MODEL	80
6.1 Carbon and nitrogen composition-depth profile simulation	80
6.2 Microstructure of torque converter (TC) piston samples	83
6.3 Composition-depth profile results.....	85
6.4 Residual stress determination – 1-step nitrocarburizing.....	87

6.5 <i>N</i> composition-depth profile model for two-step nitrocarburizing treatments	90
6.5.1 Composition-depth profile results – varying the 1 st step temperature	93
6.5.2 Composition-depth profile results – varying the 2 nd step temperature	95
6.5.3 Composition-depth profile results – varying the 1 st step <i>N</i> wt. %.....	97
6.5.4 Composition-depth profile results – increased process time	98
6.6 Residual stress determination – 2-step nitrocarburizing.....	102
CHAPTER 7 CONCLUSIONS AND FUTURE WORK	105
7.1 Conclusions.....	105
7.2 Major advances.....	108
7.3 Suggestions for future work	108
REFERENCES.....	110
APPENDICES	124
Appendix A.....	124
A.1 MATLAB program files for a single-step nitrocarburizing treatment	124
A.2 MATLAB program files for a two-step nitrocarburizing treatment	126
VITA AUCTORIS	130

LIST OF TABLES

Table 2.1: Characteristics of carburizing methods for AISI 8620 steel [19]	10
Table 2.2: Surface residual stress values of TC pistons after FNC and CN [28]	16
Table 2.3: Residual stresses due to salt bath nitrocarburizing (NC) and carbonitriding (CN) [31].....	18
Table 2.4: Change in OD, ID, GW and flatness distortions of nitrocarburized and carbonitrided 1010 Navy C-rings [44].....	25
Table 2.5: Hardness and distortion values of Navy C-ring specimens made from HSS 6-5-2 after vacuum heat treatment [45]	26
Table 2.6: Summary of the distortion modeling	36
Table 2.7: Summary of the composition profile modeling	42
Table 2.8: Summary of the residual stress-depth profile modeling	46
Table 3.1: Elemental compositions of SAE 1010 plain carbon steel [44]	50
Table 3.2: Heat treatment and specimen details	52
Table 4.1: Material properties used in the FEM models.....	60
Table 4.2: Mesh sensitivity study in a C-ring (C3) model.....	63
Table 4.3: Details about the C-ring elements.....	64
Table 4.4: Finite element simulation set up for C-ring models	65
Table 4.5: Finite element simulation set up for TC pistons.....	67
Table 5.1: Measured ID, OD and GW distortions for nitrocarburized C-rings	69
Table 5.2: C-ring's Gap Width (GW) distortion results – Top location.....	69
Table 5.3: C-ring's Gap Width (GW) distortion results – Middle location.....	70

Table 5.4: C-ring's Gap Width (GW) distortion results – Bottom location	70
Table 5.5 Comparison of the measured Outer Diameter (OD) distortion with the predicted OD distortion	72
Table 5.6: Comparison of the measured Inner Diameter (ID) distortion with the simulated results	73
Table 5.7: V/V_N ratio of Navy C-rings and TC pistons	75
Table 5.8: Experimental ID and OD distortions for nitrocarburized TC pistons.....	78
Table 5.9: Comparison of measured and predicted OD distortion of TC pistons.....	79
Table 5.10: Comparison of measured and predicted ID distortion of TC pistons	79
Table 6.1: Composition of nitrogen in ϵ , γ' and α phases [94, 95]	83
Table 6.2: Partial molar volume, predicted phase thickness and distortion.....	86
Table 6.3: CMM measured distortion values of SAE 1010 torque converter piston.....	87
Table 6.4: Comparison of measured and predicted surface residual stresses of nitrocarburized SAE 1010 torque converter pistons.....	90
Table 6.5: Simulated two step heat treatment conditions and N compositions	92
Table 6.6: Predicted local distortions for two-step nitrocarburizing treatments.....	102

LIST OF FIGURES

Figure 2.1: Ferritic nitrocarburized gear and other components [6].....	5
Figure 2.2: Optical micrographs (a-g) showing different types of compound layers on α -iron substrate by nitrocarburizing at 580°C [9].....	6
Figure 2.3: Phase diagram of Fe-N-C system at 570°C (logarithmic concentration scales) [13].....	7
Figure 2.4: AISI 1020 isopleth predicted using Thermo-Calc [14].....	8
Figure 2.5: Optical micrographs of nitrided (823 K (549°C) / 5 hrs, 60/40 vol.% NH ₃ /H ₂) iron specimen ((a) before annealing & (b) after annealing) [15].....	9
Figure 2.6: Schematic diagrams of ion nitrocarburizing system [17, 18] (x is carbon-carrier gas)	9
Figure 2.7: Schematic diagram of Korund-300 installation for fluidized bed nitrocarburizing treatment [21].....	11
Figure 2.8: (a) & (b) Salt bath nitriding/nitrocarburizing furnaces [20].....	12
Figure 2.9: Compound layer thickness vs. treatment time for mild steel, QT steel and hot worked steel (12%Cr-steel cast iron) [23].	12
Figure 2.10: Schematic diagram of bell-type gas nitriding furnace, (a) heating bell and (b) cooling bell [20].....	13
Figure 2.11: Schematic diagram of gas nitriding / nitrocarburizing furnace (pit-type) [24].....	14
Figure 2.12: Schematic of a horizontal vacuum nitriding/nitrocarburizing furnace [25].....	14

Figure 2.13: Microhardness and residual stress depth profiles of H11 tool steel, plasma nitrocarburized at 580°C/8 hrs (C1), 580°C/16 hrs (C2), 580°C/24 hrs (C3), and 580°C/32 hrs (C4) [29]..... 16

Figure 2.14: Residual stress-depth profiles of ϵ -phase iron nitride layer [30]..... 17

Figure 2.15: Residual stress-depth profile of a low carbon steel specimen that was vacuum annealed at 900°C/1hr+ nitrocarburized at 570°C/3hrs and artificial aged at 170°C/45min ((a) before fatigue, (b) after fatigue) [32]. 18

Figure 2.16: Flatness change of SAE 1010 torque converter (TC) pistons, gas ferritic nitrocarburized at 510°C/15hrs, 540°C/10hrs, 565°C/5hrs and 595°C/4hrs [28]..... 19

Figure 2.17: Distortion comparison of FNC vs. SR + FNC front rotor, adapted from [35]. 21

Figure 2.18: (a) Finished bearing ring, (b) Inner radius change and surface residual stresses of the ring due to turning [36]..... 21

Figure 2.19: (a) Navy C-ring dimensions as used by French [37], and (b) Navy C-ring specimen used by Webster and Laird [38] (dimensions in inches). 23

Figure 2.20: Dimensions of Navy C-rings used by (a) Bates et al. [40], and (b) Leskovsek and Ule [41]. 24

Figure 2.21: (a) Size and (b) shape distortion changes of carburized SAE Navy C-rings: carburizing treatments: 1) 927°C/6h (carbon potential 0.9), 2) 927°C/6h (carbon potential 1.0), 3) 927°C/6h (carbon potential 1.1), 4) 954°C/4h (carbon potential 0.9), 5) 954°C/4h (carbon potential 1.0), 6) 954°C/4h (carbon potential 1.1) and 7) 954°C/4h (carbon potential 1.2) [48]..... 27

Figure 2.22: (a) Carbon composition profile and (b) residual stress distributions for a carburized + water quenched long cylinder steel containing molybdenum [57]...... 28

Figure 2.23: (a) Temperature history (experimental and computed) at centre of tool steel block during gas quenching, (b) Distortion of gas quenched (3 bar N₂) ORVAR SUPREME tool steel block (experimental and computed). The distortion is magnified 50 times [58]. 29

Figure 2.24 : (a) Dimensional changes of a C-ring specimen before heat treatment (m and n dimensions) and after heat treatment (m' and n' dimensions), (b) distortion simulation (displacement magnification 20X) [60]. 30

Figure 2.25: Computed Gap Width (GW) vs. time curve [61]. 31

Figure 2.26: (a) Finite element model of one half of the C-ring, (b) Gap width (opening displacement) distortion of AISI 8620 carburized C-ring [62]. 31

Figure 2.27: Distortion engineering procedure by Zoch [34]. 32

Figure 2.28: (a) 100 mm long C-ring, (b) comparison of experiment and simulation distortion results, (c) banana effect, and (d) barrel or bobbin effect [63]. 33

Figure 2.29: Comparison of measured and predicted distortion (DANTE model) showing the "bowing" of AMS 6308 coupon [64]. 33

Figure 2.30: Radial displacement contour and distortion comparison of bore and tip distortion of AISI 4320H gear component [65]. 34

Figure 2.31: (a) – Geometry of a simplified large gear, (b) – Distortion comparison at seven points [66]. 35

Figure 2.32: (a) Carbon steel ring specimen geometry (dimensions in mm), (b) Measured and predicted distortion results at location 1 (outer diameter) and 2 (inner diameter) [67].	35
Figure 2.33: Nitrogen and carbon concentration profiles measured using EPMA on nitrocarburized Fe-0.8C (wt. %) and Fe alloys [68].	37
Figure 2.34: Special ferritic nitrocarburizing (FNC) process for increased N ₂ and C contents [69]......	37
Figure 2.35: Nitrogen concentration profile for nitrided 4140 steel (measured vs. computed) [70]......	38
Figure 2.36: Predicted nitrogen composition-depth profiles for pulse plasma nitride pure iron. The experimental data (Δ symbol) were acquired from Yan et al. [72], (a) T=773K (500°C) & (b) T= 793K (520°C) (1 represents ϵ phase, 2 is γ' and 3 represents α phase) [71]......	38
Figure 2.37: Predicted and experimental nitrogen, carbon composition profiles of plasma nitrocarburized austenitic stainless steel [73].	39
Figure 2.38: Simulated and experimental nitrogen depth profiles of plasma nitrided AISI 316L (400°C/2hrs) with different N diffusion coefficients [76]......	40
Figure 2.39: (a) schematic of housing, (b) plate-like component	41
Figure 2.40: Nitrogen composition-depth profiles (measured and calculated) [77]......	41
Figure 2.41: Predicted bore deformation for housing (case 1) and plate-like (case 2) components due to 2 different FNC treatments [77].	42
Figure 2.42: Predicted and measured axial residual stress of a carburized AMS 6308 steel coupon [64].	43

Figure 2.43: (a) – Predicted hoop residual stress map (MPa), (b) - Residual stress-depth profiles for a gas nitrided (550°C/120 hrs) tubular sample [78].	44
Figure 2.44: Residual stress-depth profiles at the center of the Almen strip, (a) 2.44 mm thick and (b) 3.18 mm thick [79].	44
Figure 2.45: Residual stress-depth profiles for the nitrided Fe-Al specimen (experimental and predicted) [81].	45
Figure 3.1: Overview of the research plan.	47
Figure 3.2: (a) Torque converter (TC), and (b) TC cross section [82].	48
Figure 3.3: (a, b) Navy C-ring specimen geometry, (c) schematic for Navy C-rings C1, C2 and C3 (dimensions in mm).	49
Figure 3.4: Geometry of torque converter (TC) piston.	51
Figure 3.5: Schematic process diagram of the ferritic nitrocarburizing treatment.	51
Figure 3.6: A light optical microscope (Leitz Laborlux 12 ME).	53
Figure 3.7: (a) Hysitron (Ubi1) nanomechanical instrument, (b) loading-unloading response for a SAE 1010 C-ring after FNC.	54
Figure 3.8: PRISMO coordinate measuring machine (CMM) [83].	55
Figure 3.9: Schematic of nitrogen composition-depth profile due to 1-step nitrocarburizing treatment.	56
Figure 3.10: Schematic of the simulated nitrogen composition-depth profile due to 2-step nitrocarburizing treatment.	57
Figure 3.11: Cameca SX50 Electron Probe Micro Analyzer (EPMA) at Earth Sciences, University of Toronto [84].	58
Figure 4.1: Navy C-ring geometry dimensions.	61

Figure 4.2: Compound layer comparison of the Navy C-ring probe model and the optical micrograph showing the compound layer of SAE 1010 steel.....	62
Figure 4.3: Half symmetric geometry of meshed Navy C-rings with varying thicknesses 19mm (C1), 10mm (C2), 3mm (C3).....	64
Figure 4.4: (a) Cross section of the torque Converter (TC) piston, (b) axisymmetric TC piston model.....	66
Figure 5.1: C-ring's GW distortion measurement locations.....	68
Figure 5.2: Measured and predicted gap width (GW) distortion profiles of Navy C-rings ((a) top, (b) middle & (c) bottom locations).	71
Figure 5.3: Outer Diameter (OD) distortion profile of Navy C-rings (measured and predicted).	73
Figure 5.4: Inner diameter (ID) distortion profile of Navy C-rings (measured and predicted).	74
Figure 5.5: V/V_N ratio vs. absolute errors for GW & ID distortions of Navy C-rings.	76
Figure 5.6: V/V_N ratio vs. absolute errors for OD distortions of Navy C-rings.	76
Figure 6.1: Experimental nitrogen profiles for vacuum nitrocarburized (580°C/10hrs) and gas nitrocarburized (580°C/10hrs) TC piston samples.	80
Figure 6.2: Simulated nitrogen composition-depth profiles	82
Figure 6.3: (a), (b) and (c) Optical micrographs of SAE 1010 TC piston specimen subjected to vacuum ferritic nitrocarburizing at 580°C/10hrs.	84
Figure 6.4: (a), (b) and (c) Optical micrographs of SAE 1010 TC piston specimen subjected to gas ferritic nitrocarburizing at 565°C/5hrs.	84

Figure 6.5: Carbon composition depth profile of SAE 1010 steel TC pistons measured using EPMA.....	85
Figure 6.6: Comparison of experimental and simulated nitrogen-profiling results of SAE 1010 nitrocarburized TC pistons ((a) – at the surface, (b) overall).	86
Figure 6.7: Predicted residual stress-depth profiles for FNC heat treatments (580°C/10hrs and 565°C/5hrs).	89
Figure 6.8: Simulated nitrogen composition-depth profile due to 2-step nitrocarburizing process ‘A’ (595°C / 3.6 hrs / 8% + 427°C / 1.4 hrs / 3%).	94
Figure 6.9: Predicted nitrogen composition-depth profile due to two-step nitrocarburizing process ‘B’ (580°C/3.6 hrs/8% + 427°C/1.4 hrs/3%).	94
Figure 6.10: Predicted nitrogen composition-depth profile due to two-step nitrocarburizing process ‘C’ (565°C / 3.6 hrs / 8% + 427°C / 1.4 hrs / 3%).....	95
Figure 6.11: Predicted N composition-depth profiles for heat treatment ‘A’ and ‘D’ (595°C/3.6hrs/8wt.%+477°C/1.4hrs/3wt.%).	95
Figure 6.12: Predicted N composition-depth profile for heat treatment ‘B’ and ‘E’ (580°C/3.6hrs/8wt.%+477°C/1.4hrs/3wt.%).	96
Figure 6.13: Predicted N composition-depth profile for heat treatment ‘C’ and ‘F’ (565°C/3.6hrs/8wt.%+477°C/1.4hrs/3wt.%).	96
Figure 6.14: Predicted N composition-depth profiles for heat treatment ‘G’ (595°C/3.6hrs/7wt.%+427°C/1.4hrs/3wt.%) and heat treatment ‘H’ (580°C/3.6hrs/7wt.%+427°C/1.4hrs/3wt.%).	97
Figure 6.15: Predicted N composition-depth profile for heat treatment ‘I’ (565°C/3.6hrs/7wt.%+427°C/1.4hrs/3wt.%).	98

Figure 6.16: Predicted N composition-depth profile for heat treatment ‘J’
(595°C/10hrs/8wt.%+427°C/2.7hrs/3wt.%). 99

Figure 6.17: Simulated nitrogen composition-depth profile due to two-step
nitrocarburizing process (580°C/10hrs/8% + 427°C/2.7hrs/3%). 99

Figure 6.18: Simulated nitrogen composition-depth profile due to two-step
nitrocarburizing process (565°C/10hrs/8% + 427°C/2.7hrs/3%). 100

Figure 6.19: Residual stress distribution due to 2-step nitrocarburizing process. 104

LIST OF APPENDICES

Appendix A: MATLAB program files for 1-step & 2-step nitrocarburizing treatment.....	124
--	-----

LIST OF ABBREVIATIONS/SYMBOLS

OD	Outer Diameter
ID	Inner Diameter
GW	Gap Width
LRO	Lateral Run Out
TC	Torque Converter
FNC	Ferritic Nitrocarburizing
CL	Compound Layer
CN	Carbo-Nitriding
EPMA	Electron Probe Micro Analyzer
CMM	Coordinate Measuring Machine
GDOES	Glow Discharge Optical Emission Spectroscopy
FEM	Finite Element Method
FDM	Finite Difference Method
XRD	X-Ray Diffraction

NOMENCLATURE

E	Young's modulus
σ	stress
ν	Poisson's ratio
ρ	density
c	elemental composition
D	diffusion coefficient
t	diffusion time
h	heat transfer coefficient
T	temperature
V_ε	partial molar volume of ε phase
$V_{\gamma'}$	partial molar volume of γ' phase
l_ε	thickness of ε phase
$l_{\gamma'}$	thickness of γ' phase
Δl_ε	local distortion due to ε phase
$\Delta l_{\gamma'}$	local distortion due to γ' phase in the compound layer
$\Delta l_{\gamma' \text{ in diff. zone}}$	local distortion due to γ' phase in the diffusion zone
$\hat{\sigma}$	Cauchy stress tensor
G	shear modulus
K	compressibility
ε_ε	strains due to ε phase
$\varepsilon_{\gamma'}$	strains due to γ' phase

M	molar fraction
σ_ε	residual stress due to ε phase
$\sigma_{\gamma'}$	residual stress due to γ' phase

CHAPTER 1 INTRODUCTION

Surface engineering is used to improve properties like corrosion or wear resistance that are not present in the bulk material. It also improves the quality, performance and life-cycle cost of the products, which are widely used in industries like automotive, aerospace, electronics and construction. The common surface engineering treatments are mechanical, thermo-mechanical, thermal, thermo-chemical, electrochemical & chemical, and physical techniques [1]. Heat treatments involving carburizing, nitriding, carbonitriding, and nitrocarburizing are a class of thermo-chemical surface engineering methods. The carburizing process produces a thick high-carbon martensitic case by adding carbon in the steel surface at elevated temperatures (800-1090°C) in the austenitic phase field. The main differences between carburizing and carbonitriding are the ammonia addition and the lower temperature range (705-900°C) in the carbonitriding process. The nitriding and nitrocarburizing processes, on the other hand, produce a thin compound layer at relatively lower temperatures (495-650°C) in the ferritic phase field.

Ferritic nitrocarburizing is a case hardening process in which gases, like methane/propane, ammonia and nitrogen, react with the metallic surface at 500-650°C. Ferritic nitrocarburizing offers excellent scuffing, wear and fatigue resistance by producing a thin compound layer (containing ϵ -Fe_{2.3}(C, N), γ' -Fe₄(N, C), cementite (Fe₃C) and various alloy carbides and nitrides) on the material surface. The thickness of the compound layer is usually in the range of 5 to 30 μ m. Ferritic nitrocarburizing is widely used to case harden torque converter pistons, brake rotors, gears, pinion shafts and

other wear components. The highlights of nitrocarburizing are smaller distortion than carbonitriding and no phase transformation in the bulk material [2]. However, this smaller distortion, if left untreated, could lead to performance issues in the automotive component. Machining or straightening the surface can eliminate the distortion but requires additional work hours and cost. Moreover, machining will reduce the thickness of nitrocarburized layer thereby reducing service performance of the component.

Residual stresses, which are developed during the manufacturing process conditions, often lead to distortion. Although residual stress results in dimensional changes of a material, it can provide resistance to crack initiation [3]. Any heat treatment process is a major source for distortion [4].

Navy C-rings are generally used as a test specimen to observe the dimensional distortion before analyzing an actual component (torque converter piston) for distortion. To better understand the distortion mechanisms, SAE 1010 Navy C-rings with three different thicknesses (2.8, 10, 19 mm) were used. These 3 different thicknesses were chosen to report the distortion due to change in geometry of C-rings. Torque converter (TC) piston is an automotive component that is used to measure and calculate distortion for the application of the process in practice.

The numerical simulation of heat treatment conditions were started initially in the mid-1970s [5]. The heat treatment simulations were mainly developed to predict the residual stresses and distortion. In this study, numerical techniques including finite element method (FEM) and finite difference method (FDM) are used to understand the

distortion mechanisms in Navy C-ring probe and Torque Converter (TC) piston specimens.

1.1 Research Objectives and Approach

The main focus of this research is to methodically examine the distortion in nitrocarburized SAE 1010 Navy C-ring and torque converter piston specimens. Finite element models of Navy C-rings and torque converter pistons were developed to predict the distortion trend. The predicted distortion results were compared with the experimental distortion.

An electron probe micro analyzer (EPMA) was used to measure the composition-depth profiles of nitrocarburized torque converter piston specimens. Using the composition profiles, a numerical model was developed using finite difference method to predict the compound layer thickness and distortion due to nitrocarburizing treatment. The predicted composition-depth profiles were compared with the experimental profiles. Also, the surface residual stress was predicted and compared against the experimental surface residual stress.

Based on the distortion analyses and residual stress distribution after nitrocarburizing treatments, a two-step nitrocarburizing technique is suggested, which should produce smaller distortion than single stage nitrocarburizing, while improving the surface characteristics in the automotive component.

1.2 Dissertation Outline

Chapter 2 presents a literature review of ferritic nitrocarburizing process, residual stresses, distortion, and modeling of distortion and residual stress.

Chapter 3 shows the analytical approach taken to solve the distortion problem. Experimental and numerical investigations are discussed in detail about the distortion calculation, N profiles and residual stresses.

Chapter 4 presents the finite element simulations of Navy C-rings and torque converter (TC) pistons.

Chapter 5 shows the validation of the finite element simulations of Navy C-rings and TC pistons.

Chapter 6 discusses the composition-depth profile simulation models, which are used to predict the distortion due to the nitrocarburized phases.

Chapter 7 highlights the summary and conclusions arising from this study and provides suggestions for future work.

CHAPTER 2 LITERATURE REVIEW

The objective of the literature survey is to understand the ferritic nitrocarburizing process, distortion mechanisms, distortion prediction methods, composition-depth profiling and residual stress modeling.

2.1 Ferritic Nitrocarburizing (FNC)

Ferritic nitrocarburizing (FNC) was first introduced in 1947 in a cyanide, salt-based batch process. The FNC process was later refined as a gaseous ferritic nitrocarburizing process by Lucas Industries in 1961 [6]. Many engineering components like rocker-arm spacers, textile machinery gears, pump cylinder blocks, jet nozzles, crank-shafts and drive shafts are case-hardened using nitrocarburizing treatments [7]. Gear steels made of SAE 4140, 5160, 8620 and certain tool steels are also surface engineered using the ferritic nitrocarburizing (FNC) process [8]. There are different types of ferritic nitrocarburizing processes in the automotive industry: gas, ion or plasma, fluidized bed, vacuum and salt bath. Figure 2.1 shows the automotive components that have been ferritic nitrocarburized.



Figure 2.1: Ferritic nitrocarburized gear and other components [6].

The nitrocarburizing process is carried out in the ferritic region of the Fe-C phase diagram. After nitrocarburizing, the surface of the part exhibits two distinct regions, namely a compound layer and diffusion zone. These two regions are the main reason for providing high resistance to wear and corrosion in nitrocarburized materials. The compound layer can be a single-phase layer containing ϵ - $\text{Fe}_{2.3}(\text{N}, \text{C})$ or a dual-phase layer containing both ϵ and γ' . Leineweber et al. [9] reported the types of the compound layer microstructures that can be formed on the α -iron substrate upon nitrocarburizing (see Fig. 2.2):

- (1) γ' layers,
- (2) ϵ/γ' layers,
- (3) $\epsilon/\epsilon+\gamma'$ layers,
- (4) ϵ layers + cementite, and
- (5) cementite (θ) layers

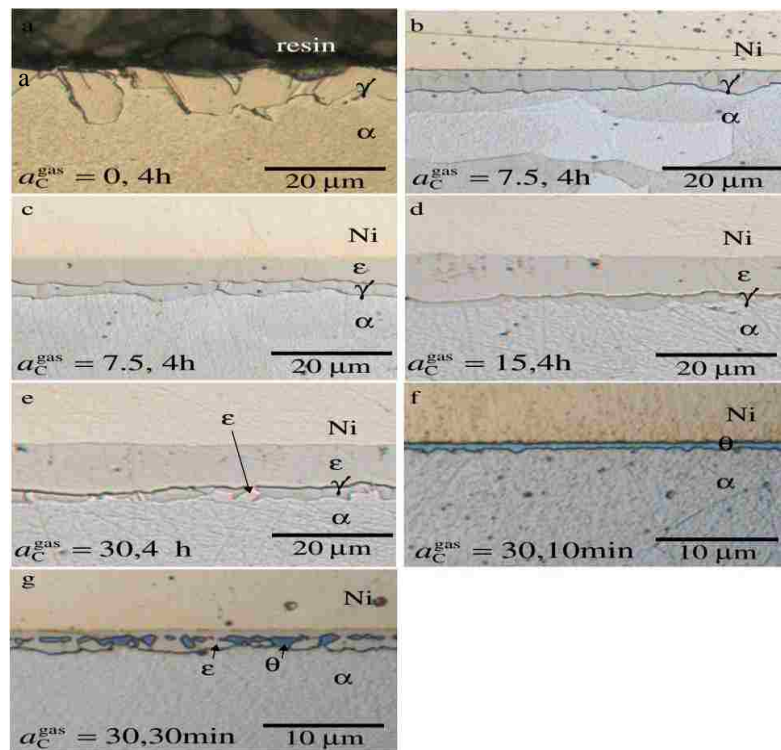


Figure 2.2: Optical micrographs (a-g) showing different types of compound layers on α -iron substrate by nitrocarburizing at 580°C [9].

The phase transformation sequence in the nitrocarburizing surface of carbon steels was found contradictory. Bell et al. [10] reported the nitrocarburized phase transformation of carbon steels in the following form: $\alpha + N + C \rightarrow \varepsilon \rightarrow \gamma'$. Mittemeijer [11] presented the phase sequence of the compound layer due to gas nitrocarburizing as: $\alpha + N + C \rightarrow \theta \rightarrow \varepsilon \rightarrow \gamma'$. They both reported ε -phase formation before γ' . However, Chen et al. [12] reported γ' to ε phase transformation. They demonstrated the formation mechanism of nitrocarburized phases as follows: $\alpha + N + C \rightarrow \gamma + N + C \rightarrow \gamma' + N + C \rightarrow \varepsilon$. Microstructural examination in the transition layer (between the compound layer and the diffusion zone) suggested that an intermediate phase state γ (austenite) was first produced before the pearlite colonies, and the γ phase was transformed into γ' during the ferritic nitrocarburizing process.

Figure 2.3 shows the Fe-N-C phase diagram, where α gets transformed to $\alpha + \gamma'$ (point b, assuming negligible C wt. %). With the increase in N wt. %, ε phase will occur from the $\alpha + \gamma'$ region (producing γ' to ε phase transformation).

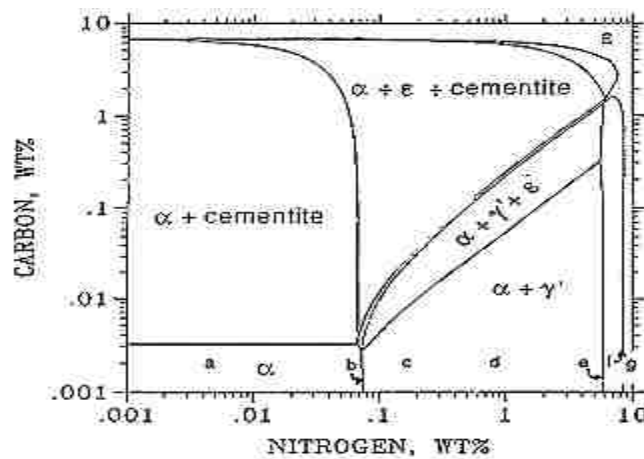


Figure 2.3: Phase diagram of Fe-N-C system at 570°C (logarithmic concentration scales) [13].

Yang and Sisson Jr. [14] simulated the phase evolution of carbon steels to predict the first forming phase. The first nitride phase was reported to be ϵ -phase during the nitriding process. They have concluded that a single γ' -phase is not possible in carbon steels: see isopleth in Figure 2.4 which shows no single γ' phase region at typical nitriding/nitrocarburizing temperatures.

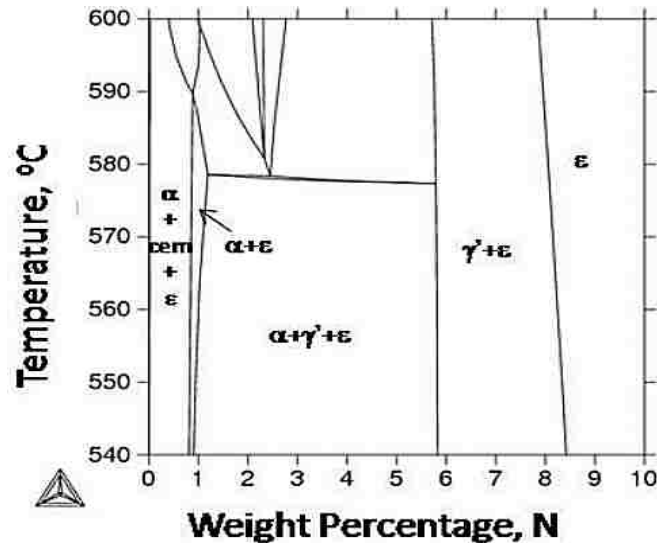


Figure 2.4: AISI 1020 isopleth predicted using Thermo-Calc [14]

An interesting regrowth of γ' sublayer was reported by Liapina et al. [15]. In their study, an iron cast rod specimen was subjected to gas nitriding at 823 K (550°C) for 5hrs followed by water quenching. The specimen was then annealed at 630 K (356°C) for 120 hrs and cold water quenched. Figure 2.5 shows the increase in γ' sublayer at the cost of ϵ phase due to the annealing process. Therefore, an individual γ' -phase is possible for iron specimen.

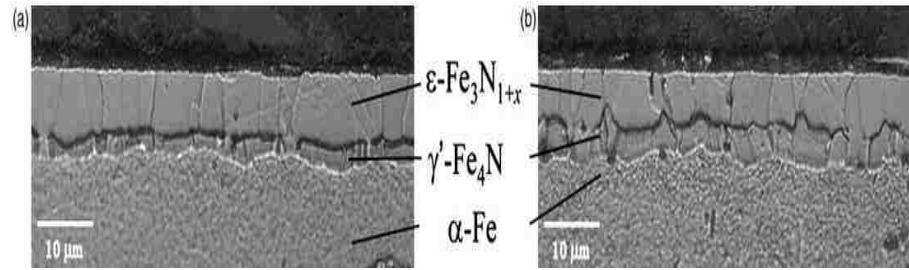


Figure 2.5: Optical micrographs of nitrided (823 K (549°C) / 5 hrs, 60/40 vol.% NH₃/H₂) iron specimen ((a) before annealing & (b) after annealing) [15].

The compound layer thickness depends on the type of ferritic nitrocarburizing (FNC) process. The maximum thickness of the compound layer due to FNC was observed to be approximately 40μm [16]. The different types of nitrocarburizing processes are briefly discussed in sections 2.1.1 to 2.1.5.

2.1.1 Ion or plasma nitrocarburizing

Ion or plasma nitrocarburizing is a low pressure thermochemical treatment in which nitrogen, hydrogen and carbon producing gases were utilized to produce a compound layer (ϵ) and diffusion zone on the steel surface. A glow discharge with a high ionization level is generated around the parts. The schematic of ion nitrocarburizing systems are shown in Figure 2.6.

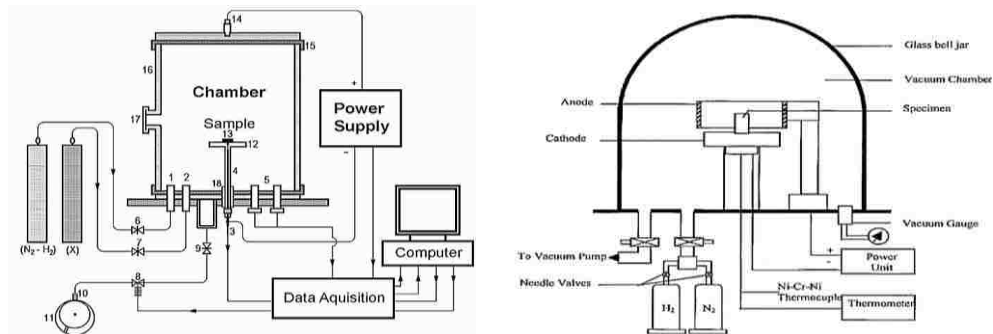


Figure 2.6: Schematic diagrams of ion nitrocarburizing system [17, 18] (x is carbon-carrier gas) .

Cherian [19] has reported a microwave atmospheric plasma technology called AtmoPlas™ to carburize the steel parts. The technology reduced the heating cycle times and energy by reaching high temperature in seconds. By using microwave carburizing technology, surface carbon concentration, case depth uniformity, and retained austenite were found to be better than the conventional processes (see Table 2.1).

Table 2.1: Characteristics of carburizing methods for AISI 8620 steel [19]

Characteristic/ property	Conventional gas carburized	Vacuum carburized	AtmoPlas carburized
Total carburizing time	142min boost + 110min diffuse + 20min temp.drop = 272min	Carburizing zone time =205 min	112min boost + 80min diffuse + 20min temp.drop = 212min
Case depth	~0.035 in. (~0.9mm)	~0.035 in. (~0.9mm)	~0.045 in. (~1.14mm)
Depth of retained austenite (%)			
Corner microstructure	~15-30% to ~0.0125in (~0.319mm)	~15-30% to ~0.0067 in (~0.319mm)	~5-20% to ~0.0067in (~0.172mm)
Surface microstructure	~10-20% to ~0.0046in (~0.119mm)	~5-15% to ~0.0095 in (~0.243mm)	~5-20% to ~0.0058in (~0.148mm)

2.1.2 Fluidized bed nitrocarburizing

In fluidized bed nitrocarburizing treatment, ammonia, compressed air and methane are blown to fluidize the catalyst (Al-Ni-Mg or aluminum oxide). The finely divided aluminum oxide will then transfer the heat from the heating medium to the workpiece. The heating medium can be electric or gas [20]. Figure 2.7 shows the schematic diagram of Korund-300 fluidized bed furnace.

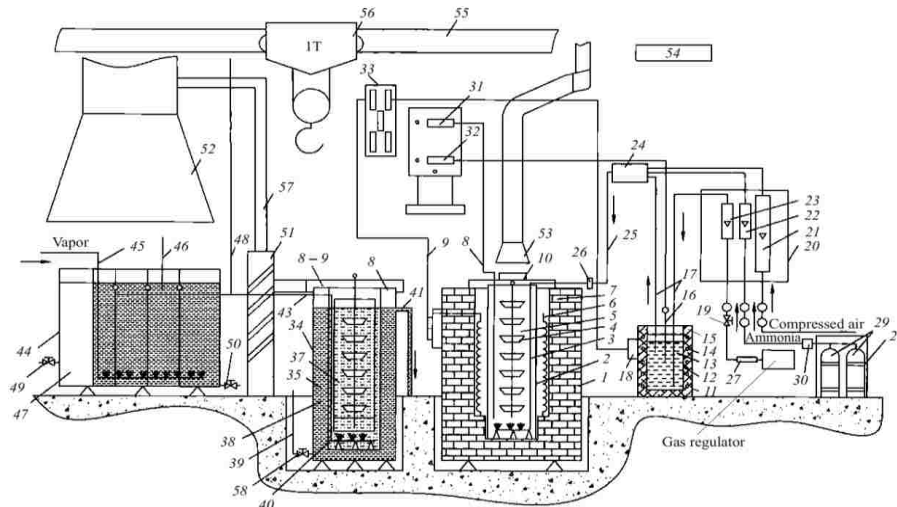


Figure 2.7: Schematic diagram of Korund-300 installation for fluidized bed nitrocarburizing treatment [21].

[1] body of the shaft furnace, 2) retort, 3) header 4) container, 5) catalyst, 6) heater, 7) heat insulation, 8) thermocouple, 9) current feedthrough, 10) cover, 11, 12) body and chamber of the device for gas cleaning, 13) catalyst, 14) heater, 15) heat insulation, 16) thermocouple, 17) gas inlet, 18) current feedthrough, 19) plug cock, 20) body of gas distribution panel, 21) air rotameter, 22) ammonia rotameter, 23) natural gas rotameter, 24) mixer, 25) pipe for feeding gas-air mixture to retort, 26) flange coupling, 27) pressure regulator in the natural gas feed line, 28) ammonia manifold, 29) ammonia cylinders, 30) pressure regulator in the ammonia feed line, 31, 32) millivoltmeter, 33) power supply cabinet, 34) body of quenching tank, 35) quenching tank, 36) safety grate, 37) oil, 38) water jacket, 39) water feed, 40) header, 41) water discharge, 42) flume for sucking off oil vapors, 43) air duct, 44) washing tank, 45) steam inlet, 46) cold water feed, 47) oil arresting compartment, 48) compressed air feed, 49) oil discharge, 50) water discharge, 51) oil vapor arrester, 52) funnel, 53) hinged funnel, 54) combined extract and input ventilation, 55) monorail, 56) monorail hoist, 57) choke, 58), valve] [21].

2.1.3 Salt bath nitrocarburizing

In salt bath nitrocarburizing treatment, the automotive part is immersed in a molten salt (NaCN , Na_2CO_3) containing nitrogen and carbon. The nitrogen and carbon from the salt will then react with the part's surface forming a compound layer and diffusion zone. The externally heated salt bath furnaces are shown in Figure 2.8. Recent development in the salt bath nitriding/nitrocarburizing treatment resulted in using a regenerable non-cyanide salt bath that produces no waste salt [22].

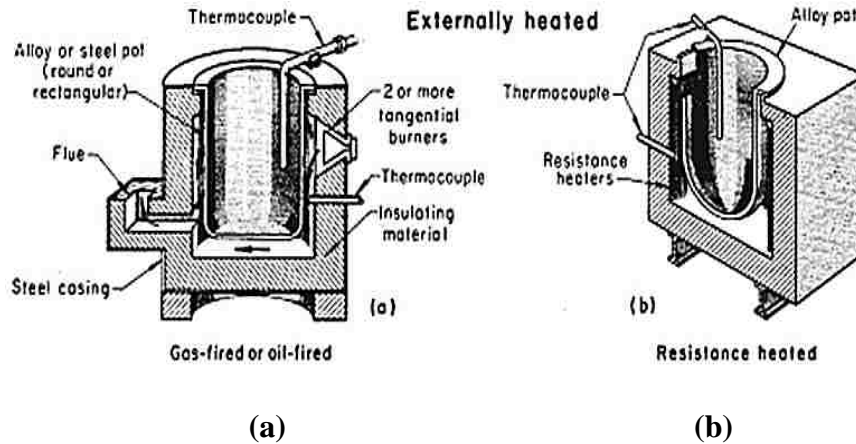


Figure 2.8: (a) & (b) Salt bath nitriding/nitrocarburizing furnaces [20].

TUFFTRIDE[®] is a salt bath nitrocarburizing process that takes place in a TF1 bath (containing alkali cyanate and alkali carbonate) at 480-630°C [23]. Figure 2.9 shows the compound layer thickness after TUFFTRIDE[®] treatment (580°C/1-2hrs) for mild steel, QT steel and hot worked steel (12%Cr-steel cast iron). It was found that the thickness of the compound layer changes with the treatment time and material type. Mild steel produced thicker compound layer than QT steel and 12%Cr-steel cast iron.

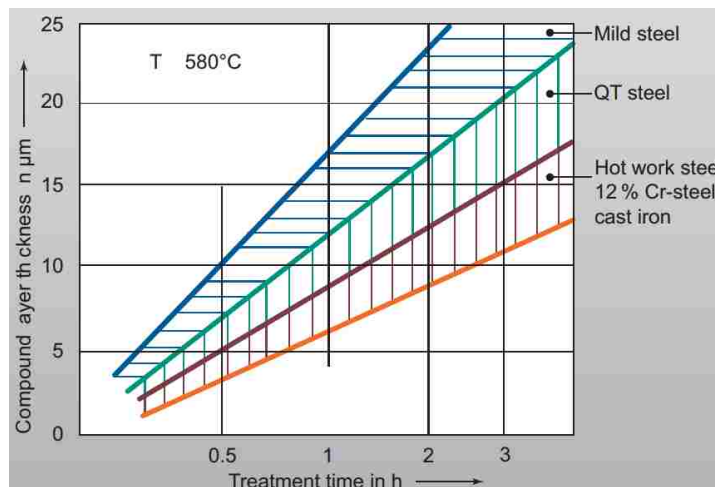


Figure 2.9: Compound layer thickness vs. treatment time for mild steel, QT steel and hot worked steel (12%Cr-steel cast iron) [23].

2.1.4 Gas nitrocarburizing

Gas nitrocarburizing employs ammonia and hydrocarbon or carbon bearing gases (like CO_2 , CO) into the steel surface to produce a compound layer and diffusion zone. The ammonia and $\text{CO}_2 + \text{CO}$ gases dissociate according to the Equations 2.1 to 2.6 [24]. The atomic nitrogen and carbon are needed for the diffusion to take place at the steel surface.

Gas nitriding/nitrocarburizing process can be carried out using bell-type and pit-type furnaces, which are schematically shown in Figure 2.10 and 2.11. Using a bell-type furnace, a uniform compound layer can be attained at the steel surface due to the temperature uniformity caused by the internal fan.

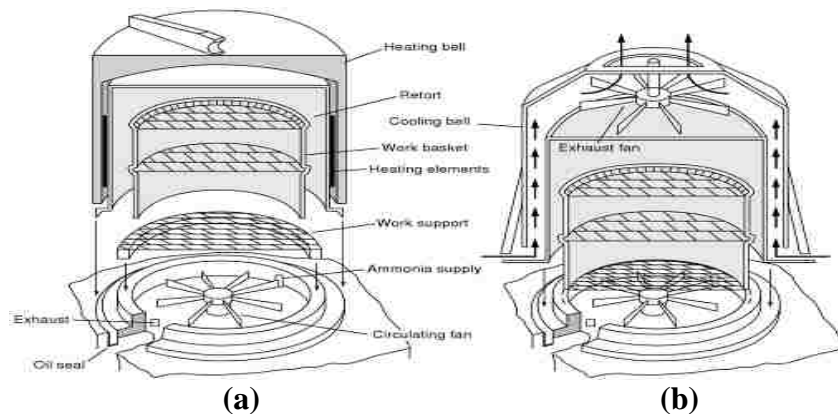
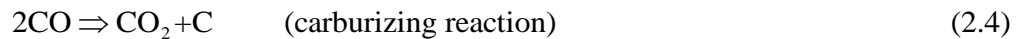
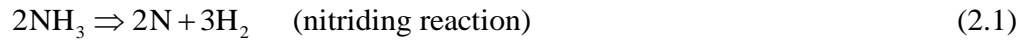


Figure 2.10: Schematic diagram of bell-type gas nitriding furnace, (a) heating bell and (b) cooling bell [20].

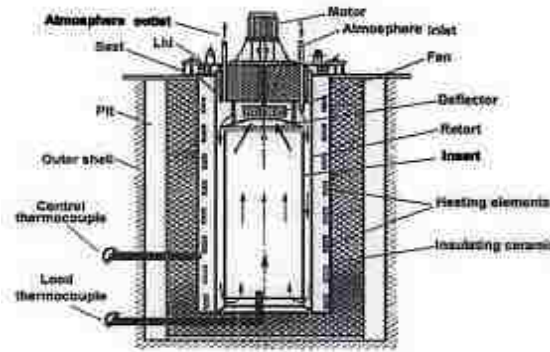


Figure 2.11: Schematic diagram of gas nitriding / nitrocarburizing furnace (pit-type) [24].

2.1.5 Vacuum nitrocarburizing

In vacuum nitrocarburizing treatment, the air is completely evacuated from the furnace. Then the ammonia and carbon producing gases are passed into the hot chamber to case harden the workload. Figure 2.12 shows the schematic diagram of a single-chamber, front loading vacuum furnace. The cooling gas inlet and outlet will be used to furnace cool the workload after nitrocarburizing.

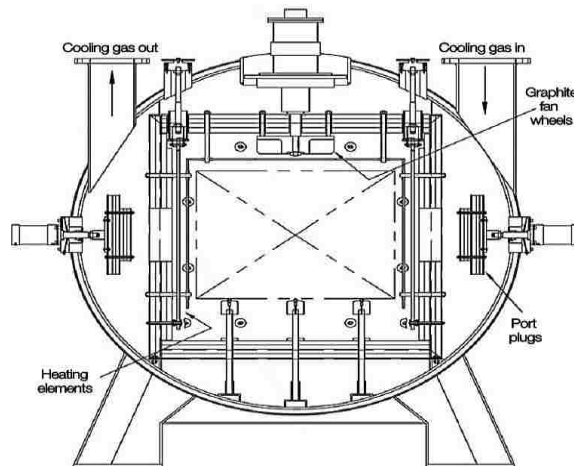


Figure 2.12: Schematic of a horizontal vacuum nitriding/nitrocarburizing furnace [25].

2.2 Residual stress

Residual stress prediction should be part of any heat treatment modeling because residual stress affects the distortion, fatigue performance and corrosion resistance of a component. A large amount of residual stress may cause the component to fail prematurely. Ericsson [26] stated that the evolution of large residual stresses due to thermal and thermochemical heat treatments was caused by the following reasons:

- a) thermal stresses due to thermal expansion or contraction of a homogeneous material in a temperature gradient field,
- b) different thermal expansion coefficients of the various phases in a multiphase material
- c) density changes due to phase transformations in the metal
- d) growth stresses of reaction products formed on the surface or as precipitates,
- e) chemical composition gradients below the surface

In thermochemical heat treatments like nitriding and nitrocarburizing, residual stresses are also the result of cohesion of the misfitting compound layer to the ferritic substrate and cohesion within the compound layer [27]. Compressive residual stress obtained in the surface of an automotive component is considered beneficial, since it can prevent crack propagation and improve fatigue endurance. However, tensile residual stresses exist in the ϵ -nitride surface layer due to nitrocarburization. Nan et al. [28] reported tensile residual stresses for SAE 1010 torque converter (TC) pistons after ferritic nitrocarburizing (FNC) process but compressive stresses for a carbonitriding (CN) process (see Table 2.2). The tensile stress values for the ϵ -phase compound layer varied from 76.5 to 268.2 MPa for all processing scenarios studied.

Table 2.2: Surface residual stress values of TC pistons after FNC and CN [28]

Heat treatment	Surface residual stress (MPa)
Gas FNC + Nitrogen cooling (510°C / 15 hrs)	122.0 ± 10.3
Gas FNC + Nitrogen cooling (540°C / 10 hrs)	146.9 ± 19.3
Gas FNC + Nitrogen cooling (565°C / 5 hrs)	268.2 ± 26.2
Gas FNC + Nitrogen cooling (595°C / 4 hrs)	76.5 ± 22.8
Ion FNC (560°C / 15 hrs)	186.2 ± 21.4
Ion FNC (525°C / 24 hrs)	224.1 ± 18.6
Gas FNC (N potential) + Nitrogen cooling (525°C / 52 hrs)	172.4 ± 9.7
Gas FNC (N potential) + Nitrogen cooling (570°C / 4 hrs)	241.3 ± 23.4
Vacuum FNC (580°C / 10 hrs)	262.7 ± 20.0
Gas FNC + quenching (580°C / 2 hrs + water quench)	252.3 ± 19.3
Gas carbonitriding (850°C / 4 hrs + 100°C oil quench)	-188.9 ± 26.2

Leskovsek et al. [29] reported the microhardness and residual stress distribution of plasma nitrocarburized H11 steel (see Fig. 2.13). The surface hardness increases with longer plasma nitrocarburizing time while the surface residual stress (tensile) decreases with increase in heat treatment time. Higher tensile residual stresses are not considered to be good enough to protect the steel from wear and fatigue.

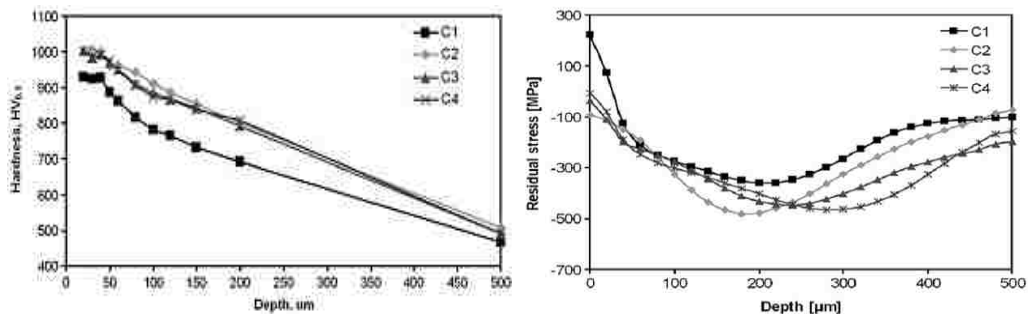


Figure 2.13: Microhardness and residual stress depth profiles of H11 tool steel, plasma nitrocarburized at 580°C/8 hrs (C1), 580°C/16 hrs (C2), 580°C/24 hrs (C3), and 580°C/32 hrs (C4) [29].

The residual stresses in the ϵ -phase iron nitride (within $2\mu\text{m}$ depth) have been measured using ψ -tilt and grazing incidence x-ray diffraction methods [30]. The ϵ -phase was produced on the part's surface using a two-stage gas nitriding treatment. Figure 2.14 shows tensile residual stress at the ϵ -phase varied in the range of 200-1200MPa. The residual stress values measured using the X-ray penetration is plotted as Tau profile (open circles) and the predicted residual stress is plotted as Z-profile (solid line). The dotted line represents the reconstructed tau profile calculated from the Z-profile.

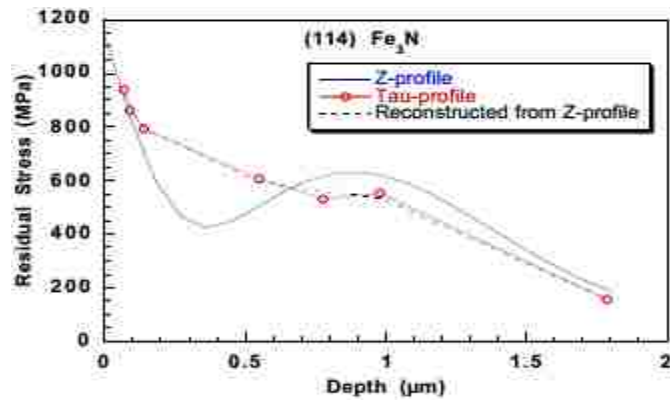


Figure 2.14: Residual stress-depth profiles of ϵ -phase iron nitride layer [30].

In contrast to the tensile stresses of ϵ -phase iron nitride mentioned above, compressive residual stresses were observed in the ϵ -phase of salt bath nitrocarburized AISI O2 tool steel (see Table 2.3). Before salt bath nitrocarburizing, the samples were annealed at 760°C for 1hr and tempered at 600°C for 1hr [31]. The surface residual stresses of ϵ - Fe_3N changed from -251 ± 51 MPa to -276 ± 30 MPa. Thomas and Bell [32] have also reported compressive residual stress on the compound layer of annealed + gas nitrocarburized low carbon steel specimen. Figure 2.15 (a) & (b) presents the compressive surface residual stress profiles measured before and after fatigue testing. An

almost complete fading of the residual stress occurred on the early stages of fatigue (see Fig. 2.15(b)).

Table 2.3: Residual stresses due to salt bath nitrocarburizing (NC) and carbonitriding (CN) [31]

Heat treatment	Nitride layers	NC (MPa)			CN (MPa)
		Fe ₃ N (113)	Fe _α (211)	Fe ₄ N (200)	γ (311)
NC (570°C/1hr)	very thin	-	-239±38	-	-
NC (570°C/3hrs)	Fe ₃ N>Fe ₄ N<Fe _α	-251±51	-259±67	-266±60	-
NC (570°C/4hrs)	Fe ₃ N=Fe ₄ N>Fe _α	-252±51	-411±82	-254±83	-
NC 570°C/5hrs	Fe ₃ N>Fe ₄ N<Fe _α	-268±55	-353±97	-281±75	-
NC 570°C/6hrs	Fe ₃ N>Fe _α	-276±30	-340±35	-	-
CN (870°C/1hr+oil quench to 180°C)	No	-	-122±38	-	-52±15

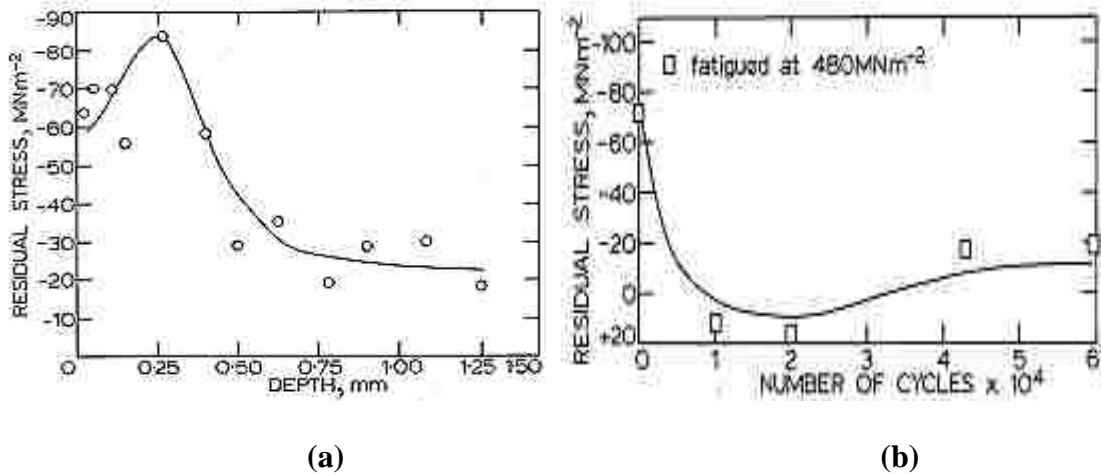


Figure 2.15: Residual stress-depth profile of a low carbon steel specimen that was vacuum annealed at 900°C/1hr+ nitrocarburized at 570°C/3hrs and artificial aged at 170°C/45min ((a) before fatigue, (b) after fatigue) [32].

Therefore, the surface stress for ϵ -phase in nitrocarburized tool steel (AISI O2) can be compressive but the ϵ -phase for nitrocarburized carbon steels (SAE 1010) are tensile in nature.

2.3 Distortion

Distortion can be defined as an inconsistent size or shape change of a material caused by the manufacturing process conditions. Two types of distortions are produced by the surface engineering treatments. They are size distortion and shape distortion. Size distortion is caused by the change in volume between the base material and the surface layer. Diameter changes and gap width changes are reported as size distortion. Materials that undergo twisting, bending and curving without any change in volume produce shape distortion. The changes in roundness, flatness and cylindricity are termed as shape distortion. Figure 2.16 shows the change in flatness (shape distortion) of nitrocarburized torque converter pistons. The mean of flatness change values ranged from 15.64% to 25.11%.

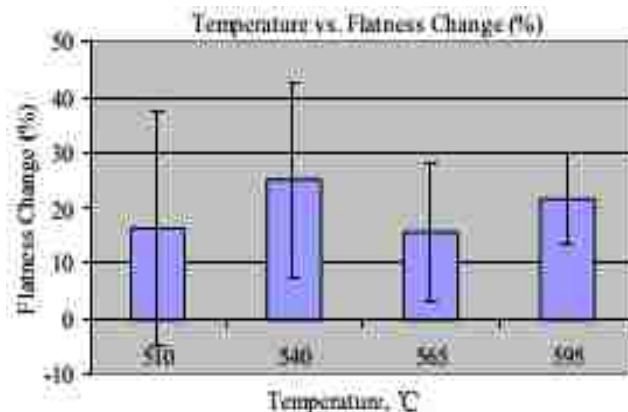


Figure 2.16: Flatness change of SAE 1010 torque converter (TC) pistons, gas ferritic nitrocarburized at 510°C/15hrs, 540°C/10hrs, 565°C/5hrs and 595°C/4hrs [28].

In the automotive and other industries, distortion can occur due to various reasons. Zoch [33] points out that minimizing distortion is not only a quality concern but is also an economic concern since between 20 and 40% of the production cost for components such as bearing races are due to machining costs to eliminate distortion. The carriers of “distortion potential” include [34]:

- a) Geometry
- b) Chemical composition / segregation
- c) Microstructure/ grain size
- d) Residual stress
- e) Temperature
- f) Mechanical history

The geometry and chemical composition are the two factors that are related to distortion even before subjecting the component to heat treatment. The microstructural changes, residual stresses and temperature resulting from the heat treatment will also produce distortion.

Holly et al. [35] from General Motors Company found that the stress relieved (SR) FNC rotors showed lower distortion (lateral run out (LRO)) than as-machined FNC rotors. The stress relief was performed at $607 \pm 15^\circ\text{C}$ for 3hrs followed by furnace cooling prior to FNC treatment. The FNC cast iron brake rotor exhibited better wear and corrosion protection than the standard non FNC brake rotor after extended parking. By providing excellent scaling resistance and static corrosion performance, FNC rotors can also help to decrease the brake pulsation [35]. Figure 2.17 compares the distortion (LRO) of FNC and stress relieved FNC front rotors.

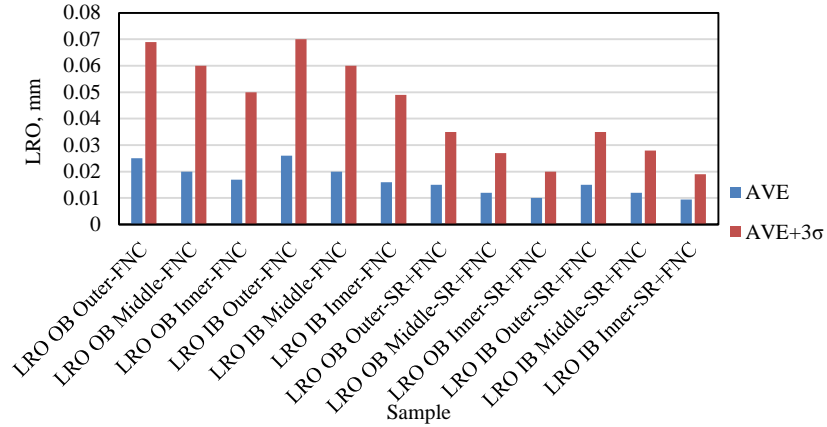


Figure 2.17: Distortion comparison of FNC vs. SR + FNC front rotor, adapted from [35].

Although distortion is significantly influenced by heat treatment, machining before heat treatment can give rise to distortion as well. Brinksmeier et al. [36] reported the dimensional deviations of SAE 52100 steel bearing rings (see Fig. 2.18(a)) due to a turning (soft machining) process. After machining, polygonal type deviations occurred due to the elastic deformation caused by fixing the workpiece in the chuck. The inner radius change was attributed to the locally varying residual stresses that enlarged the bearing ring (Fig. 2.18(b)).

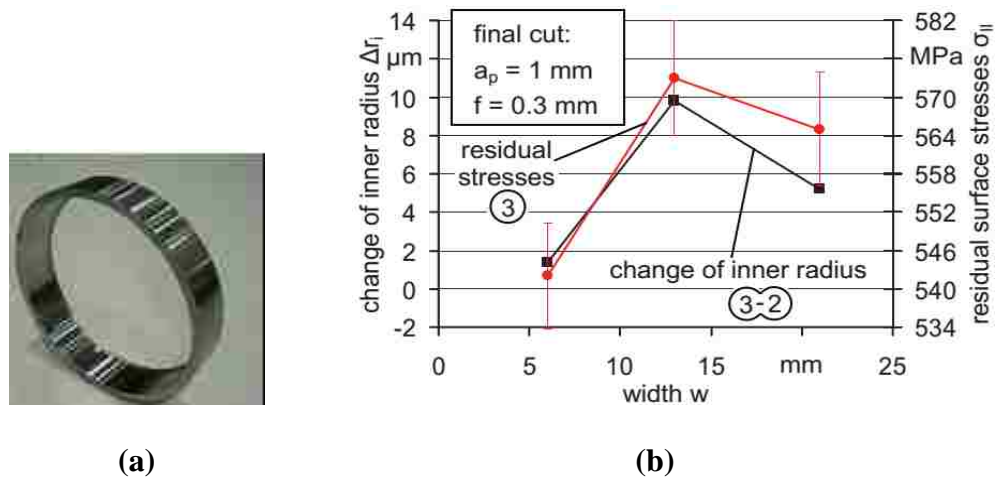


Figure 2.18: (a) Finished bearing ring, (b) Inner radius change and surface residual stresses of the ring due to turning [36].

2.3.1 Distortion prevention methods

Distortion is difficult to eliminate, but can be prevented by taking necessary steps before and during heat treatment. The following methods were used to obviate distortion in heat treated parts [3]:

- (a) Straightening - It helps to relieve the residual stresses in plain carbon and low-alloy steels. The major disadvantage of straightening is the loss of fatigue properties and crack initiation.
- (b) Support and restraint fixtures - Restraint fixtures are used during rapid cooling operation to control the dimensional changes of the parts. Support fixtures are used for parts that deliver sufficient self-restraint.
- (c) Quenching fixtures - Quenching fixture helps to prevent distortion during water or oil quenching. However, it requires accurate positioning, unobstructed quenchant flow, and an arrangement for draining the hot quenchant.
- (d) Pressure quenching - Using high pressure (5 MPa) and a turbulent gas flow, the heat treated parts are uniformly cooled to produce lower distortion.
- (e) Press quenching - It is applied to a specific geometry like flat circular diaphragms of spring steel where direct quenching is difficult.
- (f) Rolling die quenching - In rolling die quench machine, the heat treated parts are placed on the rollers and the rolls turn to minimize distortion.
- (g) Stress relieving - To reduce distortion, residual stresses are released by subcritical annealing or normalizing treatment prior to the final machining

operation. Plain carbon and low-alloy steels are stress relieved at temperatures of 550-650°C.

2.4 Types and use of Navy C-rings

The Navy C-ring is the common type of specimen used for observing dimensional changes due to heat treatment. Before analyzing an automotive component for distortion, Navy C-ring specimens machined from the material of interest are heat treated to observe any distortion. It is generally presumed that the dimensional change of a Navy C-ring specimen is comparable with the change in dimensions of the actual component.

Navy C-rings have been widely used in different dimensions according to their application. In the late 1920s, French [37] started using C-shaped gauges to study distortion and cracking, primarily in quenched steels. He reported that the thin and heavy sections of C-ring specimens, Figure 2.19(a), prevent uniform cooling thereby offering a means to promote distortion. Another type of Navy C-ring that was used to check the size and shape change distortion was the ‘modified Navy C-ring’. The dimensions of the modified Navy C-ring test specimens are shown in Fig. 2.20. It is evident that the outer diameter (OD) of the Bates C-ring (refer to Fig.2.20(a)) was reduced by half compared to the OD dimension reported by Webster and Laird [38] (see Fig.2.19(b)).

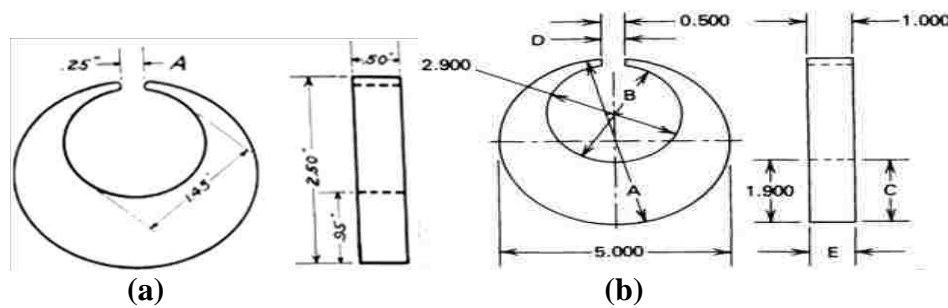


Figure 2.19: (a) Navy C-ring dimensions as used by French [37], and (b) Navy C-ring specimen used by Webster and Laird [38] (dimensions in inches).

Leskovsek et al. [39] found that the hardness values of modified Navy C-ring specimens and the metallographic specimens were comparable under identical heat treatment conditions. Based on this hardness comparison, they also assumed that the microstructure of modified Navy C-ring specimens will be similar to the metallographic specimens under the same heat treatment conditions.

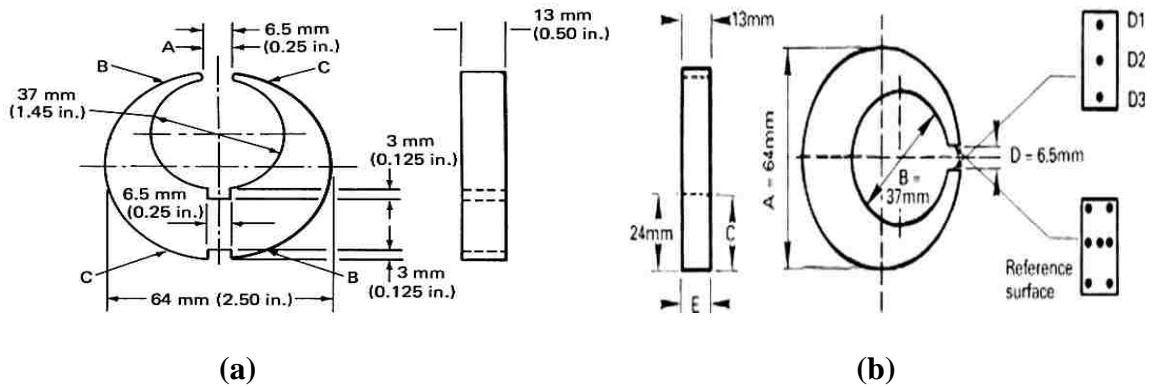


Figure 2.20: Dimensions of Navy C-rings used by (a) Bates et al. [40], and (b) Leskovsek and Ule [41].

Bates et al. [40] reported that the notched C-ring has greater crack sensitivity over and above distortion. Also the dimensions of the notched C-ring (Fig. 2.20 (a)) and the C-ring in Fig. 2.20 (b) are similar to the one used by French (see Fig.2.19 (a)).

Nan et al. [28, 42-44] used Navy C-ring specimens to study the distortion in ferritic nitrocarburized SAE 1010 plain carbon steel. Ion, vacuum and gas ferritic nitrocarburizing processes were applied to the Navy C-rings with varying thicknesses to analyze distortion. Table 2.4 shows the inner diameter (ID), outer diameter (OD), gap width (GW) and flatness distortions of nitrocarburized and carbonitrided SAE 1010 C-ring specimens [44]. Nitrocarburized C-rings have lower ID, OD, GW and flatness distortions than the carbonitrided C-rings.

Table 2.4: Change in OD, ID, GW and flatness distortions of nitrocarburized and carbonitrided 1010 Navy C-rings [44]

Heat Treatment	Change in ID, %	Change in OD, %	Change in GW, %	Change in flatness, mm
Gas ferritic nitrocarburizing				
565°C/5hrs+N ₂ cooling	0.0201	0.0438	0.0311	0.0001
Gas carbonitriding				
850°C/4hrs+oil quench (100°C)	0.1565	0.1146	2.4424	-0.0038

Distortion in high-speed steel was studied by Leskovsek and Ule [41] using the Navy C-ring specimens shown in Figure 2.20 (b). Table 2.5 shows the distortion values of high-speed steel Navy C-ring specimens used by Leskovsek [45]. The parameter ‘A’ denotes the outer diameter (OD), ‘B’ is the inner diameter (ID) and ‘D’ is the gap width (GW) of C-rings (refer Fig. 2.20 (b)). The deep cryogenic treatment at -196°C in liquid nitrogen caused greater dimensional stability (outer and inner diameters A and B) after subsequent tempering, but increased the gap width distortion (ΔD). He attributed the increase in gap width distortion to the transformational and thermal stresses.

Table 2.5: Hardness and distortion values of Navy C-ring specimens made from HSS 6-5-2 after vacuum heat treatment [45]

Vacuum heat treatment and DCT	Group of Navy C-ring sample	Hardness HRC	Dimensions of NC specimens, (mm)						Difference dimensions, (%)		
			Before vacuum heat treatment			After vacuum heat treatment			ΔA	ΔB	ΔD
			A	B	D	A	B	D			
1050/80/830/4h/ 20°C/h/600/25°C 1230/80/2x500°C	NC1	60.0	63.993	37.011	6.674	63.783	36.891	6.670	- 0.328	- 0.324	- 0.060
	NC2	59.9	63.991	37.012	6.618	63.783	36.895	6.615	- 0.325	- 0.316	- 0.045
	NC3	60.2	63.995	37.014	6.650	63.780	36.887	6.645	- 0.336	- 0.343	- 0.075
1050/80/830/4h/ 20°C/h/600/25°C 1230/80/1x500/ -196/1x500°C	NC4	63.9	63.999	37.034	6.676	63.882	36.926	6.547	- 0.183	- 0.292	- 1.932
	NC5	64.3	63.996	37.035	6.656	63.882	36.933	6.527	- 0.178	- 0.275	- 1.938
	NC9	64.7	63.993	37.024	6.674	63.890	36.934	6.586	- 0.161	- 0.243	- 1.318
1050/80/830/4h/ 20°C/h/600/25°C 1230/80/2x540°C	NC6	65.4	63.997	37.024	6.676	63.959	36.999	6.674	- 0.059	- 0.067	- 0.030
	NC7	65.4	63.998	37.018	6.673	63.957	36.994	6.669	- 0.064	- 0.065	- 0.060
	NC8	65.6	63.993	37.010	6.675	63.956	36.983	6.664	- 0.044	- 0.073	- 0.165
1050/80/830/4h/ 20°C/h/600/25°C 1230/80/ -196/1x540°C	NC10	66.0	63.998	37.017	6.636	64.008	37.017	6.631	+ 0.016	0.000	- 0.090
	NC11	66.0	63.997	37.017	6.636	64.011	37.016	6.627	+ 0.022	- 0.003	- 0.136
	NC12	66.0	63.996	37.025	6.637	64.011	37.030	6.624	+ 0.023	+ 0.013	- 0.196
1050/80/830/4h/ 20°C/h/600/25°C 1150/80/2x500°C	NC13	59.0	63.989	37.025	6.656	63.982	37.033	6.700	- 0.011	+ 0.022	+ 0.661
	NC14	59.0	63.994	37.017	6.635	63.988	37.025	6.678	- 0.009	+ 0.022	+ 0.648
	NC15	59.0	63.998	37.015	6.634	63.988	37.020	6.673	- 0.016	+ 0.013	+ 0.588

Northwood et al. [28, 42-44, 46-51] have worked extensively on Navy C-rings to determine distortion (size and shape) and residual stress in PS-18, SAE 8620, 4320 and 1010 steels. Their studies were mainly focused on minimizing distortion due to heat treatment processes such as carburizing, carbonitriding and nitrocarburizing. Figure 2.21 (a, b) shows the size and shape distortion changes of carburized SAE 8620 C-rings. After carburizing at 927/954°C, the C-rings were oil quenched (70°C) and tempered (149°C) to improve dimensional stability. The results showed that the distortions are increased by the increase in retained austenite and residual stress.

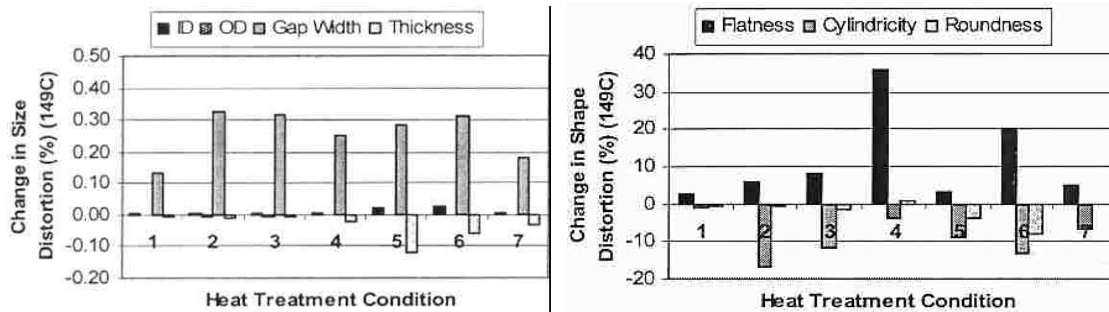


Figure 2.21: (a) Size and (b) shape distortion changes of carburized SAE Navy C-rings: carburizing treatments: 1) 927°C/6h (carbon potential 0.9), 2) 927°C/6h (carbon potential 1.0), 3) 927°C/6h (carbon potential 1.1), 4) 954°C/4h (carbon potential 0.9), 5) 954°C/4h (carbon potential 1.0), 6) 954°C/4h (carbon potential 1.1) and 7) 954°C/4h (carbon potential 1.2) [48].

2.5 Modeling

The use of high speed computations provided a new method to calculate internal stresses and associated distortions. Computer modeling helps in preventing multiple experimental attempts to develop a heat treatment practice that minimizes the distortion, time and cost. It also became a useful tool to improve our understanding of the mechanisms causing distortion.

Convergence analysis/mesh sensitivity is an important step in the finite element simulation process. It is performed to reduce the discretization error in the mesh. The element size is gradually decreased with every model and the final result (for example: stress, displacement) is estimated repeatedly. By further decreasing the element size, the final result of the current and previous model will eventually become the same. The convergence error is then calculated by the percentage difference between the final result of the current model and the previous model. This type of approach is called the h-

convergence [52] and with several runs, the discretization error can be significantly reduced.

To determine distortion and residual stresses numerically, the temperature field and the distribution of phases must be known. Inoue and Tanaka [53] published a model estimating the temperature history including transformation heat and a finite element model to calculate the residual stresses including transformation strains. Their model has been refined over several years [54-57]. A finite element code called ‘HEARTS’ was developed in which all six of the couplings (thermal stress, heat generation due to deformation, temperature-dependent phase transformation, latent heat due to phase transformation, transformation stress and transformation plasticity, and stress-induced transformation) are included. The predicted carbon content after carburization agrees well with the measured (XRD) carbon composition (see Fig. 2.22(a)). The residual stress distributions of the carburized steel cylinder specimen showed compressive residual stress at the surface and later became tensile until 3.5 mm from center (see Fig. 2.22(b)).

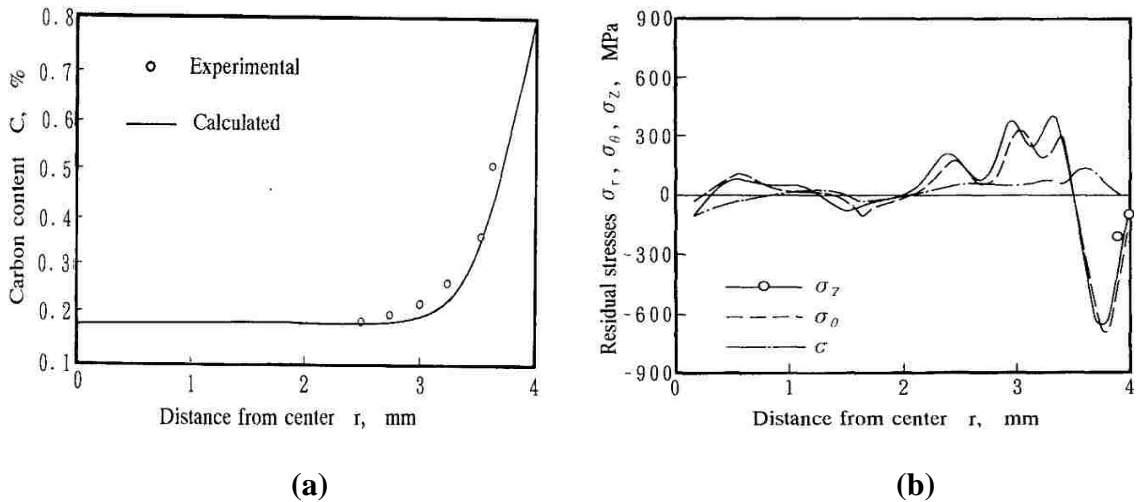


Figure 2.22: (a) Carbon composition profile and (b) residual stress distributions for a carburized + water quenched long cylinder steel containing molybdenum [57].

Thuvander et al. [58, 59] presented a numerical model to predict distortion during heat treatment of tool steels using coupled temperature calculation and phase transformation and subsequent analysis of mechanical response. The simulations have been carried out with finite element model code ABAQUS with additional routines for phase transformations. Both diffusion controlled and martensite transformations were included in the model. Heat treatment simulations for quenching and tempering as well as case hardening have been performed.

The temperature history of tool steel blocks (ORVAR SUPREME and DIEVAR) were validated against the measured temperature (see Fig. 2.23(a)). The predicted distortion of gas quenched tool steel blocks were found to be in a good agreement with the experimental distortion (Fig. 2.23(b)).

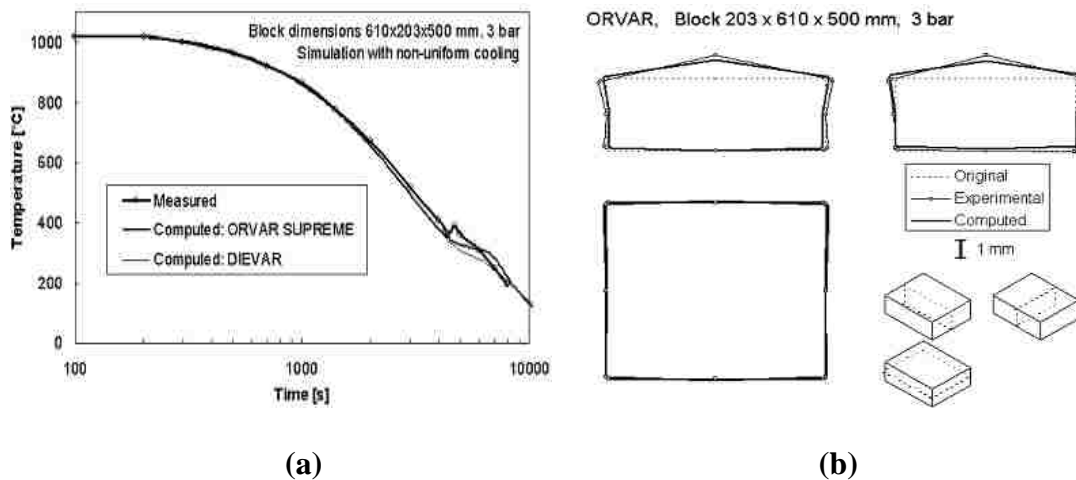


Figure 2.23: (a) Temperature history (experimental and computed) at centre of tool steel block during gas quenching, (b) Distortion of gas quenched (3 bar N₂) ORVAR SUPREME tool steel block (experimental and computed). The distortion is magnified 50 times [58].

2.5.1 Distortion modeling

Silva et al [60] reported the distortions of AISI 4140 steel C-rings quenched in oil. They predicted a 7% error between the experimental and numerical values of the C-ring Gap Width (GW) and Outer Diameter (OD) distortions. These geometric distortions of the C-rings were attributed to austenite-martensite transformation at the thicker regions of the C-ring. Figure 2.24(a, b) shows the gap width distortion and distortion simulation of a C-ring specimen due to heat treatment.

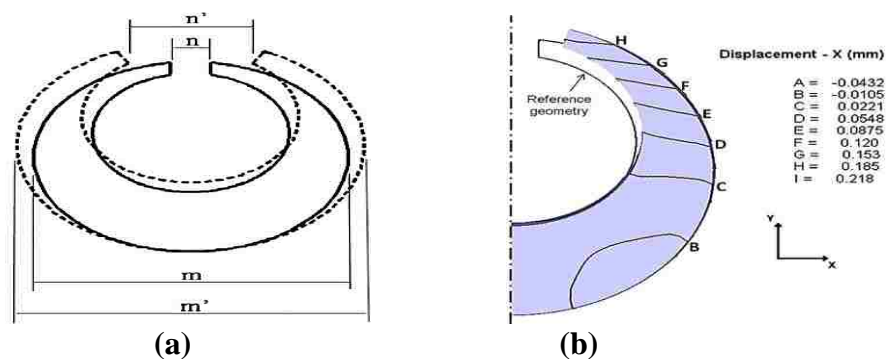


Figure 2.24 : (a) Dimensional changes of a C-ring specimen before heat treatment (m and n dimensions) and after heat treatment (m' and n' dimensions), (b) distortion simulation (displacement magnification 20X) [60].

Hernández-Morales et al. [61] studied the evolution of thermal and stress fields in a AISI 304 stainless steel modified Navy C-ring probe cooled to 40°C in still water. They applied an uncoupled thermo-elasto-plastic model to predict the internal stress field and distortion using DEFORM-HT (commercial software). The model was successfully validated by comparing the computed and measured thermal response. The measured and predicted gap length of C-ring also showed a good agreement. They concluded that the C-ring gap widens at the early stages of quenching due to the thermal contraction of the

tip of the probe and then closes as the thermal contraction of the medium portion of the probe arm pushes the tip inwards (see Fig. 2.25).

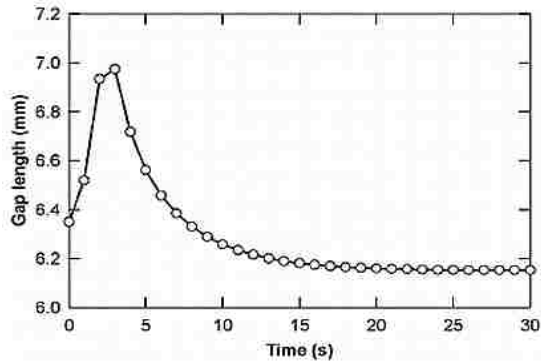


Figure 2.25: Computed Gap Width (GW) vs. time curve [61].

Li et al. [62] developed a finite element model of an AISI 8620 steel C-ring (Fig. 2.26(a)) using DANTE (commercial software) to simulate the furnace heating, carburization, quenching and tempering processes. Adding carbon lowered the gap width distortion from 0.05 to 0.02mm (see Fig. 2.26(b)). However quenching increased the distortion to 0.22mm. The results showed that the gap width distortion of the C-ring was very sensitive to the heat treatment conditions. The gap width distortion was caused by the thermal gradient and phase transformation sequence.

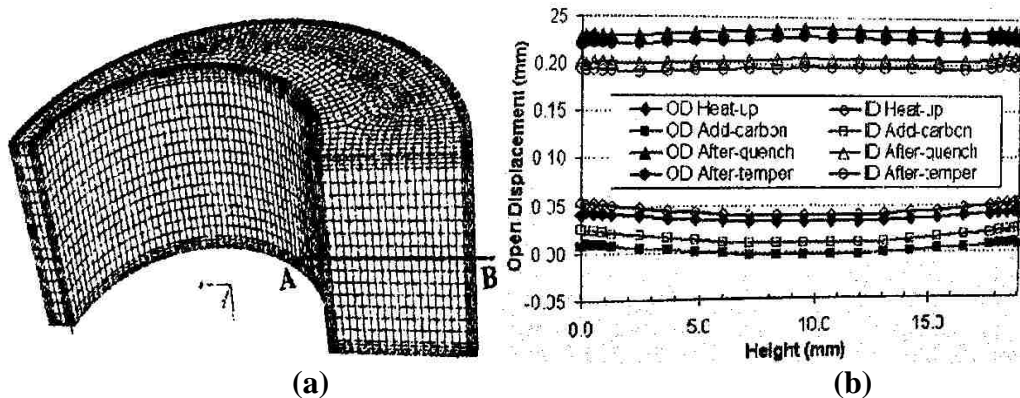


Figure 2.26: (a) Finite element model of one half of the C-ring, (b) Gap width (opening displacement) distortion of AISI 8620 carburized C-ring [62].

Zoch [34] presented a methodology called “distortion engineering” (see Fig. 2.27) to understand the dimensional changes of SAE 52100, 4140 and 5120 rings, shafts and discs/gears. The simulated processes include rolling, forging, milling, heating, carburizing and quenching. The distortion compensation was found to be difficult for shafts and discs/gears but the distortion could be compensated successfully for rings. Hence the material geometry is an important aspect that should be considered to reduce distortion.

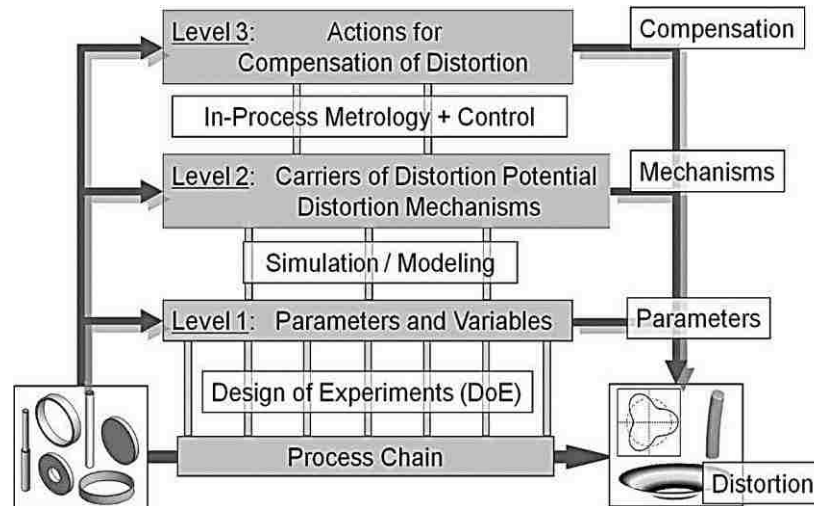


Figure 2.27: Distortion engineering procedure by Zoch [34].

Nicolas et al. [63] presented the experimental and simulation results of 3-D distortion identification from quenched ASCOMETAL steel grade C-ring. The C-ring test part was 100mm long with a 16mm wide opening. The dimensions of outer and inner diameters were 70 and 45 mm with 11 mm off-centered. The 3-D distortion of C-rings were reported as ovalization, barrel effect and banana effect (see Fig. 2.28).

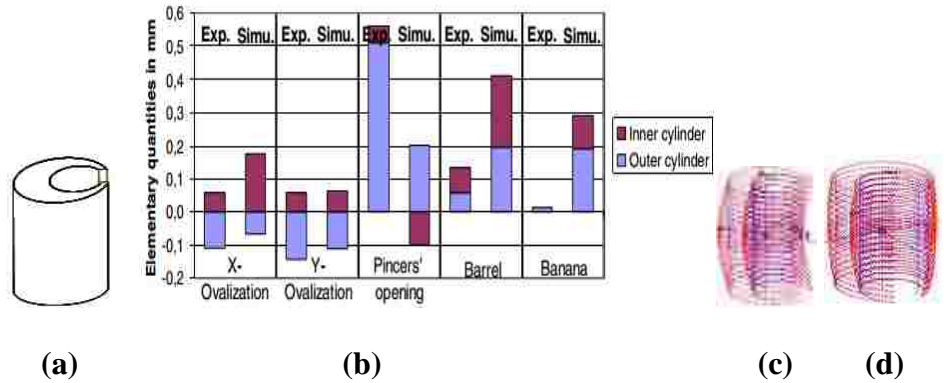


Figure 2.28: (a) 100 mm long C-ring, (b) comparison of experiment and simulation distortion results, (c) banana effect, and (d) barrel or bobbin effect [63].

Freborg et al [64] developed a heat treatment simulation model to predict the residual stress and distortion response in a carburized AMS 6308 steel coupon. Convective heat transfer coefficients (htc) were calculated from the thermal response of a 304 stainless steel test block and a DANTE (commercial software) thermal model. A constant heat transfer coefficient (htc) was assumed during gas quenching as the temperature dependent properties like thermal conductivity and kinematic viscosity have less effect on htc. Figure 2.29 shows the distortion comparison of an AMS 6308 coupon that was vacuum carburized + subcritical annealed + austenitized + gas quenched + deep frozen + double tempered.

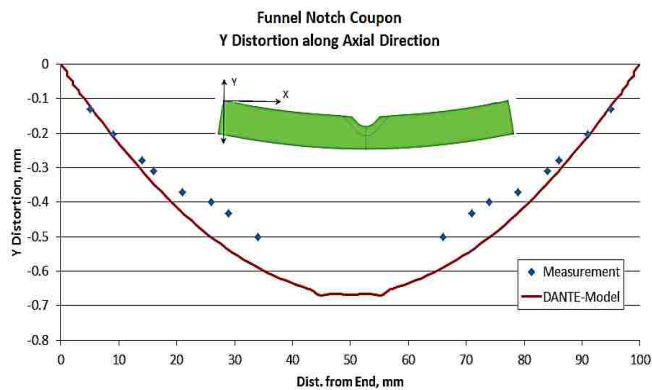


Figure 2.29: Comparison of measured and predicted distortion (DANTE model) showing the "bowing" of AMS 6308 coupon [64].

They have also modeled a heat treatment simulation involving carburization and oil quenching for AISI 4320H gear component [65]. The radial distortion was predicted and validated by the experimental measurements (see Fig. 2.30).

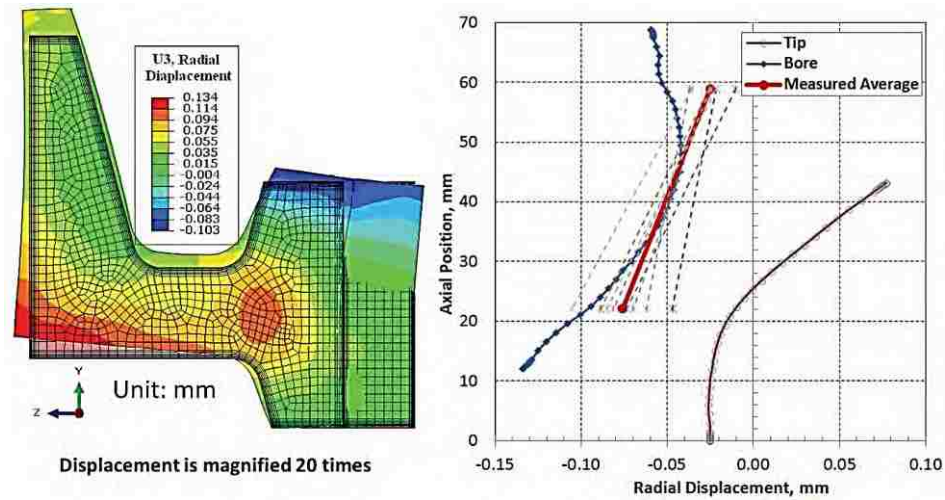


Figure 2.30: Radial displacement contour and distortion comparison of bore and tip distortion of AISI 4320H gear component [65].

Depouhon et al. [66] presented a numerical model to anticipate the distortion in a simplified large gear due to nitriding (see Fig. 2.31 (a)). The distortion was measured experimentally using a 3D coordinate measuring machine (CMM) and the predicted distortion results were validated against the measured distortion. The predicted and measured distortion were calculated at seven different locations in the gear. The predicted distortion values reported in Figure 2.31 (b) seem to be in good agreement with the experimental values. The simulation method assumed that the volumetric eigen strains were the only source of distortion.

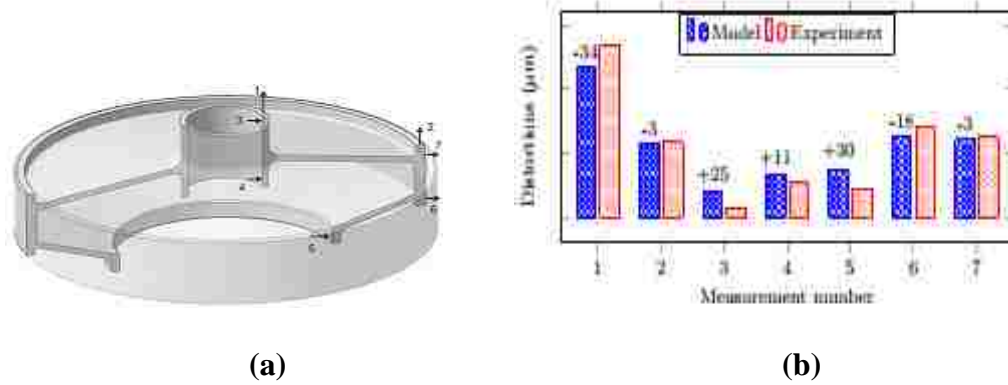


Figure 2.31: (a) – Geometry of a simplified large gear, (b) – Distortion comparison at seven points [66].

A mathematical model was developed to predict the distortion, carbon and nitrogen contents in a carbo-nitrided ASTM 4118 carbon steel specimen (see Fig. 2.32 (a)). The heat treatment starts with heating at 930°C/120 min followed by passing C/N gas with carbon and nitrogen potentials of 1.1% and 0.3%. The carbo-nitriding process was carried out for 240 min followed by cooling at 850°C for 40 min. In the end, the specimen was oil quenched to 60°C. The predicted distortion shows partial agreement with the experimental results (refer Fig. 2.32 (b)).

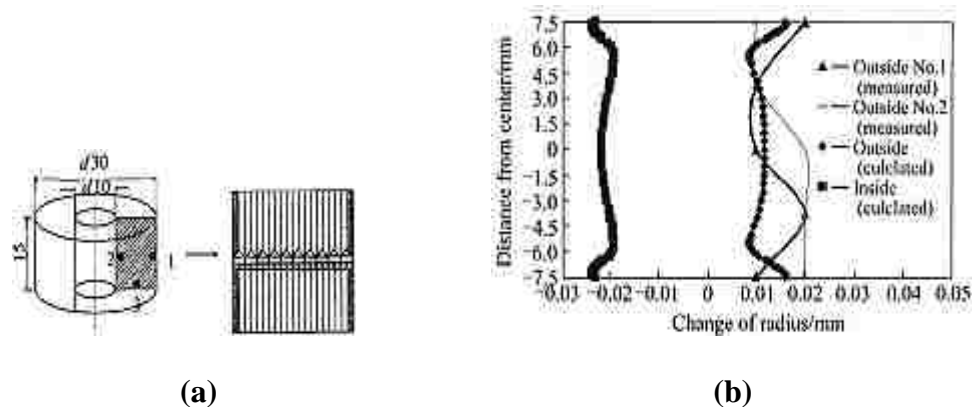


Figure 2.32: (a) Carbon steel ring specimen geometry (dimensions in mm), (b) Measured and predicted distortion results at location 1 (outer diameter) and 2 (inner diameter) [67].

Table 2.6 is a summary of the distortion modeling discussed in section 2.5.1. The distortion was predicted mostly for carburizing treatments that involve austenite to martensite phase transformation. Extensive literature is not available for the distortion modeling of nitrocarburizing processes.

Table 2.6: Summary of the distortion modeling

Study (Ref.)	Material/Heat treatment	Component of modeling	Core material phase transformation	Agreement with experiment*
[60]	AISI 4140 steel/ carburizing (900°C/1hr)+oil quench(25°C/300s)	C-ring	austenite to martensite	good
[61]	AISI 304 stainless steel / heating(900°C)+Water quench(40°C)	modified C-ring	no phase transformation	good
[62]	AISI 8620 steel / carburizing(925°C/ 6hrs)+oil quench(65°C/10min)+ tempering(150°C/2hrs)	C-ring	austenite to lower bainite & martensite	good
[63]	ASCOMETAL steel grade/heating(930°C)+ quench(20°C)	modified C-ring	not mentioned	partial
[64]	AMS 6308 steel/ carburizing+anneal+ austenitize+gas quench(10 bar N ₂) +deep freeze+double temper	notched coupon	austenite to martensite	moderate
[65]	AISI 4320H steel/ Carburizing(927°C/ 15hrs+857°C/1hr)+oil quench(70°C)	gear	austenite to martensite & bainite	partial
[66]	32CrMoV13 steel/ Gas nitriding(120hrs)	gear	no phase transformation	good
[67]	ASTM 4118 carbon steel/carbonitriding (930°C/360min)+cooled (850°C/10min)+oil quench(60°C)	ring	austenite to martensite & bainite	partial

* ‘good’ denotes <10% difference between experimental and simulated values, ‘moderate’ indicate <25% difference between experimental and simulated values, and ‘partial’ denotes >40% prediction difference.

2.5.2 Composition-Depth profiles: experimental and modeling

Figure 2.33 shows the nitrogen and carbon composition-depth profiles of gas nitrocarburized Fe-0.8C (wt. %) and Fe alloys. In the compound layer, the concentration of nitrogen is higher than the carbon concentration during the nitrocarburizing treatment. This situation can arise when the carbon and nitrogen content in the compound layer cannot be altered independently of each other.

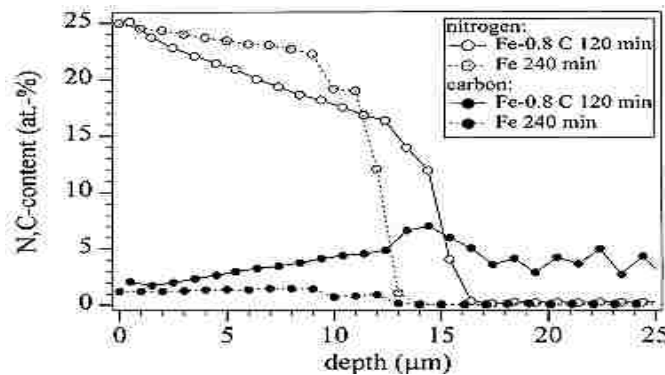


Figure 2.33: Nitrogen and carbon concentration profiles measured using EPMA on nitrocarburized Fe-0.8C (wt. %) and Fe alloys [68].

Grafen and Edenhofer [69] have reported a method to overcome this problem by dividing the nitrocarburizing process in two parts: the first part will have $\text{NH}_3 + \text{CO}_2 + \text{N}_2$ gases to increase the nitrogen content while the second part consists of $\text{NH}_3 + \text{C}_3\text{H}_8 + \text{N}_2$ gases to increase the carbon content in the compound layer (see Fig. 2.34).

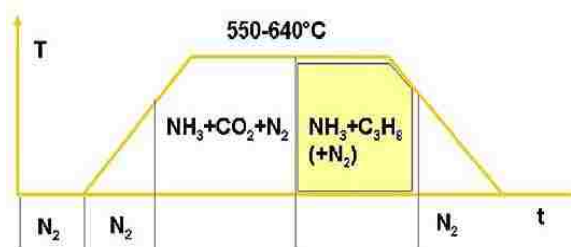


Figure 2.34: Special ferritic nitrocarburizing (FNC) process for increased N_2 and C contents [69].

Many researchers have investigated the composition-depth profiles during nitriding/nitrocarburizing treatments to predict the compound layer growth. Yang and Sisson Jr. [70] simulated the compound layer growth kinetics of nitrided AISI 4140 steel. In their work, the N concentration was measured at four different locations (labelled as 1, 2, 3 and 4 in Fig. 2.35) within the surface layer and the solid (red) line indicates the simulated nitrogen concentration profile. The simulated profile showed good agreement with the measured results.

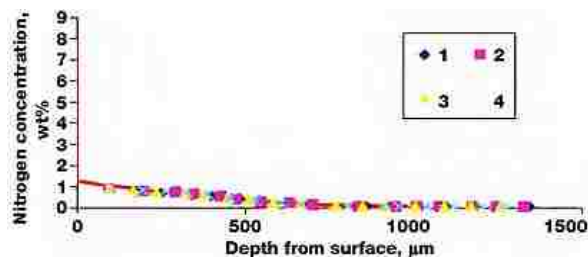


Figure 2.35: Nitrogen concentration profile for nitrided 4140 steel (measured vs. computed) [70].

Keddam [71] presented a kinetic model to simulate the pulse plasma nitriding process using Fick's laws of diffusion. He developed a computer simulation program using Turbo-Pascal language to predict the nitrogen composition profiles at two temperatures (see Fig. 2.36).

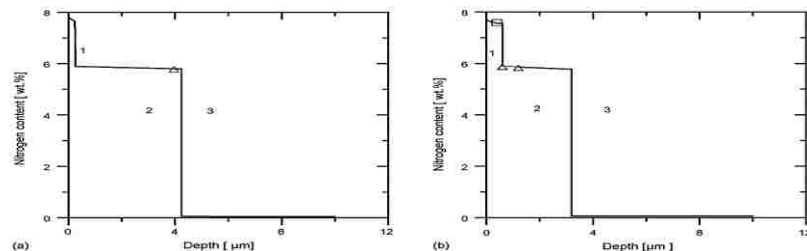


Figure 2.36: Predicted nitrogen composition-depth profiles for pulse plasma nitride pure iron. The experimental data (Δ symbol) were acquired from Yan et al. [72], (a) $T=773\text{K}$ (500°C) & (b) $T=793\text{K}$ (520°C) (1 represents ϵ phase, 2 is γ' and 3 represents α phase) [71].

The model was limited to the compound layer only and the diffusion layer was not included in the model. The regions 1, 2 and 3 in Fig. 2.36 helps to identify the ϵ/γ' interface and γ'/α interface in the nitrogen profiles. The thickness of the nitrided phases was found to decrease with the increase in process temperature (500 to 520°C).

Finite difference approximation is the most widely known technique used for simulating the composition profiles of nitriding/nitrocarburizing steels. Gu et al. [73] performed a numerical simulation of nitrogen and carbon composition-depth profiles using the finite difference method with the Crank-Nicolson algorithm. The Crank-Nicolson algorithm is an advanced implicit integration scheme proposed by Crank and Nicolson in 1947 [74]. It is unconditionally stable and produces better truncation error than the basic implicit method [75]. Figure 2.37 shows the simulated and experimental composition profiles for low-temperature plasma nitrocarburized (430°C/30hrs) austenitic stainless steel. The blue line indicates the nitrogen composition and the red line indicates the carbon composition. The blue and red dots represent the experimental data measured using glow discharge optical emission spectroscopy (GDOES). The general trend of the carbon and nitrogen composition profiles agree well.

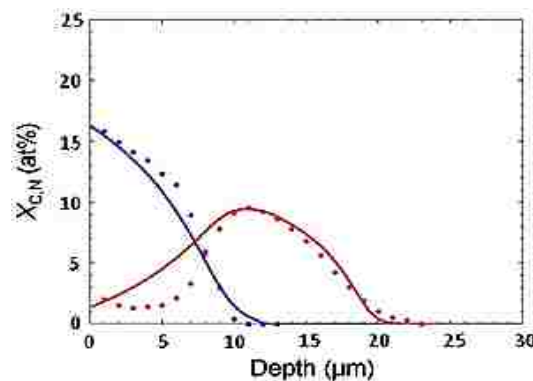


Figure 2.37: Predicted and experimental nitrogen, carbon composition profiles of plasma nitrocarburized austenitic stainless steel [73].

Another example of nitrogen-depth profile simulation using a finite difference method (Crank-Nicolson) is shown in Figure 2.38. The nitrogen profile in plasma nitrided (400°C/2hrs) AISI 316L steel was experimentally obtained by GDOES. The diffusion coefficient values (D_0) of nitrogen were changed to predict the best profile approximation. By comparing the experimental and simulated profiles, Moskaliuviene et al. [76] calculated the best fit (black line) at $D_0 = 0.837 \times 10^{-3} \text{cm}^2/\text{s}$. It was found that the nitrogen penetration depth and nitrogen diffusivity depends on the crystalline orientation of AISI 316L steel (see Fig. 2.38 (b)).

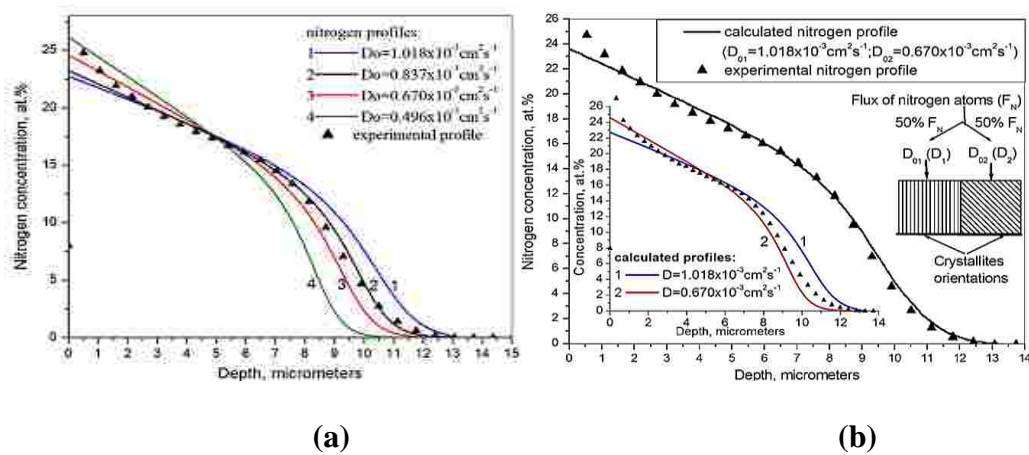


Figure 2.38: Simulated and experimental nitrogen depth profiles of plasma nitrided AISI 316L (400°C/2hrs) with different N diffusion coefficients [76].

Torres et al. [77] also developed a numerical model using implicit finite difference approximation to predict the nitrogen profile and distortion during FNC treatments. The model was applied to housing (case 1) and plate-like (case 2) components made of sand-cast ductile iron (Fig. 2.39 (a & b)). They have divided the model into two parts. The first part of the model calculates the nitrogen profile. A second order kinetic reaction was included in the model to account for the formation of nitrides.

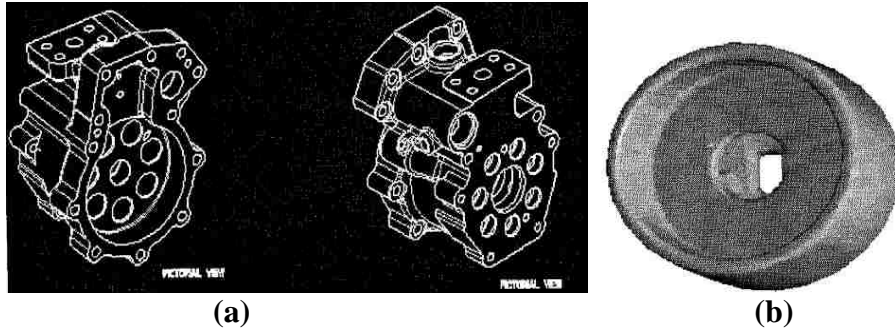


Figure 2.39: (a) schematic of housing, (b) plate-like component

The predicted N composition profile (solid line in Fig. 2.40) was in good agreement with the experimental N profile (measured using GDOES). The second part takes the nitrogen composition profiles as input and executes structural analysis to predict the final distortion (see Fig. 2.41). The bore distortion initially decreases with the distance along the bore, then increases back to the same level.

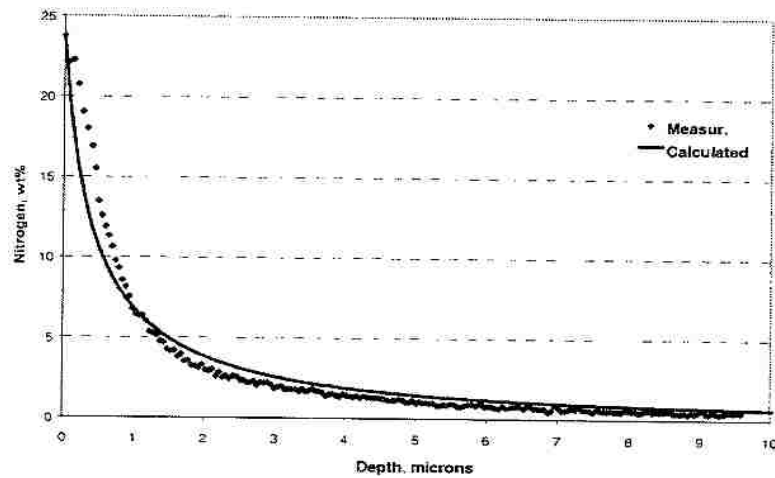


Figure 2.40: Nitrogen composition-depth profiles (measured and calculated) [77].

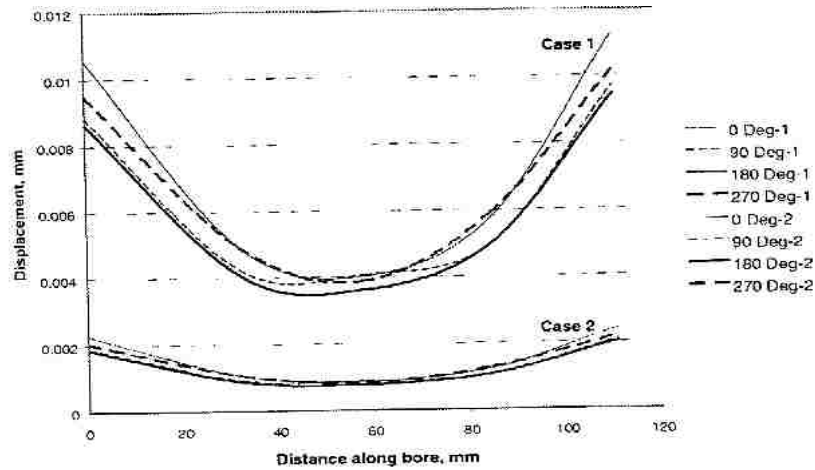


Figure 2.41: Predicted bore deformation for housing (case 1) and plate-like (case 2) components due to 2 different FNC treatments [77].

Table 2.7 summarizes the composition profile modeling procedures reported in section 2.5.2.

Table 2.7: Summary of the composition profile modeling

Study (Ref.)	Materials / Heat treatment	Component of modeling	Agreement with experimental results*
[70]	AISI 4140 steel/heating(843°C/ 1.5hr)+oil quench (54°C)+tempered(579°C/ 3hrs)+nitriding (527°C/10hrs+548°C/ 50hrs)	disk	good
[71]	Pure iron / plasma nitriding(500°C)	15 x 15 x 10mm specimen	partial
[73]	AISI 316L steel / plasma nitrocarburizing (430°C/30 hrs)	--	good
[76]	AISI 316L / plasma nitriding (400°C/2hrs)	--	good
[77]	Sand cast ductile iron / ferritic nitrocarburizing	housing & plate-like	good

* ‘good’ denotes <10% difference between experimental and simulated results, and ‘partial’ denotes incomplete experimental data.

2.5.3 Residual Stress Modeling

Freborg et al. [64] applied an internal state variable (ISV) material model into the DANTE simulation software to predict the residual stress of a notched AMS 6308 steel coupon. The results showed compressive residual stress at the surface, which then tended to become tensile with an increase in depth (see Fig.2.42). There is not much change in the predicted residual stress values up to 0.6mm depth. At 0.6mm, the X-ray measured residual (compressive) stress is almost half of the predicted stress.

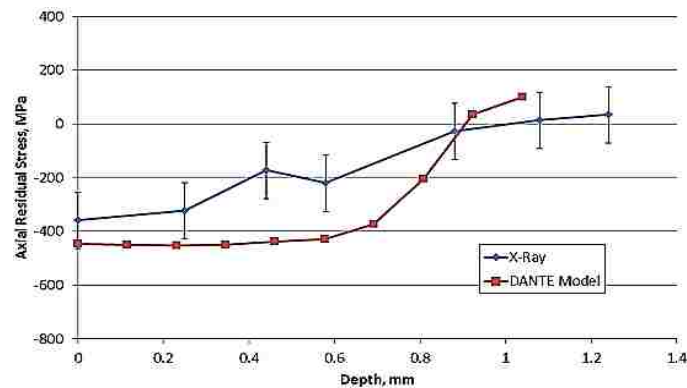


Figure 2.42: Predicted and measured axial residual stress of a carburized AMS 6308 steel coupon [64].

Depouhon et al. [78] developed a nitriding model to predict the residual stresses of 32CrMoV13 low alloy steel. The model has two sections: the chemical calculation was solved by diffusion-reaction-convection model and the mechanical calculation by elasto-visco-plasticity model. Figure 2.43 shows the predicted hoop residual stress and residual stress profiles after gas nitriding. The model predicts a compressive stress of approximately 500 MPa at the nitrided surface, and tensile stresses in the bulk material.

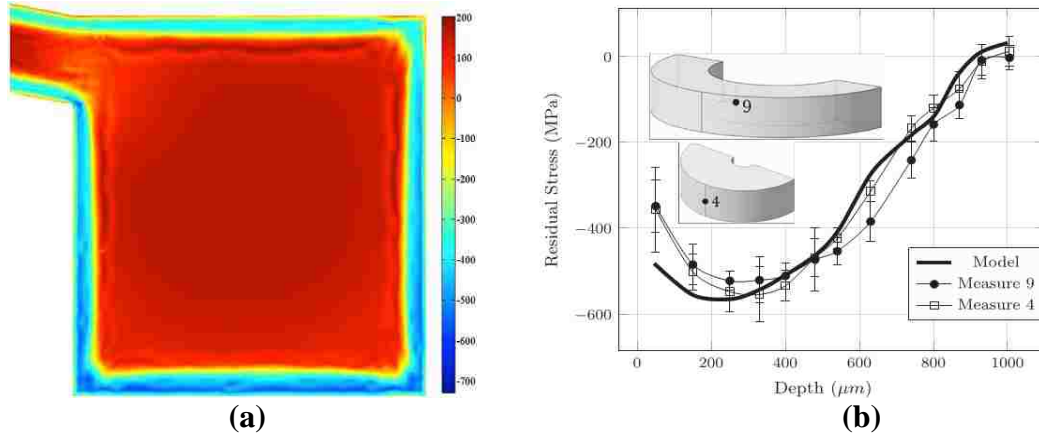


Figure 2.43: (a) – Predicted hoop residual stress map (MPa), (b) - Residual stress-depth profiles for a gas nitrided (550°C/120 hrs) tubular sample [78].

A multiphase material model was developed using ABAQUS (finite element code) with DANTE user subroutines to simulate the residual stresses of a carburized Almen strip [79]. Almen strip (100 mm long and 20 mm wide) is a calibration test specimen used to quantify the residual stresses. The experimental residual stress points in Figure 2.44 were measured using X-ray diffraction [80]. Although the residual stress data (experimental) was not completely measured, a partial agreement exists between experimental and simulated residual stresses.

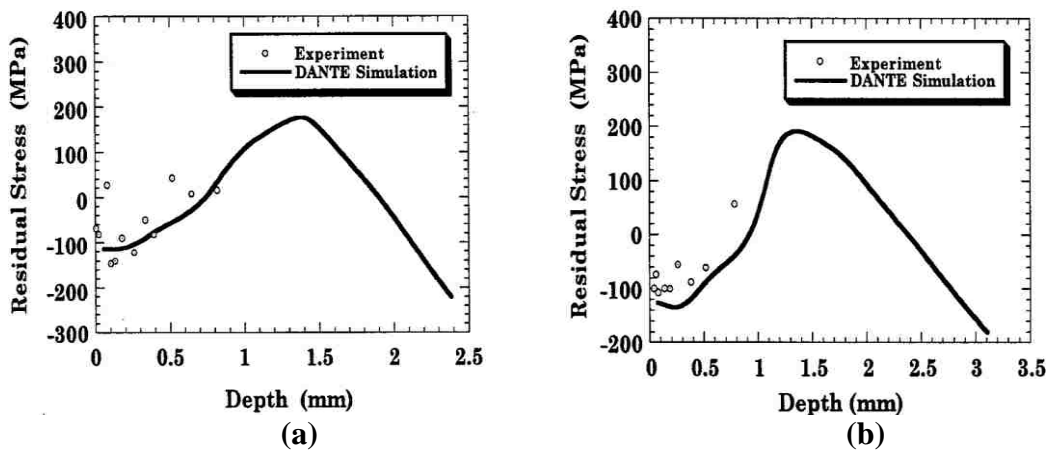


Figure 2.44: Residual stress-depth profiles at the center of the Almen strip, (a) 2.44 mm thick and (b) 3.18 mm thick [79].

The residual stress gradients of a nitrided Fe-Al specimen was studied using a cross-sectional transmission X-ray micro-diffraction technique [81]. It was reported that the Fe-Al specimen cutting can relax the residual stress in the near-surface region. FEM simulations were developed to estimate the residual stress relaxation using ABAQUS software. In the FEM model, the stress profile was varied until the predicted stress was equal to the experimentally measured residual stress. The solid line in Figure 2.45 represents the predicted residual stress of the cross-sectional specimen using FEM. The residual stress profiles were divided into five regions (I, II, III, IV and V) to understand the stress gradients. The un-nitrided core (region V) with zero nitrogen has low tensile stress. With the increase in nitrogen composition, compressive residual stress is developed in region IV, III and II, but region I ended up with tensile residual stress at the surface. The results showed that the misfit accommodation of incoherent AlN precipitation was realized plastically. The AlN phase in Fe-Al specimen is similar to the γ' (Fe_4N) phase in nitrided/nitrocarburized carbon steels.

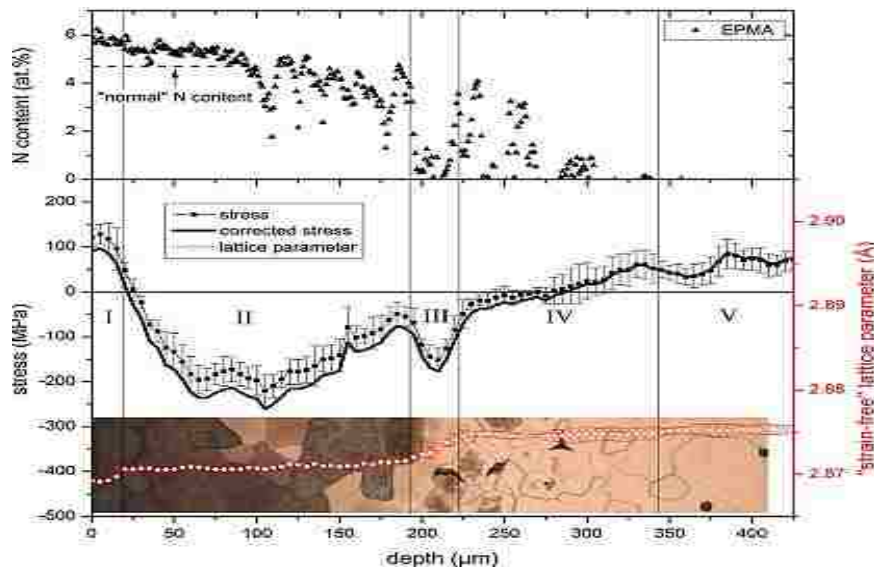


Figure 2.45: Residual stress-depth profiles for the nitrided Fe-Al specimen (experimental and predicted) [81].

Table 2.8 summarizes the residual stress-depth profile modeling discussed in section 2.5.3.

Table 2.8: Summary of the residual stress-depth profile modeling

Study (Ref.)	Material / Heat treatment	Component of modeling	Agreement with experimental results
[64]	AMS 6308 steel / carburizing + anneal + austenitize + gas quench (10 bar N ₂) + deep freeze + double temper	notched coupon	partial
[78]	32CrMoV13 steel / gas nitriding (550°C/120hrs)	tubular plate	good
[79]	SAE 4023 & SAE 4620 steel / carburizing (927°C/7.5hrs+899°C/2hrs+871°C/1.3hr) + oil quench (177°C) + air cool (25°C)	Almen strips	partial
[81]	Fe-4.7 at.% Al / recrystallized (800°C/20min)+gas nitriding (550°C/30hrs)+water quench	rectangular specimen	good

* ‘good’ denotes <10% difference between experimental and simulated results, and ‘partial’ denotes >40% prediction difference.

CHAPTER 3 ANALYTICAL APPROACH

The main goal of this research is to minimize the distortion and residual stress associated with the ferritic nitrocarburizing treatment for SAE 1010 plain carbon steel specimens. To calculate the distortion behaviour, two different specimen types were used, namely: Navy C-ring (probe) and a torque converter (TC) piston (automotive component). Navy C-rings were simply used as a measuring tool to observe the geometrical variations due to the ferritic nitrocarburizing process. Figure 3.1 is an overview of the research plan for evaluating the distortion of Navy C-rings and torque converter (TC) pistons and subsequent validation of the simulation results.

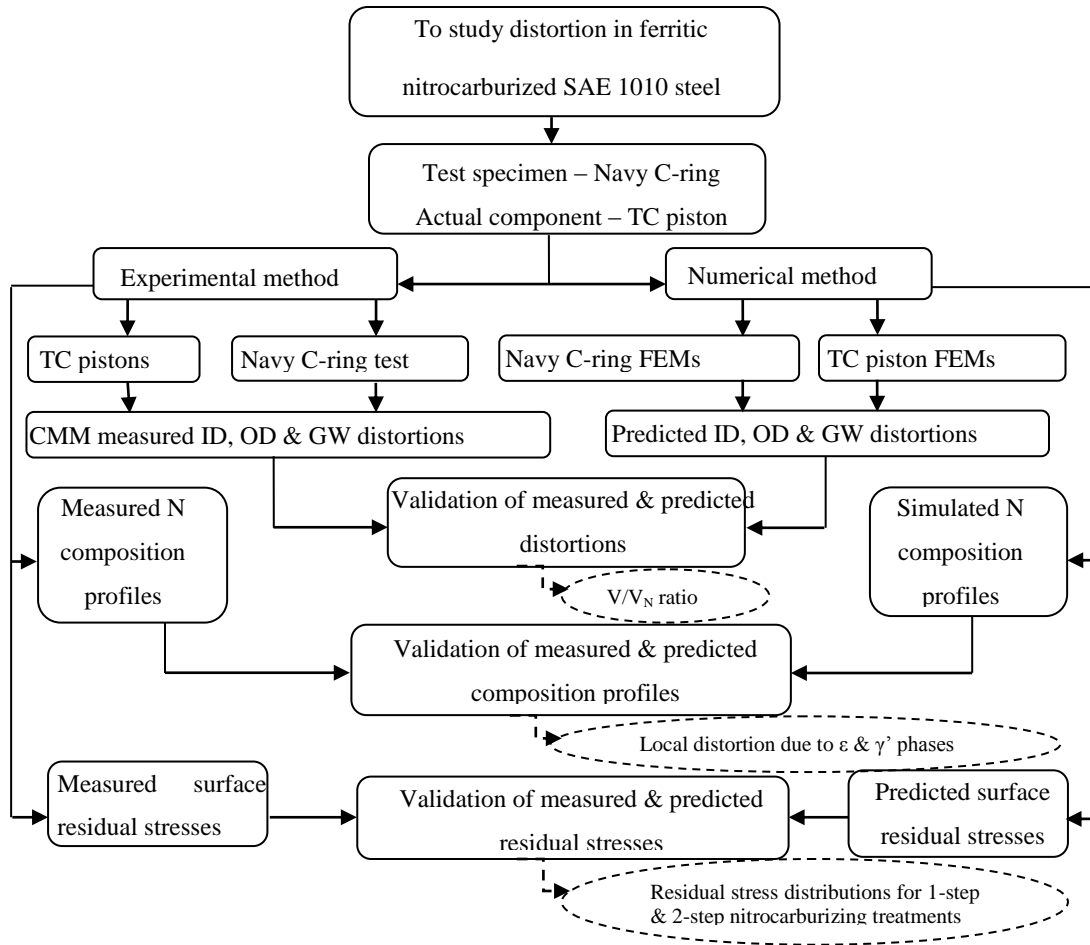


Figure 3.1: Overview of the research plan.

Torque converter (TC) is used to transmit power from an engine/motor to a rotating drive load. The components of torque converter include: a pump impeller, a turbine runner, a stator, and a piston [16]. TC piston (lockup clutch) is used to eliminate the energy loss due to difference in rotational speeds of turbine and the impeller. TC piston is ferritic nitrocarburized to improve the fatigue strength and wear resistance. Figure 3.2(a, b) shows a typical torque converter (TC) and cross section of a torque converter and piston.

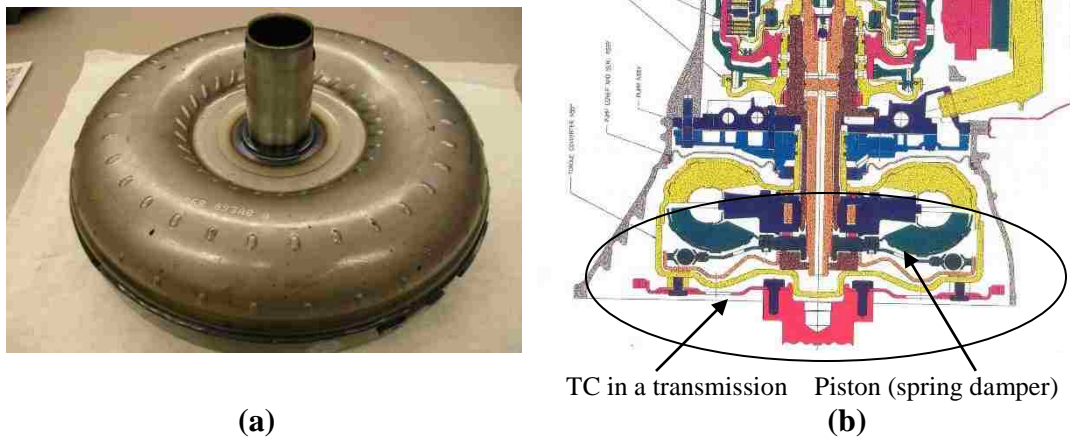


Figure 3.2: (a) Torque converter (TC), and (b) TC cross section [82].

3.1 Distortion reduction

The first part of the research deals with the distortion reduction of nitrocarburized SAE 1010 steel specimens. To solve the distortion problem, three different Navy C-ring specimens (thickness: 19, 10, 2.8mm) and torque converter (TC) piston specimens were used in the experimental and numerical methods. Navy C-ring probes were mainly chosen to analyze the effect of its thickness on distortion.

3.1.1 Navy C-ring geometry

The Navy C-rings were cut from a bar stock of hot rolled SAE 1010 steel using electrical discharge machining. Figure 3.3 (a, b & c) shows the geometry of three C-rings (C1, C2 and C3) that were used to calculate the distortion.

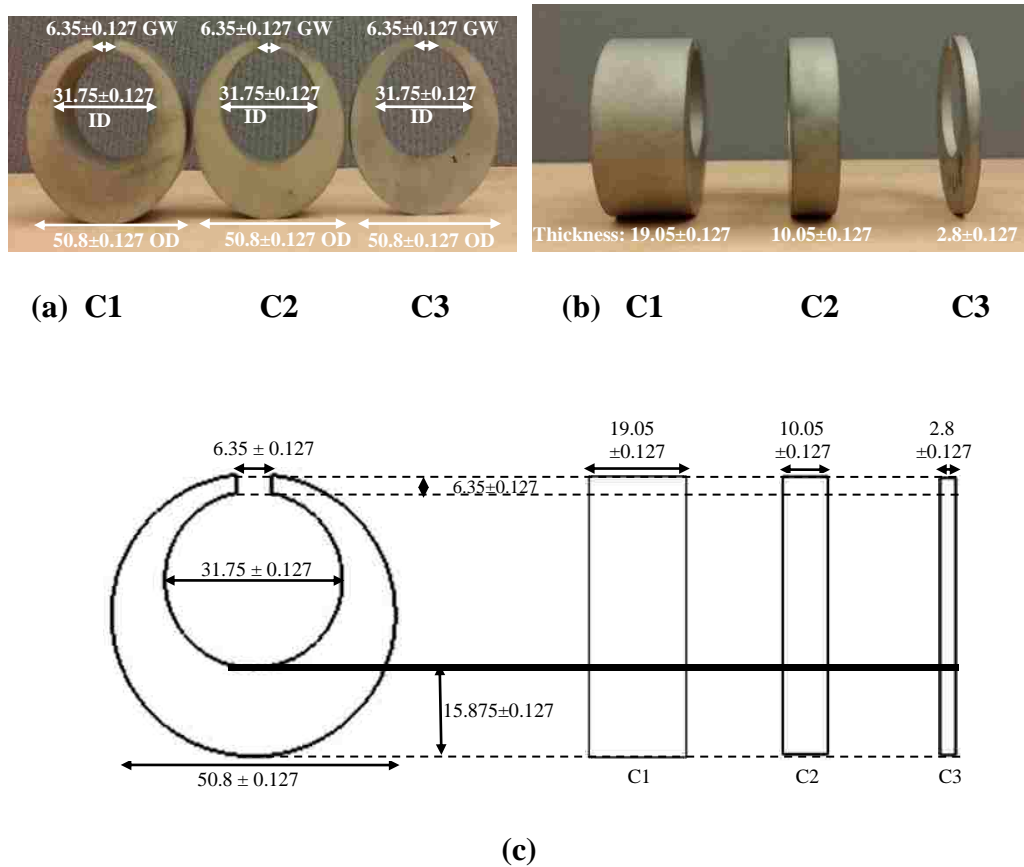


Figure 3.3: (a, b) Navy C-ring specimen geometry, (c) schematic for Navy C-rings C1, C2 and C3 (dimensions in mm).

3.1.2 Materials

The chemical composition of SAE 1010 plain carbon steel specimens used in the present work is listed in Table 3.1:

Table 3.1: Elemental compositions of SAE 1010 plain carbon steel [44]

Element	Wt. %
Carbon (C)	0.12
Manganese (Mn)	0.43
Phosphorus (P)	0.008
Sulfur (S)	0.008
Silicon (Si)	0.03
Chromium (Cr)	0.03
Nickel (Ni)	0.01
Molybdenum (Mo)	0.01
Copper (Cu)	0.02
Plumbum (Pb)	Not detected
Aluminum (Al)	0.052
Vanadium (V)	0.001
Columbium (Cb)	Not detected
Titanium (Ti)	0.002
Cobalt (Co)	Not detected
Tin (Sn)	Not detected
Boron (B)	0.0003
Calcium (Ca)	0.0001
Zirconium (Zr)	Not detected
Tungsten (W)	Not detected

3.1.3 Torque converter piston fabrication

Cold-worked SAE 1010 steel sheets (2.8 mm thick) were used to produce torque converter (TC) pistons. The SAE 1010 sheets underwent a progressive five-stage stamping operation to fabricate them into TC pistons [16]. Torque converter pistons were then subjected to various ferritic nitrocarburizing processes. They have an outer diameter

(OD) of 260 mm and an inner diameter (ID) of 60 mm. Figure 3.4 shows the SAE 1010 steel torque converter (TC) piston geometry.

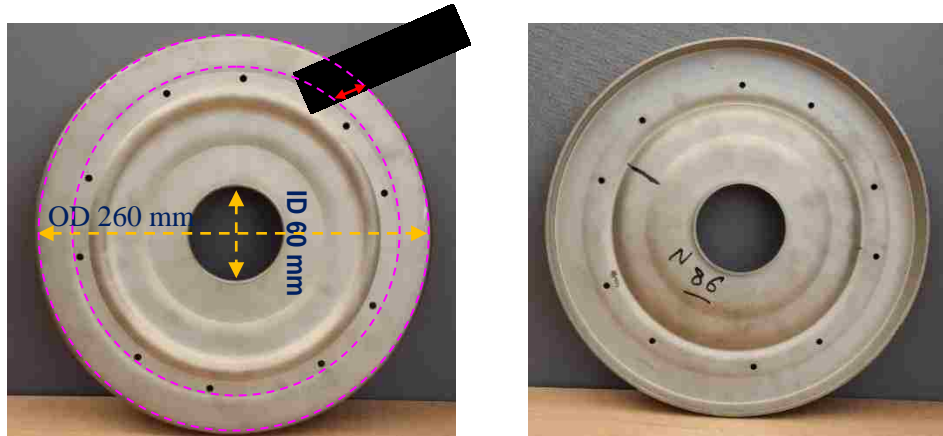


Figure 3.4: Geometry of torque converter (TC) piston.

3.1.4 Heat treatment conditions

The basic process scheme of a ferritic nitrocarburizing process is given below (Fig. 3.5).

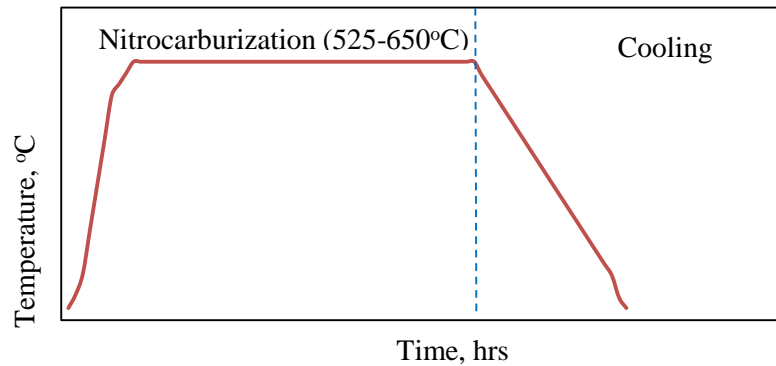


Figure 3.5: Schematic process diagram of the ferritic nitrocarburizing treatment.

Table 3.2 lists the heat treatment processes that were used in the experimental and numerical methods. For each of the gas ferritic nitrocarburizing (FNC) treatments, six Navy C-rings with three different thicknesses were used for measuring the distortion. The total number of torque converter (TC) pistons used for each FNC treatment is ten.

Table 3.2: Heat treatment and specimen details

Heat treatment		No. of specimens used
Gas ferritic nitrocarburizing	595°C/ 4hrs + air cooled to room temperature	Navy C-rings: 6 TC pistons: 10
	565°C/ 5hrs + air cooled to room temperature	Navy C-rings: 6 TC pistons: 10
Vacuum ferritic nitrocarburizing	580°C/ 10hrs + air cooled to room temperature	TC pistons: 10

3.1.5 Sample preparation and optical microscopy

An optical microscope (Leitz Laborlux 12 ME) was used to analyze the microstructure of the SAE 1010 TC piston samples after ferritic nitrocarburizing (FNC) treatments (see Fig. 3.6). Small sections were cut from the heat treated TC pistons and mounted in blue diallyl phthalate powder using a Buehler Simplimet mounting press. The mounted samples were then ground using 240, 320, 400, 600 and 1200 grit silicon carbon papers. After grinding, samples were polished using 1.0 μm and 0.5 μm alumina powder suspended in distilled water. The TC piston samples were then etched using 3.5% Nital solution for 10-15 seconds, followed by a water rinse and ethanol. The following magnifications were used to finally examine the specimens: 200X, 500X and 1000X.



Figure 3.6: A light optical microscope (Leitz Laborlux 12 ME).

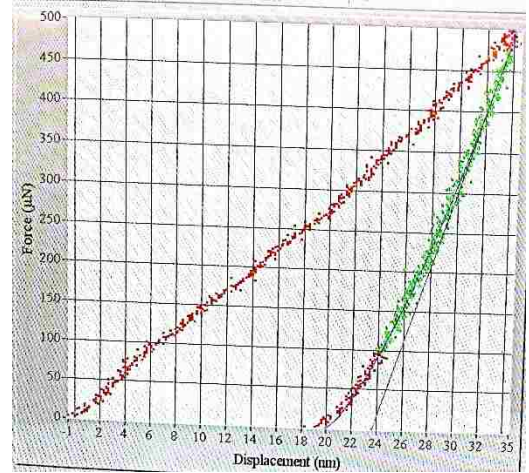
Nitrocarburized microstructures showed a compound layer containing ϵ -phase ($\text{Fe}_{2-3}(\text{C}, \text{N})$), diffusion zone containing γ' -phase (Fe_4N), and ferrite in the core. The thickness of the compound layer was then measured for different heat treated samples.

3.1.6 Nano-indentation measurements

Nanoindentation testing was used to calculate the Young's modulus values of the compound layer and core material (SAE 1010). Figure 3.7(a) shows the instrument used for nanoindentation (Hysitron Ubi1) in SAE 1010 steel samples. The indentation load is applied from 0 to $500\mu\text{N}$ and then from $500\mu\text{N}$ back to $0\mu\text{N}$. When the load is removed from the indenter ($500\mu\text{N}$ back to $0\mu\text{N}$), the specimen will try to recover back to its original shape due to the elastic strain relaxation. However, the specimen is unable to fully recover due to plastic deformation. The Young's modulus of the specimen is calculated from the slope of the unloading curve of the load-displacement response (see Fig. 3.7(b)). The depth of indenter penetration was $\sim 40\text{nm}$.



(a)



(b)

Figure 3.7: (a) Hysitron (Ubi1) nanomechanical instrument, (b) loading-unloading response for a SAE 1010 C-ring after FNC.

3.1.7 Experimental distortion measurements

The distortion of C-ring and TC piston specimens were measured using a PRISMO coordinate measuring machine (CMM) (refer Fig. 3.8). The inner diameter (ID), outer diameter (OD) and gap width (GW) dimensions were measured by conducting contact scans on the specimen surface using a mechanical set-up probe. The specimen features were scanned using Imageware Surface scanning software. The dimensional accuracy was 0.1 microns.

The ID and OD dimensions were recorded at multiple locations along each specimen before and after ferritic nitrocarburizing (FNC) treatment. The ID dimension of the TC piston specimen was measured at 15mm below the lockup surface and the OD dimension was measured at 21.5mm below the lockup surface of the TC piston.

The C-ring's GW dimension was measured at top, middle and bottom positions of the gap width. The difference in ID, OD and GW dimensions (after FNC – before FNC) were then calculated for each specimen, and their average values were finally obtained as geometric distortions.



Figure 3.8: PRISMO coordinate measuring machine (CMM) [83].

3.1.8 Numerical (FEM) *distortion prediction*

The predicted distortions were calculated from the finite element simulations of Navy C-rings and torque converter (TC) pistons. The ID and OD distortions were calculated throughout the inner and outer circumferences of the C-ring model and their average values were compared with the experimental ID and OD (averaged) distortions. The GW distortion was predicted at three locations (top, middle and bottom through the thickness) similar to the experimental GW distortion of the C-rings. The details about the Navy C-ring FEM models, TC piston FEM models and the distortion results are discussed in detail in Chapter 4 and 5.

In addition to the predicted ID (inner diameter), OD (outer diameter) and GW (gap width) distortions, a composition-depth profile simulation model was developed to predict the local distortion due to ϵ & γ' phases (see Chapter 6). The local distortion due to the nitrocarburized phases will help to better understand and control the distortion behavior.

3.1.9 Composition-depth profile numerical simulation

The nitrogen composition-depth profiles were calculated numerically using finite difference method (FDM). The numerical models are addressed in Chapter 6. Figures 3.9 and 3.10 show the schematic diagrams for the simulated nitrogen composition-depth profiles due to 1-step and 2-step nitrocarburizing treatments. The simulated composition-depth profiles of 1-step and 2-step nitrocarburizing treatments were used to calculate the compound layer (CL) thickness and local distortion due to ϵ and γ' phases.

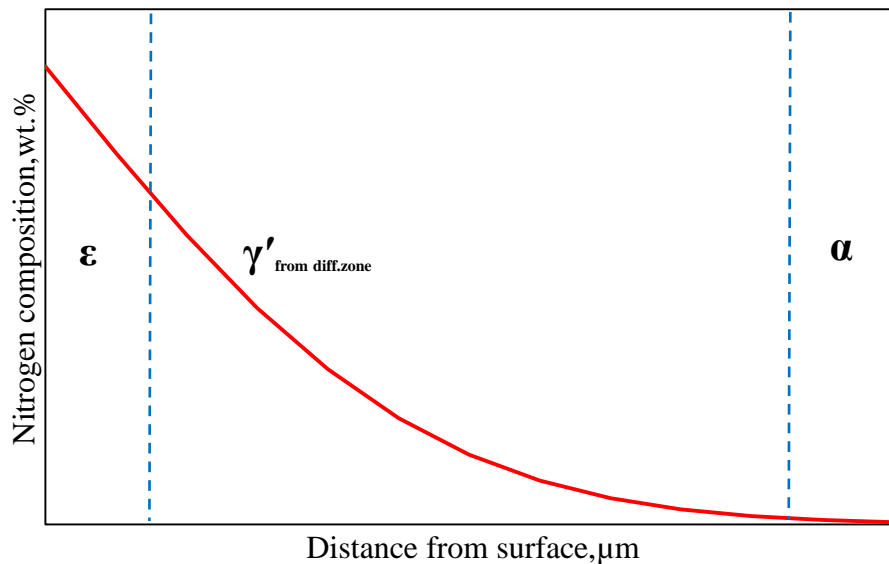


Figure 3.9: Schematic of nitrogen composition-depth profile due to 1-step nitrocarburizing treatment.

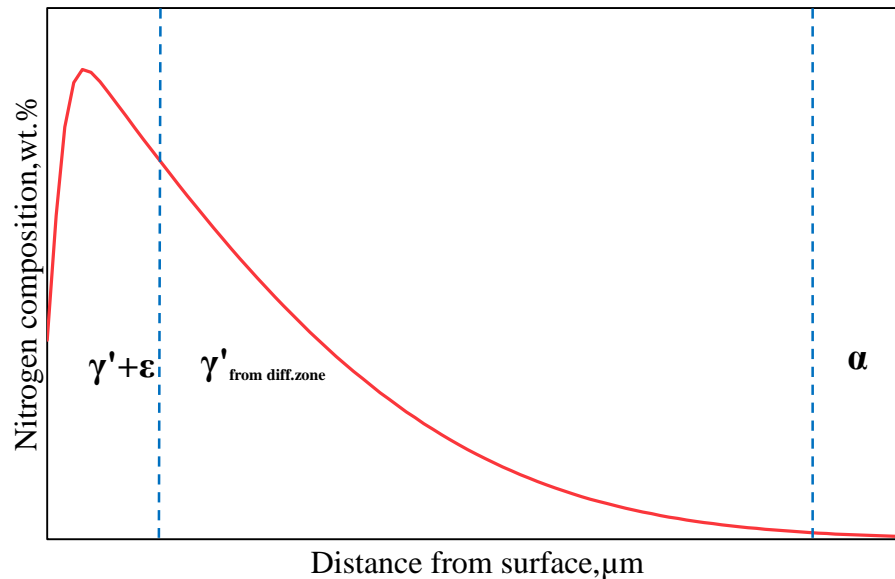


Figure 3.10: Schematic of the simulated nitrogen composition-depth profile due to 2-step nitrocarburizing treatment.

3.1.10 Composition-depth profile measurements (experimental)

Using electron probe micro analysis (EPMA), quantitative elemental analysis can be performed at a very small spot size. It is commonly used to analyze geological materials. Nitrogen and carbon composition profiles of ferritic nitrocarburized TC piston samples were measured experimentally using a CAMECA SX50 electron probe micro analyzer (EPMA) at the Earth Sciences Department, University of Toronto (see Fig. 3.11).

Point analysis along a linear direction was performed on nitrocarburized TC piston samples perpendicular to the surface. A total of 15 point locations were selected in the compound layer (on both the sample ends) and core material to measure the

intensities. The measured intensities were then compared with a standard of known nitrogen and carbon compositions to conduct the quantitative chemical analysis.



Figure 3.11: Cameca SX50 Electron Probe Micro Analyzer (EPMA) at Earth Sciences, University of Toronto [84].

3.2 Reduction in surface residual stress

The second part of research deals with the reduction of surface residual stresses in TC piston specimens after ferritic nitrocarburizing. The surface residual stresses due to 1-step ferritic nitrocarburizing were predicted and validated against the experimentally measured stresses. The results showed tensile residual stresses at the TC piston surface. In order to further reduce the surface (tensile) stress, the residual stress distributions for the nitrocarburized phases were simulated for a set of 2-step nitrocarburizing treatments (refer to Chapter 6).

CHAPTER 4 NUMERICAL SIMULATIONS FOR NAVY C-RINGS AND TORQUE CONVERTER PISTONS

Experimental methods require several repetitions to obtain improvements in heat treatment processes [85]. Repeated experiments are time consuming and expensive. To overcome this problem, simulation tools are developed. Numerical simulations using the finite element method (FEM) are widely used in the automotive industry to save time and reduce cost in manufacturing processes. The accuracy of the simulation results depend on providing the correct material data.

Distortion resulting from heat treatment can be calculated using numerical methods. Two dimensional and three dimensional finite element models were developed to simulate the heat treatment conditions and to investigate the effect of Navy C-ring and torque converter (TC) piston geometries on distortion.

4.1 Material Properties

An isotropic fully elastic material model was selected for the Navy C-rings and torque converter (TC) pistons. Table 4.1 lists the material properties (Young's modulus, Poisson's ratio, thermal expansion coefficient) of the compound layer and bulk material (SAE 1010 steel) used in the FEM models. The Young's modulus values were measured using nano-indentation test. The mean thermal expansion coefficient values were taken from the literature [86, 87]. The density of SAE 1010 steel is $7.872 \times 10^3 \text{ kg/m}^3$ [86, 88].

The material model has been selected as elastic only, because the maximum yield strength (from the simulated models) of the C-ring and TC piston are calculated as 78.55

MPa and 54.96 MPa respectively. At 600°C and room temperature, the yield strength of the SAE 1010 steel are 110 MPa and 305 MPa respectively [89, 90] . Therefore, the maximum calculated stress do not exceed the yield strength of 1010 steel.

Table 4.1: Material properties used in the FEM models

Material	Young's Modulus (E), GPa	Poisson ratio (ν)	Mean thermal expansion coefficient ($\times 10^{-6}$), °C ⁻¹
Compound layer	205	0.29	7.62 (25°C)
Bulk material (SAE 1010)	192	0.29	14.6 (0-600°C)

For a low carbon steel ($C < 0.3\%$), the variation of Young's modulus values with temperature was found to be less than 20% [91]. Therefore, in the FEM models, the Young's modulus values were assumed constant and do not vary with temperature.

4.2 Navy C-ring Probe

Three different Navy C-rings were modeled with dimensions similar to the C-ring geometries (C1, C2 and C3) shown in section 3.1.1. The Inner Diameter (ID), Outer Diameter (OD) and Gap Width (GW) of the C-rings were calculated before and after heat treatment simulations. Figure 4.1 shows the Navy C-ring dimensions used in the FEM models.

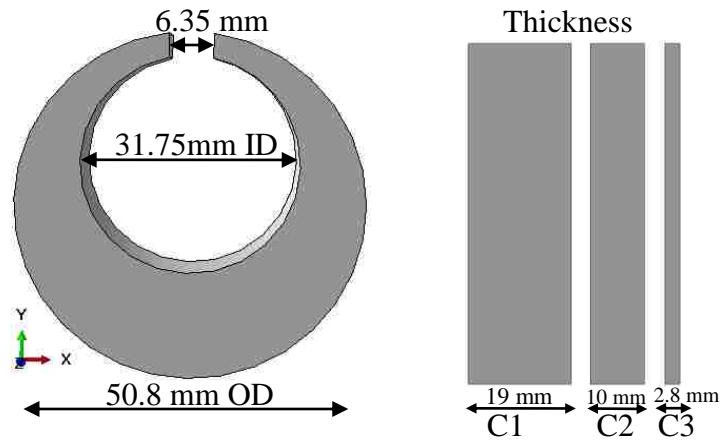


Figure 4.1: Navy C-ring geometry dimensions

4.3 Navy C-ring Finite Element Models

Finite element simulations of Navy C-rings were developed to predict the distortion of nitrocarburized SAE 1010 steel. Two different heat treatment conditions (565°C/5hrs + air cooling, and 595°C/4hrs + air cooling) were simulated in this study. The C-ring part was partitioned into sections: compound layer and bulk. The compound layer of C-rings were modeled with a thickness of 13.73 μm for 565°C/5hrs+air cooling and 19.12 μm for 595°C/4hrs+air cooling. These thickness values were obtained from the previous work [16]. The material properties of the compound layer and bulk material (SAE 1010) were applied to the modeled sections of the C-ring (refer to Table 4.1). Figure 4.2 compares the modeled C-ring sections with the optical micrograph showing the compound layer.

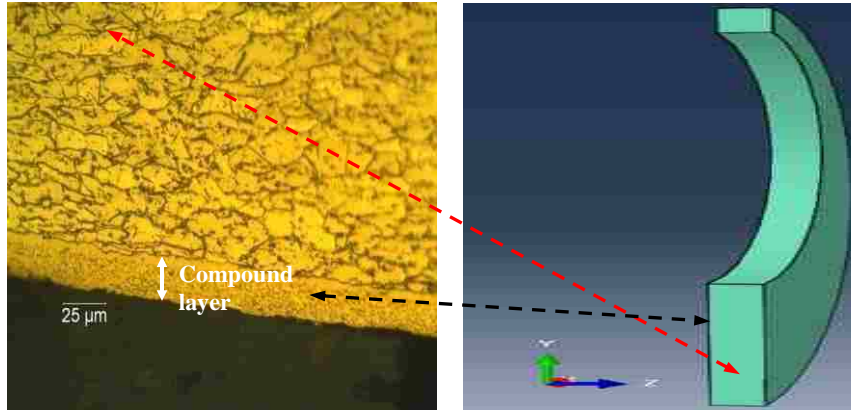


Figure 4.2: Compound layer comparison of the Navy C-ring probe model and the optical micrograph showing the compound layer of SAE 1010 steel.

The heat treatment process involving ferritic nitrocarburizing and air cooling does not involve a phase transformation (in the bulk), so the FEM model will not take into account any phase transformation phenomenon, e.g. austenite to martensite.

4.3.1 Boundary Conditions

Heat transfer that takes place between the material surface and the surrounding environment by convection is related to the heat transfer coefficient as follows:

$$q = h \cdot A \cdot \Delta T \quad (4.1)$$

where h represents the convective heat transfer coefficient ($\text{W}/\text{m}^2\text{°C}$), A denotes the heat transfer area of the surface (m^2), q is the heat transferred per unit time (W), and ΔT denotes the temperature difference ($T_s - T_\infty$) between the surface (T_s) and the fluid (T_∞) (°C). This convective heat transfer coefficient (h) was applied as a thermal boundary condition at all Navy C-ring surfaces in contact with the gas. The heat transfer coefficient used in the model was $200 \text{ W}/\text{m}^2\text{°C}$. In the model, one end of the Navy C-ring half was fixed at the bottom to avoid rigid body motion.

4.3.2 Discretization of the C-ring models

All parts were assigned with a solid section property in ABAQUS (a commercial software). Taking advantage of the C-ring symmetry, only half of the C-ring was modeled. The discretized finite element model of the three different C-rings are illustrated in Figure 4.3. Linear tetrahedral elements of type C3D4T were selected to discretize the C-ring parts. The mesh density of the nitrocarburized layer was kept higher than the bulk material; computer runs with different mesh densities were performed to make sure that numerical solution for the predicted distortion was mesh independent. After several computer runs, it was also found that a variable time step of 10^{-9} to 2000 sec was appropriate for convergence. Table 4.2 shows the mesh sensitivity study for C3 sample. The total number of elements in each of the C-ring model are listed in Table 4.3.

Table 4.2: Mesh sensitivity study in a C-ring (C3) model

Model number	No. of elements	GW distortion (top) (mm)	Relative difference between consecutive iterations (%)
1	114795	-0.0067	--
2	121218	-0.0071	5.6
3	121586	-0.0074	4.1
4	122359	-0.0076	2.6

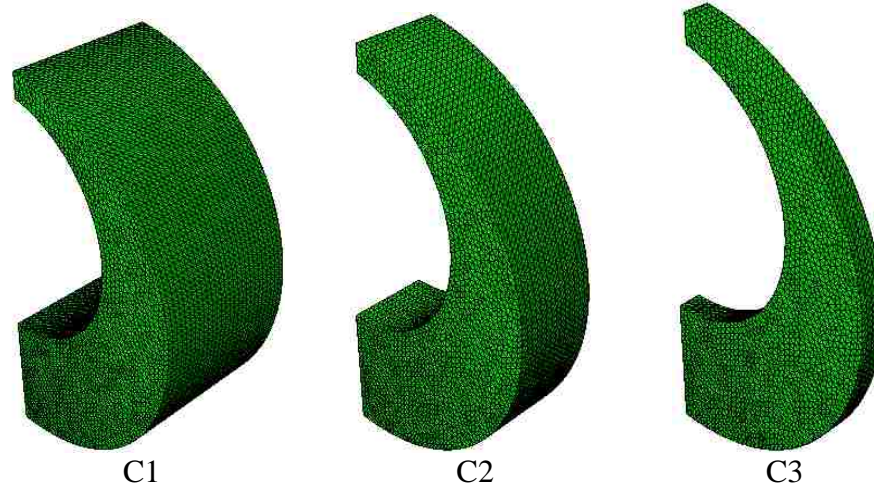


Figure 4.3: Half symmetric geometry of meshed Navy C-rings with varying thicknesses 19mm (C1), 10mm (C2), 3mm (C3).

Table 4.3: Details about the C-ring elements

Specimens	Total number of nodes	Total number of tetrahedral elements
C1	62860	348199
C2	36416	197330
C3	22999	122359

4.4 Simulation Procedure of C-ring models

A total of six FEM C-ring models were developed (two heat treatments per C-ring type). The distortion problem was solved using an explicit time integration scheme. Each FEM model has two operations: heating and cooling (see Table 4.4). The FEM simulation of the C-ring's heating operation involved the prediction of the ring expansion due to the increase in temperature from 27°C to 565°C/595°C. Once expanded at 565 or 595°C for 4-5hrs, the C-ring was considered as completely nitrocarburized by

incorporating the material properties of the ϵ & γ' phases. The expanded C-rings were then passed into the cooling operation (27°C/1.1hr).

Table 4.4: Finite element simulation set up for C-ring models

Operation	Parameter	Value	Simulated compound layer thickness, μm	
			565°C/ 5hrs	595°C/ 4hrs
1 - Heating	Specimens	C-rings (C1, C2, C3)	13.73	19.12
	Material	SAE 1010 steel		
	Initial temperature	27°C		
	Heating temperature/time	565°C/5hrs & 595°C/4hrs		
2 - Cooling	Specimens	Expanded C-rings from operation 1	13.73	19.12
	Initial temperature	565°C & 595°C		
	Cooling temperature/time	27°C/1.1 hr		

4.5 Axisymmetric Torque Converter Piston Model

Finite element simulations (2D axisymmetric model) of torque converter pistons were developed. The torque Converter (TC) piston used in this study has a thickness (2.8mm) which is same as the C3 C-ring type. The same heat treatment conditions that were used for Navy C-rings were used for TC pistons. The piston part was partitioned into two sections: compound layer and bulk. The compound layer section was meshed finer than the bulk material.

The compound layer section was modeled to a thickness of 12.28 μm for 565°C/5hrs+air cooling and 14.22 μm for 595°C/4hrs+air cooling conditions. These thickness values were obtained from the previous work [16]. Similar to the C-ring model,

the material properties of the compound layer and bulk material (SAE 1010) were applied separately. The applied thermal and mechanical boundary conditions were similar to the Navy C-ring probe models. Figure 4.4 (a) & (b) shows the torque converter piston cross section and axisymmetric FEM model. Triangular elements of type CAX6MT were selected to discretize the axisymmetric TC piston.

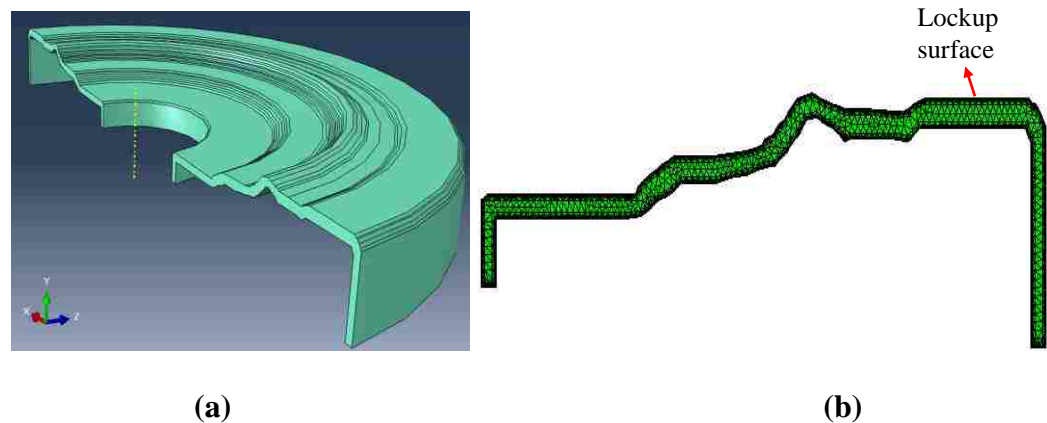


Figure 4.4: (a) Cross section of the torque Converter (TC) piston, (b) axisymmetric TC piston model.

4.6 Simulation procedure of axisymmetric TC piston model

Axisymmetric models were developed using an explicit time integration scheme to simulate the nitrocarburizing processes (565°C/5hrs + air cooling & 595°C/4hrs + air cooling). The heating and cooling job files were set to run with double precision. The expanded piston after the heating operation was predefined as the initial state of the cooling operation. Table 4.5 lists the simulation set-up of the axisymmetric model similar to the C-ring model.

In order to validate the predicted distortion values, the ID distortion was estimated at 11mm below the lockup surface. Similarly, the OD distortion was estimated at 21.5mm below the lockup surface (refer to section 3.1.7).

Table 4.5: Finite element simulation set up for TC pistons

Operation	Parameter	Value	Simulated compound layer thickness, μm	
			565°C/ 5hrs	595°C/ 4hrs
1 - Heating	Specimens	TC piston	12.28	14.22
	Material	SAE 1010 steel		
	Initial temperature	27°C		
	Heating temperature/time	565°C/5hrs & 595°C/4hrs		
2 - Cooling	Specimens	Expanded piston from operation 1	12.28	14.22
	Initial temperature	565°C & 595°C		
	Cooling temperature/time	27°C/1.1 hr		

CHAPTER 5 VALIDATION OF THE FINITE ELEMENT MODELS

5.1 Distortion results of Navy C-rings

The distortion occurs either by expansion or contraction of the C-rings due to heat treatment. Distortion with a negative value indicates the contraction of C-rings after heat treatment. The predicted C-ring distortions were validated against the measured distortions (ID, OD and GW).

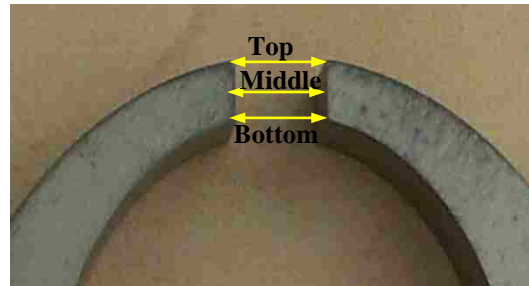


Figure 5.1: C-ring's GW distortion measurement locations

The GW distortion was measured at three different locations using a CMM (see section 3.1.7), which are denoted top, middle and bottom in Fig. 5.1. The C-ring's gap width (GW), OD and ID distortions were calculated from the Navy C-ring FEM models and experimental measurements. The experimentally measured distortion of C-rings were calculated by subtracting the dimensions (ID, OD and GW) after heat treatment from the dimensions (ID, OD and GW) recorded before heat treatment. The C-ring's ID, OD and GW distortion values were then averaged (6 C-rings per heat treatment = 2C1, 2C2 and 2C3, total=12 C-rings) and are reported in Table 5.1. The absolute errors were estimated as the difference between measured and predicted distortion.

$$\text{ID, OD, GW distortion} = \text{ID, OD, GW dimensions (after heat treatment)} - \text{ID, OD, GW dimensions (before heat treatment)} \quad (5.1)$$

$$\text{Absolute error} = |\text{Measured distortion} - \text{Predicted distortion}| \quad (5.2)$$

Table 5.1: Measured ID, OD and GW distortions for nitrocarburized C-rings

Heat treatment	Gas ferritic nitrocarburizing, 595°C/4hrs + air cooling			Gas ferritic nitrocarburizing, 565°C/5hrs + air cooling		
	<i>Specimen ID (thickness)</i> <i>C1 (19mm)</i>	<i>C2 (10mm)</i>	<i>C3 (2.8mm)</i>	<i>C1 (19mm)</i>	<i>C2 (10mm)</i>	<i>C3 (2.8mm)</i>
OD distortion, mm	0.0250	0.0235	0.0278	0.0223	0.0224	0.0193
ID distortion, mm	0.0067	0.0006	-0.0049	0.0064	0.0004	-0.0025
GW distortion (top), mm	0.0067	-0.0148	-0.0085	0.0043	-0.0144	-0.0117
GW distortion (middle), mm	0.0033	-0.0146	--	-0.0002	-0.0174	--
GW distortion (bottom), mm	0.0055	-0.0155	-0.0125	-0.0003	-0.0173	-0.0124

Tables 5.2, 5.3, and 5.4 compares the measured and predicted GW distortion results of the Navy C-rings.

Table 5.2: C-ring's Gap Width (GW) distortion results – Top location

Heat Treatment	C-ring specimens	V/V _N ratio*	GW distortion (mm), <u>Location: Top</u>		
			Measured	Predicted	Absolute error
595°C/4h + air cooling	C1 (19 mm thick)	381	0.0067	-0.0035	0.0102
	C2 (10 mm thick)	200	-0.0148	-0.0109	0.0039
	C3 (2.8 mm thick)	56	-0.0085	-0.0076	0.0009
565°C/5h + air cooling	C1 (19 mm thick)	381	0.0043	-0.0019	0.0062
	C2 (10 mm thick)	200	-0.0144	-0.0042	0.0102
	C3 (2.8 mm thick)	56	-0.0117	-0.0043	0.0074

* defined as bulk volume (V) to nitrocarburized volume (V_N) ratio.

Table 5.3: C-ring's Gap Width (GW) distortion results – Middle location

Heat Treatment	C-ring specimens	V/V _N ratio*	GW distortion (mm), <i>Location: Middle</i>		
			Measured	Predicted	Absolute error
595°C/4h + air cooling	C1 (19 mm thick)	381	0.0033	-0.0076	0.0109
	C2 (10 mm thick)	200	-0.0146	-0.0093	0.0053
	C3 (2.8 mm thick)	56	--	-0.0062	--
565°C/5h + air cooling	C1 (19 mm thick)	381	-0.0002	-0.0073	0.0071
	C2 (10 mm thick)	200	-0.0174	-0.0065	0.0109
	C3 (2.8 mm thick)	56	--	-0.0046	--

* defined as bulk volume (*V*) to nitrocarburized volume (*V_N*) ratio.

Table 5.4: C-ring's Gap Width (GW) distortion results – Bottom location

Heat Treatment	C-ring specimens	V/V _N ratio*	GW distortion (mm), <i>Location: Bottom</i>		
			Measured	Predicted	Absolute error
595°C/4h + air cooling	C1 (19 mm thick)	381	0.0055	-0.0089	0.0144
	C2 (10 mm thick)	200	-0.0155	-0.0070	0.0085
	C3 (2.8 mm thick)	56	-0.0125	-0.0053	0.0072
565°C/5h + air cooling	C1 (19 mm thick)	381	-0.0003	-0.0059	0.0056
	C2 (10 mm thick)	200	-0.0173	-0.0048	0.0125
	C3 (2.8 mm thick)	56	-0.0124	-0.0038	0.0086

* defined as bulk volume (*V*) to nitrocarburized volume (*V_N*) ratio.

Figure 5.2 shows the measured and predicted gap width (GW) profiles for the nitrocarburized Navy C-rings. In all three locations (top, middle and bottom), sample C2

exhibited highest GW distortion than C1 and C2 samples. The predicted GW distortion was in better agreement with the measured GW distortion for sample C2 and C3.

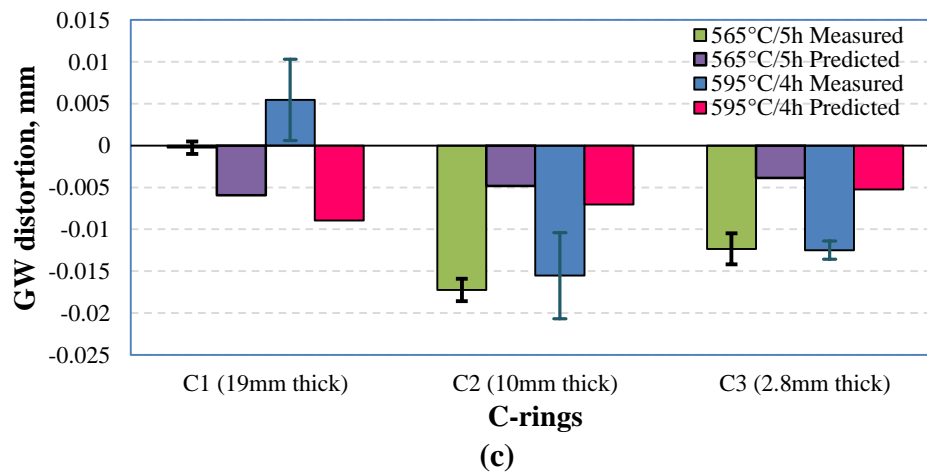
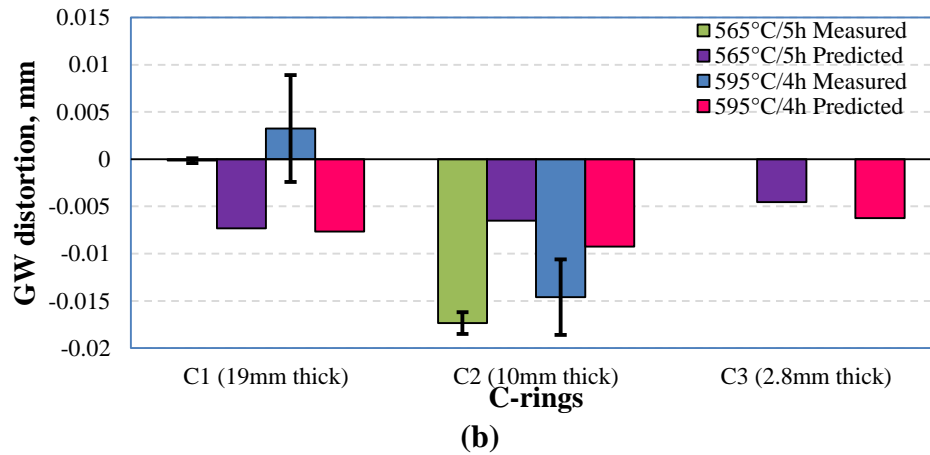
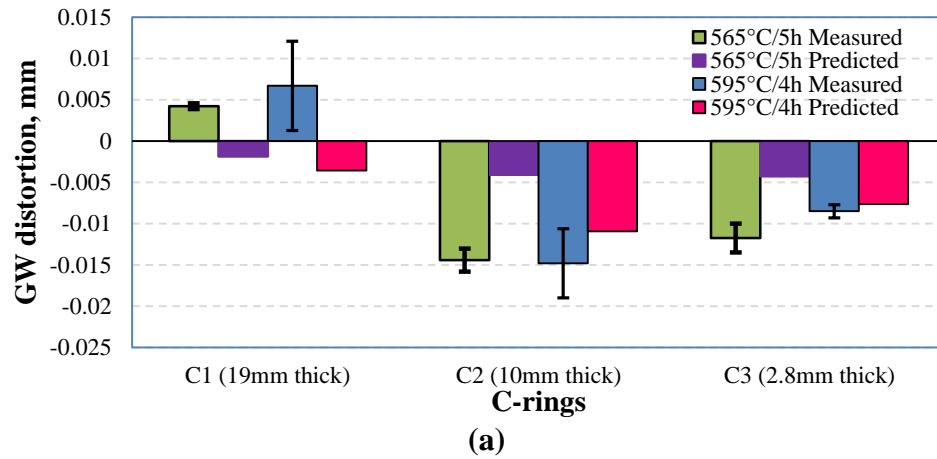


Figure 5.2: Measured and predicted gap width (GW) distortion profiles of Navy C-rings ((a) top, (b) middle & (c) bottom locations).

The predicted GW distortion (top location) of sample C1 showed C-ring gap contraction while the measured distortion showed gap expansion, leading to high error. This could be due to the thickness (19mm) of sample C1. For thicker samples, the distortion contribution due to bulk material (SAE 1010) will be higher than the distortion contribution due to nitrocarburized layer.

The measured OD distortion slightly increased with an increase in process temperature from 565°C to 595°C (see Fig. 5.3). A similar trend profile is observed for the predicted OD distortion. Tables 5.5 and 5.6 lists the OD and ID distortion results (measured & predicted) with the change in heat treatment and C-ring thicknesses. The OD distortion for thicker samples (C1 and C2) resulted in high error, which is similar to the GW distortion results. Figure 5.3 shows the OD distortion profile with the change in C-ring thicknesses.

Table 5.5 Comparison of the measured Outer Diameter (OD) distortion with the predicted OD distortion

Heat Treatment	C-ring specimens	V/V _N ratio*	OD distortion (mm)		
			Measured	Predicted	Absolute error
595°C/4h + air cooling	C1 (19 mm thick)	381	0.0250	0.0088	0.0162
	C2 (10 mm thick)	200	0.0235	0.0064	0.0171
	C3 (2.8 mm thick)	56	0.0278	0.0184	0.0094
565°C/5h + air cooling	C1 (19 mm thick)	381	0.0223	0.0042	0.0181
	C2 (10 mm thick)	200	0.0224	0.0032	0.0192
	C3 (2.8 mm thick)	56	0.0193	0.0016	0.0177

* defined as bulk volume (V) to nitrocarburized volume (V_N) ratio.

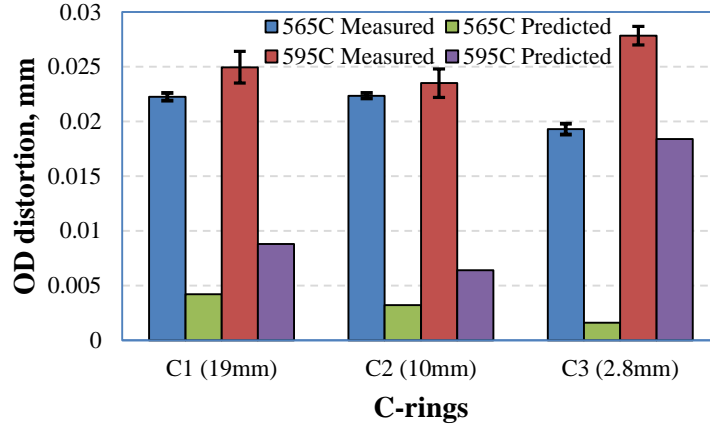


Figure 5.3: Outer Diameter (OD) distortion profile of Navy C-rings (measured and predicted).

There seems to be some sort of uncertainty in the ID distortion of C3 (2.8 mm thick). The error bar of C3 (see Fig. 5.4) is larger than its measured value. Nevertheless, the ID distortion prediction follows similar trend of the measured distortion. The experimental measurements for Navy C-rings have shown that the ID distortion decreases with the decreasing C-ring thickness (from 19 to 2.8 mm). This trend is confirmed by the numerically calculated distortions.

Table 5.6: Comparison of the measured Inner Diameter (ID) distortion with the simulated results

FNC	C-ring specimens	V/V _N ratio*	Inner Diameter (ID) (mm)		
			Measured Distortion	Predicted Distortion	Absolute error
595°C/4h + air cooling	C1 (19 mm thick)	381	0.0067	0.0014	0.0053
	C2 (10 mm thick)	200	0.0006	-0.0024	0.0030
	C3 (2.8 mm thick)	56	-0.0049	-0.0002	0.0047
565°C/5h + air cooling	C1 (19 mm thick)	381	0.0064	0.0010	0.0054
	C2 (10 mm thick)	200	0.0004	-0.0016	0.002
	C3 (2.8 mm thick)	56	-0.0025	-0.0002	0.0023

* defined as bulk volume (V) to nitrocarburized volume (V_N) ratio.

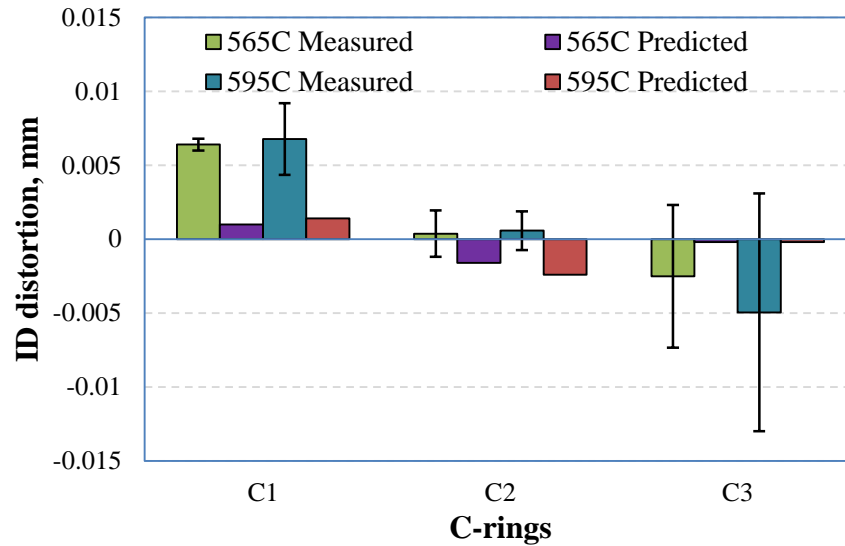


Figure 5.4: Inner diameter (ID) distortion profile of Navy C-rings (measured and predicted).

The Navy C-ring model results show that the distortion is affected by the nitrocarburized surface (compound layer) and bulk (core material) modifications due to heat treatment. The distortion in thinner samples (smaller V/V_N ratio) are controlled by the nitrocarburized layers whereas the distortion in thicker samples are controlled by the bulk. As the FEM simulations of C-rings didn't take into account of the bulk volume modifications and diffusion zone, the simulated distortion for the thicker samples have higher error values than the thinner sample.

5.2 Bulk Volume/Nitrocarburized Volume Ratio

The GW, ID and OD errors decrease with decrease in C-ring thickness (19 to 2.8 mm). Hence, the thickness of the Navy C-ring becomes an important factor when comparing the C-ring distortion with the actual component (TC piston). Based on the

nitrocarburized volume (V_N) and bulk volume (V) (SAE 1010 steel), an empirical ratio (V/V_N) was introduced to identify the effect of distortion on C-ring thickness. According to the V/V_N ratio, the samples were divided into two categories: nitrocarburized volume dominant (C3 & TC) and bulk volume dominant (C1 & C2). Table 5.7 lists the V/V_N ratio of three Navy C-rings (C1, C2 and C3) and torque converter (TC) pistons.

The V/V_N ratio comparisons of the C-ring helps to recognize the magnitude of distortion contribution due to nitrocarburized layer and bulk material of thicker and thinner samples. From the error values (see Figs. 5.5 & 5.6), it is clear that the V/V_N ratio of the C-ring should be lower than 100 to obtain precise distortion prediction. The bulk volume dominant samples (C1 & C2) exhibited higher error than the nitrocarburized surface dominant sample (C3). The decrease in V/V_N ratio caused lower OD, ID and GW distortions. The GW distortion values becomes more negative with the decrease in C-ring thickness. Therefore, the reduction of V/V_N ratio led to an overall gap width (GW) shrinkage.

Table 5.7: V/V_N ratio of Navy C-rings and TC pistons

Sample Name	V/V_N ratio
C1	381
C2	200
C3	56
TC	56

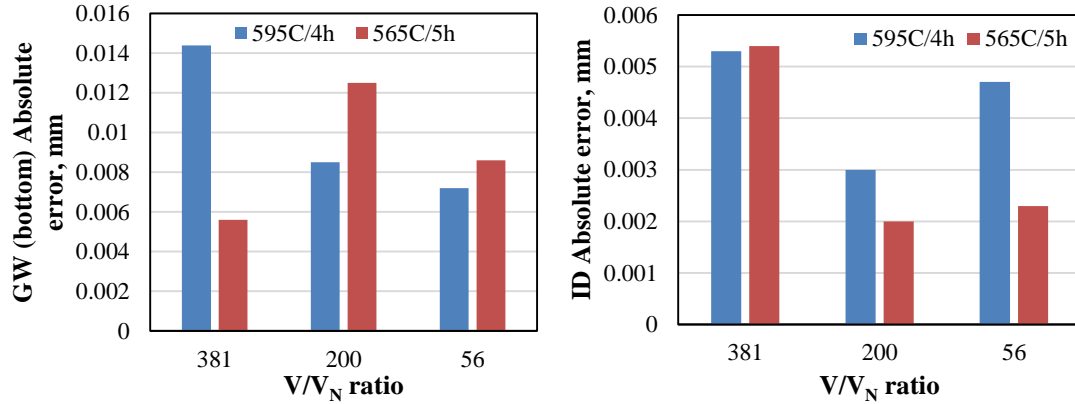


Figure 5.5: V/V_N ratio vs. absolute errors for GW & ID distortions of Navy C-rings.

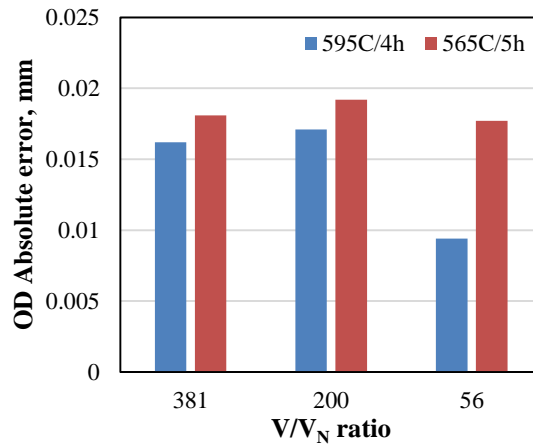


Figure 5.6: V/V_N ratio vs. absolute errors for OD distortions of Navy C-rings.

5.3 Distortion results of torque converter (TC) pistons

The OD and ID distortions for the TC piston specimens (10 specimens/FNC) due to nitrocarburizing treatments are listed in Table 5.8. The distortion values of the ten specimens were averaged and reported as measured distortions.

The OD distortion results showed that the outer diameter of the torque converter piston shrank by reducing the nitrocarburizing temperature from 595°C to 565°C. However, the ID distortion results for both nitrocarburizing treatments showed ID

expansion, and the distortion was found to decrease with the decrease in nitrocarburizing temperature (595°C to 565°C).

The ID distortion of TC pistons were an order of magnitude higher than the ID distortion of C-rings (see Tables 5.6 and 5.7). The OD distortion of C-rings varied from 0.0193mm to 0.0278mm and the OD distortion for TC pistons are in the range of -0.0202mm to 0.0301mm. The ID distortion results showed inner diameter expansion in C-rings (except C3) and pistons. But the OD distortion results showed outer diameter contraction in the TC pistons and expansion in C-rings. This clearly proves that the OD distortion of C-rings behave differently than the TC pistons.

Table 5.8 compares the measured and predicted OD distortions for two FNC treatments (595°C/4h + air cooling and 565°C/5h + air cooling). Although the predicted OD and ID distortions underestimate their measured distortion values (Tables 5.9 & 5.10), a similar decreasing distortion trend (decline in measured distortion) was observed for the predicted values with decrease in nitrocarburizing temperature.

Table 5.8: Experimental ID and OD distortions for nitrocarburized TC pistons

Specimen No.	Gas ferritic nitrocarburizing, 595°C/4hrs + air cooling		Gas ferritic nitrocarburizing, 565°C/5hrs + air cooling	
	OD distortion, mm	ID distortion, mm	OD distortion, mm	ID distortion, mm
1	0.0382	0.0427	-0.0175	0.0318
2	0.0344	0.0417	-0.0281	0.0317
3	0.0317	0.0405	-0.0280	0.0341
4	0.0226	0.0412	-0.0270	0.0301
5	0.0314	0.0438	-0.0301	0.0335
6	0.0409	0.0403	-0.0236	0.0345
7	0.0251	0.0453	-0.0176	0.0336
8	0.0311	0.0414	-0.0095	0.0360
9	0.0264	0.0433	-0.0087	0.0349
10	0.0192	0.0440	-0.0119	0.0341
average	0.0301	0.0424	-0.0202	0.0334

The ID distortion error of TC pistons seems to drop with the decrease in nitrocarburizing temperature (595 to 565°C) but contrasting results were obtained for the OD distortion error. Similar error results were obtained for the C-ring sample C3 which has the same thickness (2.8mm) as TC piston. Therefore, the dimensions of the measuring tool (C-ring) play a significant role in relating the distortion results with an actual component of interest (TC piston).

Table 5.9: Comparison of measured and predicted OD distortion of TC pistons

Sample	FNC	V/V _N ratio	OD distortion, mm		
			Measured	Predicted	Absolute error
TC pistons	595°C/4h + air cooling	56	0.0301	0.0120	0.0181
	565°C/5h + air cooling	56	-0.0202	0.0100	0.0302

Table 5.10: Comparison of measured and predicted ID distortion of TC pistons

Sample	FNC	V/V _N ratio	ID distortion, mm		
			Measured	Predicted	Absolute error
TC pistons	595°C/4h + air cooling	56	0.0424	0.0025	0.0399
	565°C/5h + air cooling	56	0.0334	0.0020	0.0314

CHAPTER 6 COMPOSITION-DEPTH PROFILE SIMULATION MODEL

The nitrogen composition-depth profiles of two heat treatment conditions (gas FNC at 565°C/5hrs and vacuum FNC at 580°C/10hrs) were measured using electron probe micro analyzer (Fig. 6.1).

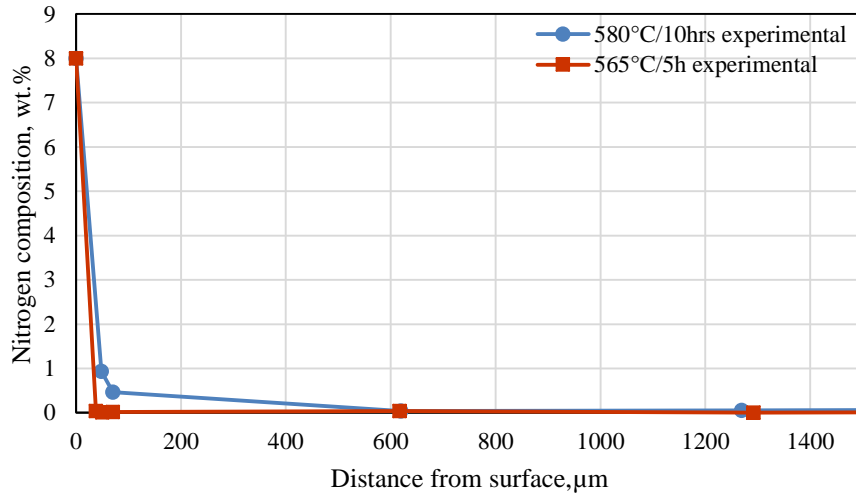


Figure 6.1: Experimental nitrogen profiles for vacuum nitrocarburized (580°C/10hrs) and gas nitrocarburized (580°C/10hrs) TC piston samples.

6.1 Carbon and nitrogen composition-depth profile simulation

Fick's second law of diffusion is the governing law of the evolution of the nitrogen concentration during the ferritic nitrocarburizing process:

$$\frac{\partial c}{\partial t} = D \left(\frac{\partial^2 c}{\partial x^2} + \frac{\partial^2 c}{\partial y^2} + \frac{\partial^2 c}{\partial z^2} \right) + \frac{\partial D}{\partial c} \left(\frac{\partial c}{\partial x} + \frac{\partial c}{\partial y} + \frac{\partial c}{\partial z} \right) \quad (6.1)$$

where c denotes the element composition, t is the diffusion time, D is the diffusion coefficient, x , y and z are the spatial coordinates. In the considered system, the diffusion coefficient is assumed constant (independent of element composition) within the same

phase region (ϵ , γ' and α) such that $\frac{\partial D}{\partial c} = 0$. In addition, the thickness of the system (along the x axis) is much smaller than any of the other two dimensions $\frac{\partial^2 c}{\partial x^2} \gg \frac{\partial^2 c}{\partial y^2}, \frac{\partial^2 c}{\partial z^2}$. Therefore, the final diffusion equation that was used to calculate the composition profile is reduced to:

$$\frac{\partial c}{\partial t} = D \frac{\partial^2 c}{\partial x^2} \quad (6.2)$$

The composition-depth profile simulations are developed using MATLAB, in which the governing partial differential equations are converted into a set of finite difference equations. An explicit time integration scheme along with finite centered difference discretization is used for solving the Equation (6.2) to calculate the nitrogen composition-depth profile. The following boundary and initial conditions were applied to the model:

$$c(x = 0, t) = 8 \text{ wt.}\% \quad (6.3)$$

$$c(x = x_n, t) = 8 \text{ wt.}\% \quad (6.4)$$

$$c(x, 0) = 0 \quad (6.5)$$

In the present work, $x_n = 0.0028$ m (thickness of torque converter piston). The simulation procedure takes part in the following manner. First, the initial composition of nitrogen is stated explicitly. By utilizing the assigned diffusion coefficients and boundary conditions, new concentration terms are then calculated based on the known ones. Finally, growth of the phases and their contribution to distortion are predicted. N composition-depth profiles for the nitrocarburized treatments were generated by considering ϵ , γ' and α as separate layers. Diffusion coefficients for nitrogen in ϵ , γ' and α , phases are given in Equations 6.6, 6.7 and 6.8 [71, 92, 93]:

$$D_N^\varepsilon = 0.227 \times 10^{-4} e^{\left(\frac{-147600}{RT}\right)} \quad \text{m}^2/\text{s} \quad (6.6)$$

$$D_N^{\gamma'} = e^{\left(\left(\frac{-73274}{RT}\right) - 18.775\right)} \quad \text{m}^2/\text{s} \quad (6.7)$$

$$D_N^\alpha = 4.67 \times 10^{-8} e^{\left(\frac{-75150}{RT}\right)} \quad \text{m}^2/\text{s} \quad (6.8)$$

where $R = 8.32 \text{ J/mol K}$ and T is the heat treatment temperature in Kelvin. The above three equations ((6.6), (6.7) and (6.8)) were used in the numerical model to calculate the nitrogen diffusivities. The developed model simulates the nitrogen composition-depth profiles for samples subjected to ferritic nitrocarburizing (FNC) processes at $580^\circ\text{C}/10\text{hrs}$ and $565^\circ\text{C}/5\text{hrs}$ (see Fig.6.2).

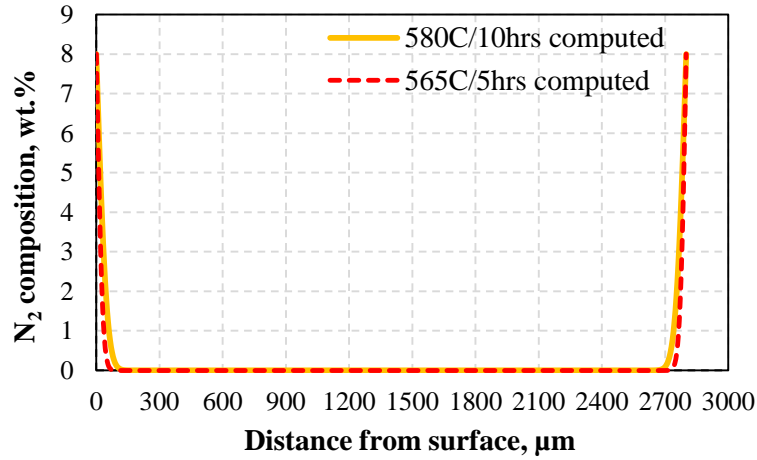


Figure 6.2: Simulated nitrogen composition-depth profiles

Distortion is predicted locally using the following relations:

Distortion due to $\gamma'+\text{N}+\text{C} \rightarrow \varepsilon$ phase transformation,

$$\Delta l_\varepsilon = \frac{\Delta V_{\varepsilon-\gamma'}}{V_\varepsilon} l_\varepsilon \quad (6.9)$$

Distortion due to $\alpha+\text{N}+\text{C} \rightarrow \gamma'$ phase transformation,

$$\Delta l_{\gamma'} = \frac{\Delta V_{\gamma'-\alpha}}{V_{\gamma'}} l_{\gamma'} \quad (6.10)$$

where V_{ϵ} and $V_{\gamma'}$ are the partial molar volumes of ϵ & γ' phases; l_{ϵ} and $l_{\gamma'}$ are the thickness of ϵ and γ' phases. $\Delta V_{\epsilon-\gamma'}$ and $\Delta V_{\gamma'-\alpha}$ are the change in partial molar volumes due to the $\gamma' \rightarrow \epsilon$ and $\alpha \rightarrow \gamma'$ phase transformations. From equations (6.9) and (6.10), it is clear that the thickness of the nitrocarburized layer should be predicted first in order to find the overall local distortion. The thickness of ϵ and γ' phases can be predicted if the composition of nitrogen in ϵ , γ' and α phase regions are known. The threshold nitrogen compositions required to induce the $\gamma' \rightarrow \epsilon$ and $\alpha \rightarrow \gamma'$ phase transformations were taken from the literature (see Table 6.1).

Table 6.1: Composition of nitrogen in ϵ , γ' and α phases [94, 95]

Phases	Nitrogen composition, wt. %
ϵ	> 5.56
γ'	> 0.0876 and ≤ 5.56
α	≤ 0.0876

6.2 Microstructure of torque converter (TC) piston samples

Figures 6.3 and 6.4 shows the microstructure of SAE 1010 torque converter piston sample after vacuum and gas ferritic nitrocarburizing (FNC) treatments. The ϵ compound layer and ferrite grains containing γ' precipitates in the diffusion zone were evident in the micrographs. The micrographs were taken at a magnification of 200X, 500X and 1000X. The compound layer has porous regions at the surface followed by a clean non-porous region (near the compound layer/diffusion zone interface) (see Fig. 6.3(c)).

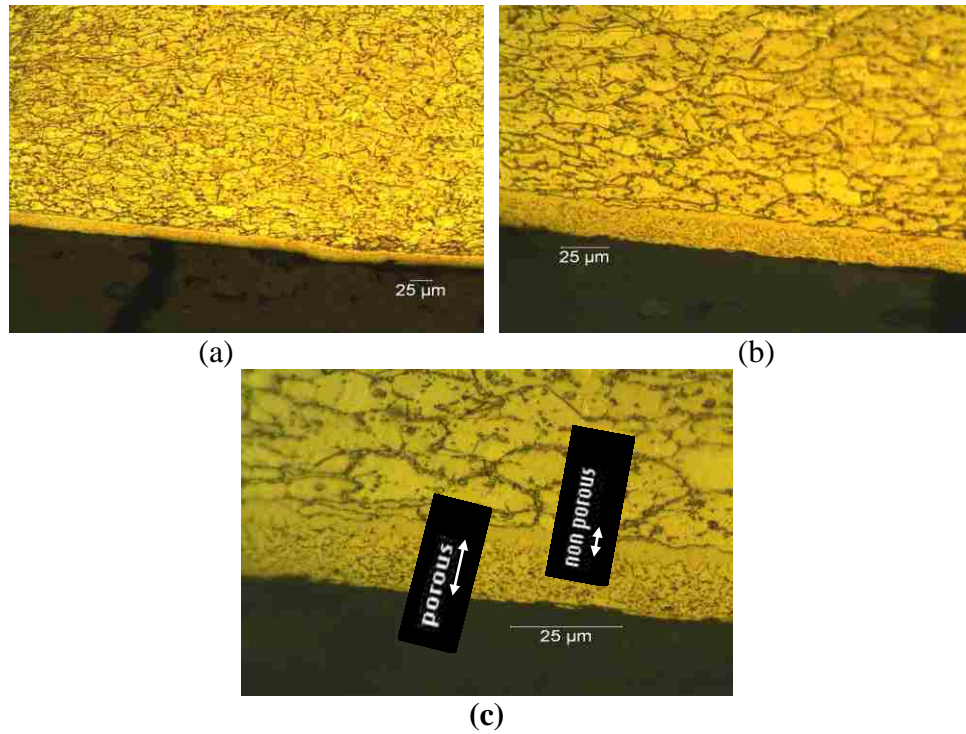


Figure 6.3: (a), (b) and (c) Optical micrographs of SAE 1010 TC piston specimen subjected to vacuum ferritic nitrocarburizing at 580°C/10hrs.

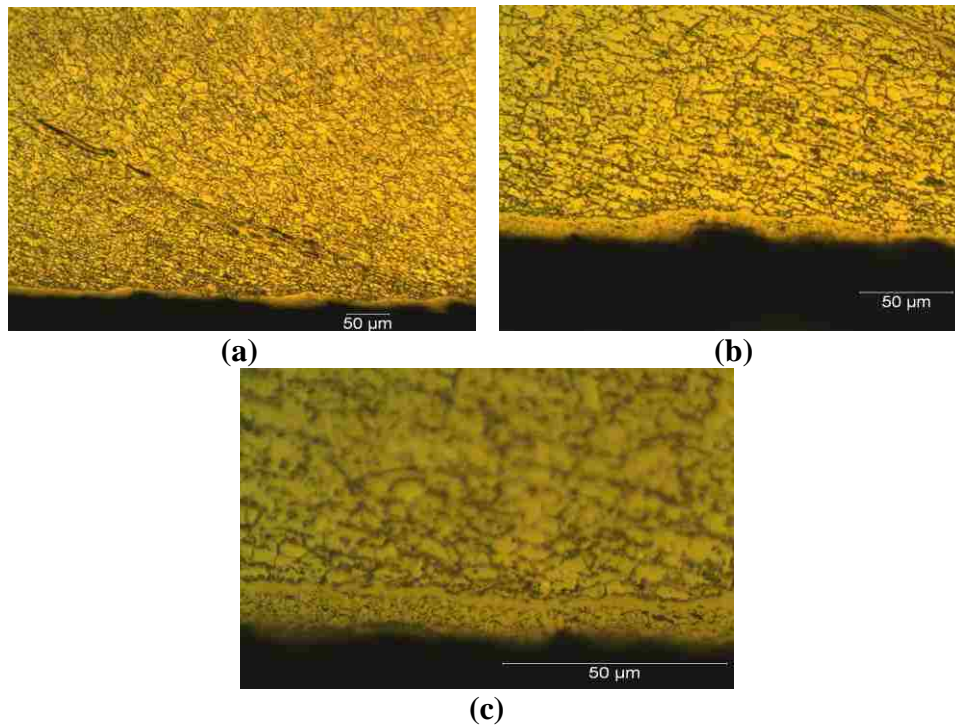


Figure 6.4: (a), (b) and (c) Optical micrographs of SAE 1010 TC piston specimen subjected to gas ferritic nitrocarburizing at 565°C/5hrs.

The compound layer of gas FNC TC piston sample revealed larger pores than the vacuum FNC piston sample. These pores could affect the surface residual stresses. The compound layer of the vacuum treated specimen was intact on the bulk material after polishing. However, the compound layer of gas FNC piston specimen was irregular and some regions were eaten away (probably due to nital etching).

6.3 Composition-depth profile results

Figure 6.5 presents the carbon composition profiles of SAE 1010 TC piston specimens subjected to gas FNC and vacuum FNC treatments. At the surface, the gas ferritic nitrocarburizing (FNC) treatment (565°C/5hrs) has a higher carbon wt. % than the vacuum ferritic nitrocarburizing (FNC) treatment (580°C/10hrs).

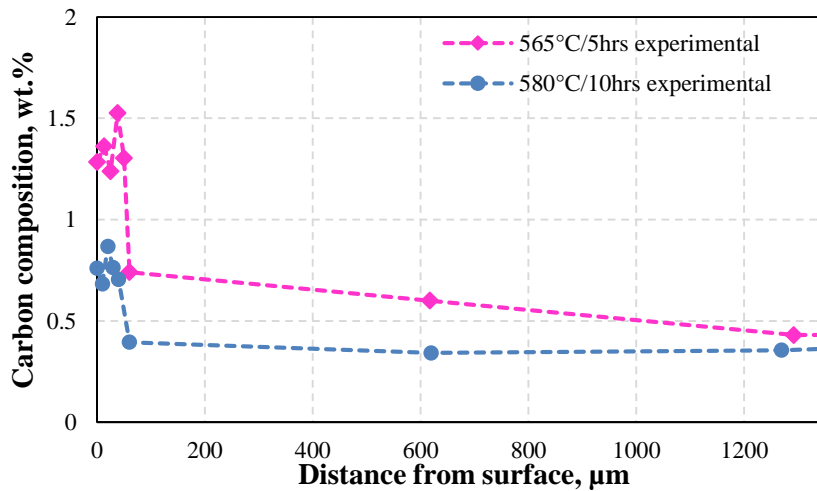


Figure 6.5: Carbon composition depth profile of SAE 1010 steel TC pistons measured using EPMA.

However, the vacuum FNC piston sample has a higher nitrogen wt. % than the gas FNC treated piston (see Fig. 6.6). This observation shows that the nitrogen penetration hinders the carbon penetration during FNC treatment. The predicted nitrogen

composition profiles were validated by the experimental nitrogen profiles in SAE 1010 torque converter (TC) pistons.

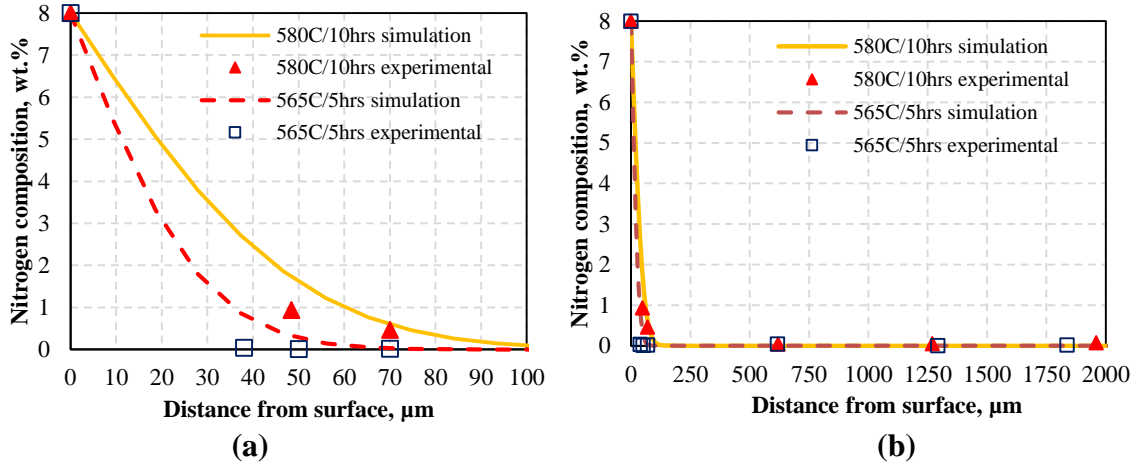


Figure 6.6: Comparison of experimental and simulated nitrogen-profiling results of SAE 1010 nitrocarburized TC pistons ((a) – at the surface, (b) overall).

Table 6.2 lists the predicted phase thicknesses and local distortions due to nitrocarburized phases for the FNC treatments (565°C/5hrs and 580°C/10hrs). The phase thicknesses were first calculated from the simulated N composition profiles using Table 6.1. Using the phase thickness values, the local distortion is then calculated using Equations 6.9 & 6.10.

Table 6.2: Partial molar volume, predicted phase thickness and distortion

Phases	Partial molar volume, $\times 10^{-6} \text{ m}^3/\text{mol}$	$\Delta V_{\varepsilon-\gamma'}$, $\times 10^{-6} \text{ m}^3/\text{mol}$	$\Delta V_{\gamma'-\alpha}$, $\times 10^{-6} \text{ m}^3/\text{mol}$	Predicted phase thickness, μm		Predicted local distortion, μm	
				580°C/10 hrs	565°C/5 hrs	580°C/10 hrs	565°C/5 hrs
ε	8.37	0.15	1.08	16	10	0.29	0.18
γ' from diffusion zone	8.22			84	53	11.04	6.96
α	7.14						
Total						11.33	7.14

The predicted distortion is found to be higher for 580°C/10hrs than 565°C/5hrs. Similarly, the measured distortion for heat treatment (580°C/10hrs) is higher than 565°C/5hrs. Table 6.3 presents the measured ID and OD distortions of nitrocarburized torque converter pistons.

Table 6.3: CMM measured distortion values of SAE 1010 torque converter piston

Heat Treatment	CMM measured distortion	
	Inner diameter (ID), μm	Outer diameter (OD), μm
Gas FNC 565°C/5 hrs	24.64	10.52
Vacuum FNC 580°C/10hrs	35.28	78.38

Although the predicted local distortion cannot really be compared to the inner diameter and outer diameter distortions of TC piston, the local distortion due to ε and γ' phases can be applied to any geometry (shape) whereas the global (experimental) distortion (shown in Table 6.3) is applicable only to a specific geometry such as TC piston.

6.4 Residual stress determination – 1-step nitrocarburizing

The conservation of linear momentum equation, neglecting body forces and inertia forces, can be expressed as:

$$\text{div } \hat{\sigma} = 0 \quad (6.11)$$

where $\hat{\sigma}$ is the Cauchy stress tensor.

$$\text{div} \begin{pmatrix} \sigma_{xx} & \sigma_{yx} & \sigma_{zx} \\ \sigma_{xy} & \sigma_{yy} & \sigma_{zy} \\ \sigma_{xz} & \sigma_{yz} & \sigma_{zz} \end{pmatrix} = 0 \quad (6.12)$$

For 1-dimensional stress state, equation (6.12) is reduced as:

$$\frac{\partial \sigma_{xx}}{\partial x} = 0 \quad (6.13)$$

Integrating the above equation yields:

$$\sigma_{xx} = \text{constant} \quad (6.14)$$

Equation (6.14) indicates that the residual stress is constant within a phase. The residual stresses are predicted using the stress jump at the interface between the two phases: see Equations 6.15 and 6.16 [96]:

$$\Delta \sigma_{\gamma'-\alpha} = \frac{4G}{1 + \frac{4}{3} \cdot G \cdot K} \cdot \varepsilon_{\gamma'} \cdot M \quad (6.15)$$

$$\Delta \sigma_{\varepsilon-\gamma'} = \frac{4G}{1 + \frac{4}{3} \cdot G \cdot K} \cdot \varepsilon_{\varepsilon} \cdot M \quad (6.16)$$

where G is shear modulus, K is the compressibility, $\varepsilon_{\varepsilon}$, $\varepsilon_{\gamma'}$ are the strains due to ε and γ' phases and M is the molar fraction of the precipitates. The molar fraction (M) values are taken from the literature [94]. The compressibility (K) and shear modulus (G) of γ' are 0.00572 GPa⁻¹ and 62.2 GPa [97, 98] respectively. The compressibility (K) and shear modulus (G) of ε are 0.0065 GPa⁻¹ (B=154 GPa; K=1/B) and 78 GPa [99, 100] respectively.

The strain due to change in volume of the phases can be expressed as:

$$\varepsilon_{\gamma'} = \frac{1}{3} \frac{\Delta V_{\gamma'-\alpha}}{V_{\gamma'}} \quad (6.17)$$

$$\varepsilon_{\varepsilon} = \frac{1}{3} \frac{\Delta V_{\varepsilon-\gamma'}}{V_{\varepsilon}} \quad (6.18)$$

Since for the bulk (α phase) $\sigma_{\alpha} = 0$, equation (6.15) yields

$$\text{Surface residual (tensile) stress for } \gamma'\text{-phase, } \sigma_{\gamma'} = 25.9 \text{ MPa} \quad (6.19)$$

Similarly for the ϵ phase,

$$\sigma_{\epsilon} = \sigma_{\gamma'} + \frac{4G}{1 + \frac{4}{3} \cdot G \cdot K} \cdot \epsilon_{\epsilon} \cdot M \quad (6.20)$$

$$\text{Surface residual (tensile) stress for } \epsilon\text{-phase, } \sigma_{\epsilon} = 297.9 \text{ MPa} \quad (6.21)$$

Figure 6.7 shows the predicted residual stress distribution within the nitrocarburized torque converter pistons. Nan et al. [16] have reported the residual stress values of nitrocarburized pistons measured using X-ray diffraction (XRD) technique. The residual stresses were measured at the lockup surface of the piston specimen. The predicted stress value (σ_{ϵ}) slightly overestimates the measured residual stress values (see Table 6.4).

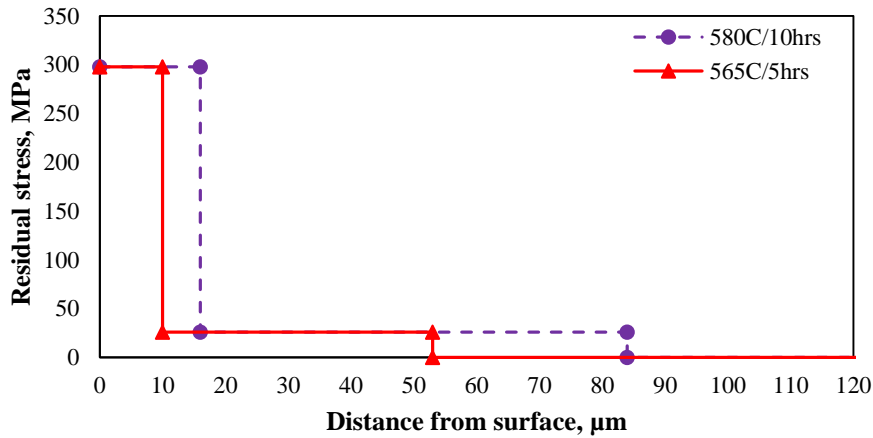


Figure 6.7: Predicted residual stress-depth profiles for FNC heat treatments (580°C/10hrs and 565°C/5hrs).

The presence of porosity in the compound layer affects the residual stress distribution. A heat treatment that produces more pores in the compound layer will have

less tensile stresses. The surface residual stress (tensile) could also be lowered by the presence of γ' phase in the compound layer (see section 6.5).

Table 6.4: Comparison of measured and predicted surface residual stresses of nitrocarburized SAE 1010 torque converter pistons.

Heat treatment	Surface residual stress		
	Measured (MPa)	Predicted (MPa)	
		ϵ	γ' sub-layer
Gas ferritic nitrocarburizing 565°C/5hrs	268 ± 26	297.9	25.9
Vacuum ferritic nitrocarburizing 580°C/10hrs	263 ± 20	297.9	25.9

From Equations 6.15 and 6.16, it is clear that the residual stresses do not have temperature dependence due to FNC treatments. Therefore, the predicted surface residual stresses associated with the Gas FNC and vacuum FNC treatments remains the same.

6.5 N composition-depth profile model for two-step nitrocarburizing treatments

The microstructure of 1-step nitrocarburizing treatment produces a single phase (ϵ -Fe₂₋₃ (C, N)) compound layer and diffusion zone containing γ' phase. The surface residual stresses (tensile) for vacuum ferritic nitrocarburizing (580°C/10hrs) and gas ferritic nitrocarburizing (565°C/5hrs) treatments were 263±20 MPa and 268±26 MPa respectively [16]. In order to further reduce the tensile residual stresses and also to improve the nitrocarburized surface quality, 2-step nitrocarburizing treatments are introduced in this work. This 2-step treatment can potentially reduce the tensile stress at the steel surface due to the additional γ' phase (Fe₄N). The phase sequence of the 2-step nitrocarburizing treatment will be $\gamma' / \epsilon / \gamma'_{diff.zone} / \alpha$ whereas the phase sequence of 1-step

nitrocarburizing is $\varepsilon / \gamma' / \alpha$. Based on the N profile model for the 1-step nitrocarburizing process (refer to section 6.1), the nitrogen composition profiles of 12 different 2-step heat treatment conditions are simulated in this study.

Table 6.5 lists the heat treatment conditions and nitrogen compositions modeled to produce a two-phase (γ' and ε) compound layer. The heat treatment conditions were designed in four batches (ABC;DEF;GHI;JKL). In the first batch, the 1st step process temperature was varied from 595°C to 565°C. Then the 2nd step process temperature was raised by 50°C for heat treatments D, E and F. The 1st step nitrogen compositions of heat treatments G, H and I was decreased from 8 to 7 wt. %. Finally, the process times were increased from 3.6hrs to 10hrs and 1.4hrs to 2.7hrs for heat treatments J, K and L. The parameters involved in heat treatments 'A' to 'L' were chosen to produce the same level of distortion as 1-step nitrocarburizing but lowers the surface residual stresses.

The N composition-depth profile simulation procedure for 2-step nitrocarburizing treatment was performed in two stages. The first stage simulates the step 1 with a nitrogen intake composition of 7 or 8 wt. % and the second stage reproduced the step 2 (Table 6.5) with a nitrogen composition of 3 wt. %. Fick's second law of diffusion (Eqn. (6.2)) was again used to calculate the composition-depth profiles using the explicit time integration scheme with finite centered difference discretization.

Table 6.5: Simulated two step heat treatment conditions and N compositions

Heat treatment	Step number	Process temperature/time	Nitrogen composition (wt. %)
A	1	595°C/3.6hrs +	8%
	2	427°C/1.4hrs	3%
B	1	580°C/3.6hrs +	8%
	2	427°C/1.4hrs	3%
C	1	565°C/3.6hrs +	8%
	2	427°C/1.4hrs	3%
D	1	595°C/3.6hrs +	8%
	2	477°C/1.4hrs	3%
E	1	580°C/3.6hrs +	8%
	2	477°C/1.4hrs	3%
F	1	565°C/3.6hrs +	8%
	2	477°C/1.4hrs	3%
G	1	595°C/3.6hrs +	7%
	2	427°C/1.4hrs	3%
H	1	580°C/3.6hrs +	7%
	2	427°C/1.4hrs	3%
I	1	565°C/3.6hrs +	7%
	2	427°C/1.4hrs	3%
J	1	595°C/ 10hrs +	8%
	2	427°C/ 2.7hrs	3%
K	1	580°C/ 10hrs +	8%
	2	427°C/ 2.7hrs	3%
L	1	565°C/ 10hrs +	8%
	2	427°C/ 2.7hrs	3%

The following boundary and initial conditions were applied to the model: during the first step nitrocarburizing treatment time (t1), the composition of nitrogen was applied

as $c(x=0, t_1) = 8$ (wt. %). At the start of t_2 (2nd step time) the N composition was dropped to 3 (wt. %), so the N composition was given as $c(x=0, t_2) = 3$ (wt. %). Similarly, the other end of the specimen's N compositions were expressed as: $c(x=x_n, t_1) = 8$ wt. % (step 1), $c(x=x_n, t_2) = 3$ wt. % (step 2). The model was applied to SAE 1010 steel torque converter (TC) piston. The thickness of the SAE 1010 TC piston specimen used was 0.0028m (x_n). The initial composition of nitrogen in the bulk material is considered to be zero such that $c(x, 0) = 0$.

In order to calculate the distortion due to γ' and ϵ phases, the N composition-depth profiles after 2-step treatments were divided into three separate regions ($\gamma'+\epsilon$, $\gamma'_{\text{diff.zone}}$ and α phases) using the threshold nitrogen compositions (see Table 6.1). The thickness of the γ' , ϵ and $\gamma'_{\text{diff.zone}}$ phases were initially calculated from the N profiles and the distortion due to γ' , ϵ and $\gamma'_{\text{diff.zone}}$ phases were then predicted (refer to Eqns. 6.22, 6.23 and 6.24) assuming the following surface phase transformation sequence: $\alpha \rightarrow \gamma'_{\text{diff.zone}} \rightarrow \epsilon \rightarrow \gamma'$.

6.5.1 Composition-depth profile results – varying the 1st step temperature

The simulated nitrogen composition profiles of the first heat treatment batch (A, B and C) are shown in Figures 6.8, 6.9 and 6.10. A general decreasing nitrogen penetration was observed with the decrease in 1st step temperature.

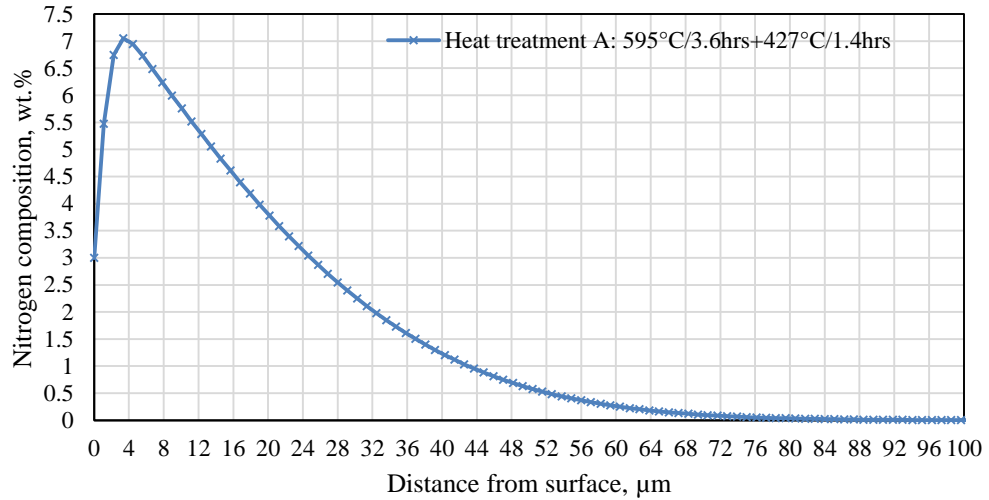


Figure 6.8: Simulated nitrogen composition-depth profile due to 2-step nitrocarburizing process ‘A’ (595°C / 3.6 hrs / 8% + 427°C / 1.4 hrs / 3%).

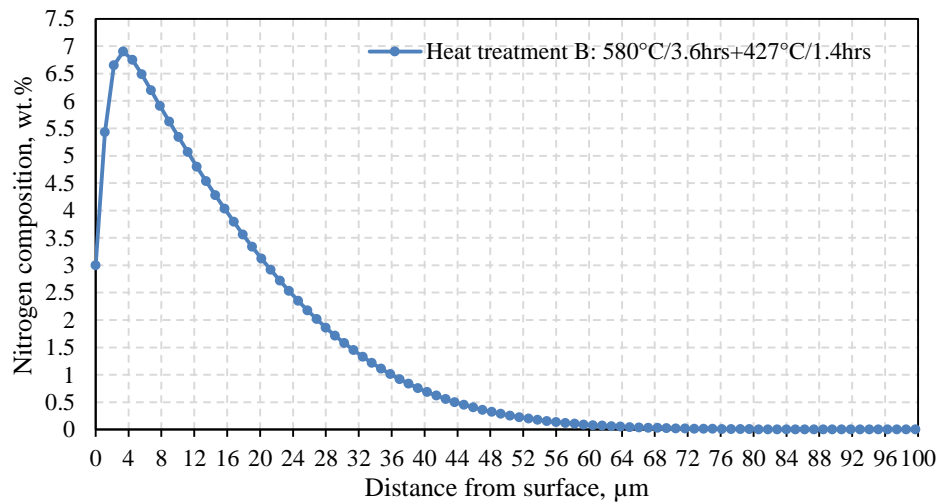


Figure 6.9: Predicted nitrogen composition-depth profile due to two-step nitrocarburizing process ‘B’ (580°C/3.6 hrs/8% + 427°C/1.4 hrs/3%).

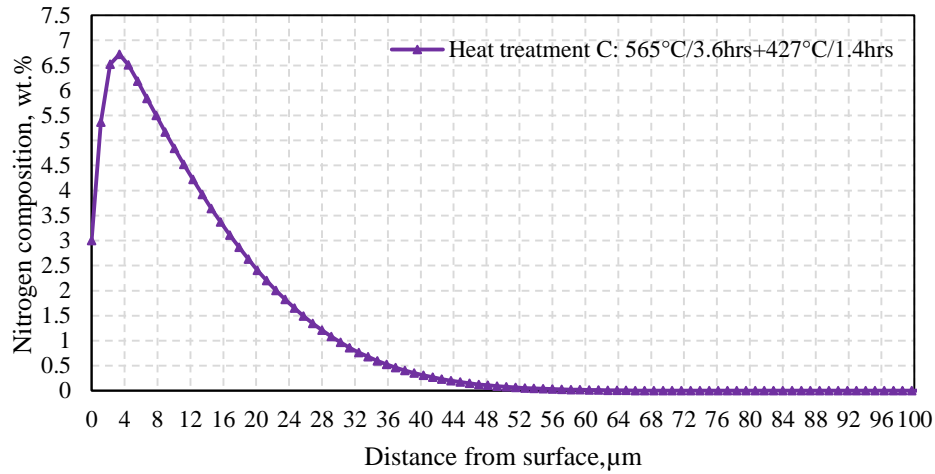


Figure 6.10: Predicted nitrogen composition-depth profile due to two-step nitrocarburizing process ‘C’ (565°C / 3.6 hrs / 8% + 427°C / 1.4 hrs / 3%).

6.5.2 Composition-depth profile results – varying the 2nd step temperature

The heat treatment A and D have same 1st step process temperature but different 2nd step temperature. The nitrogen profile for heat treatment D (with higher 2nd step temperature than B&E) predicted a thicker γ' -phase (purple dotted line) than the heat treatment A (green dotted line) (see Fig. 6.11). However, the heat treatment A produced a thicker ϵ -phase than heat treatment D.

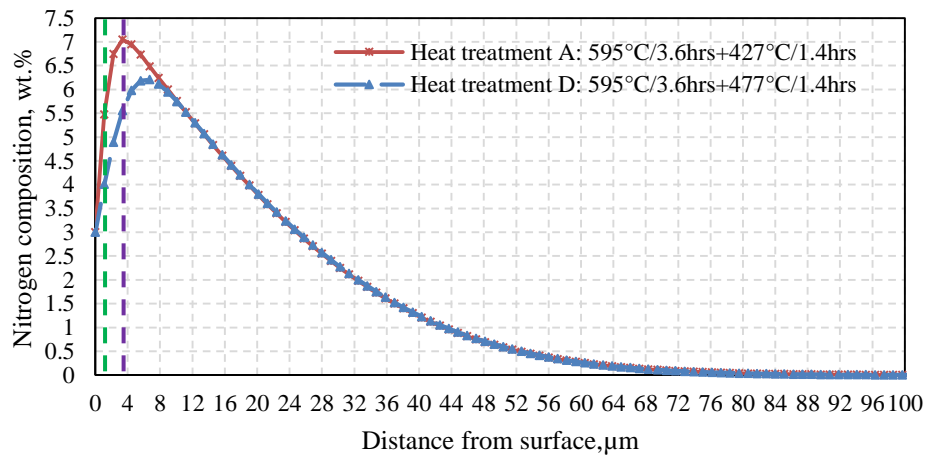


Figure 6.11: Predicted N composition-depth profiles for heat treatment ‘A’ and ‘D’ (595°C/3.6hrs/8wt.%+477°C/1.4hrs/3wt.%).

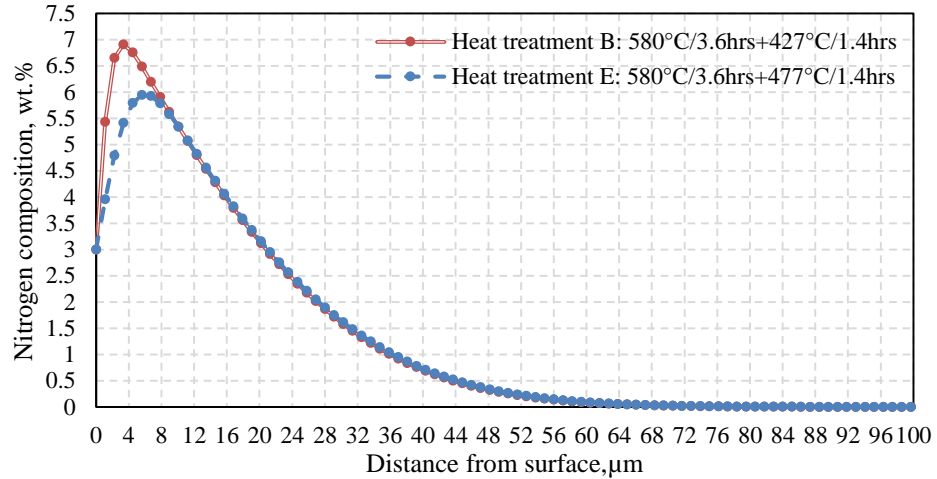


Figure 6.12: Predicted N composition-depth profile for heat treatment ‘B’ and ‘E’ (580°C/3.6hrs/8wt.%+477°C/1.4hrs/3wt.%).

Similar results were obtained for heat treatments B, E and C, F (Figs. 6.12 and 6.13). The higher 2nd step temperature in heat treatments E and F resulted in a thicker γ' -phase and a thinner ϵ -phase than heat treatments B and C. The decrease in nitrogen wt. % are similar for both the set of heat treatments.

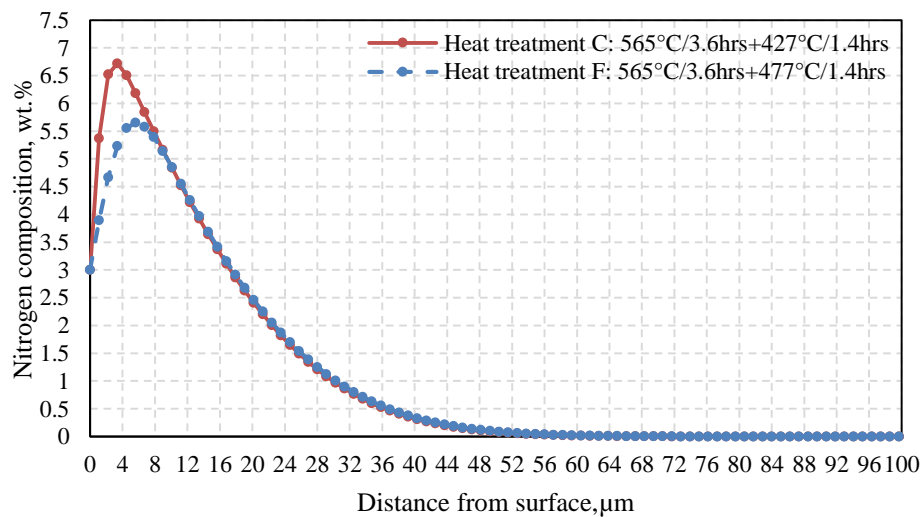
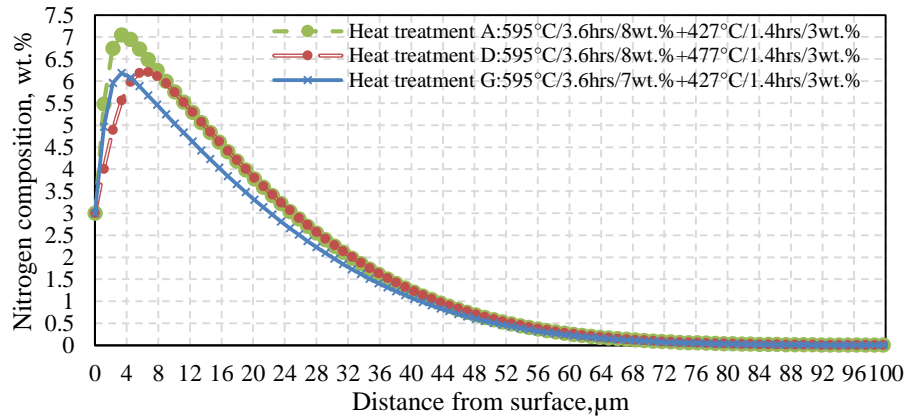


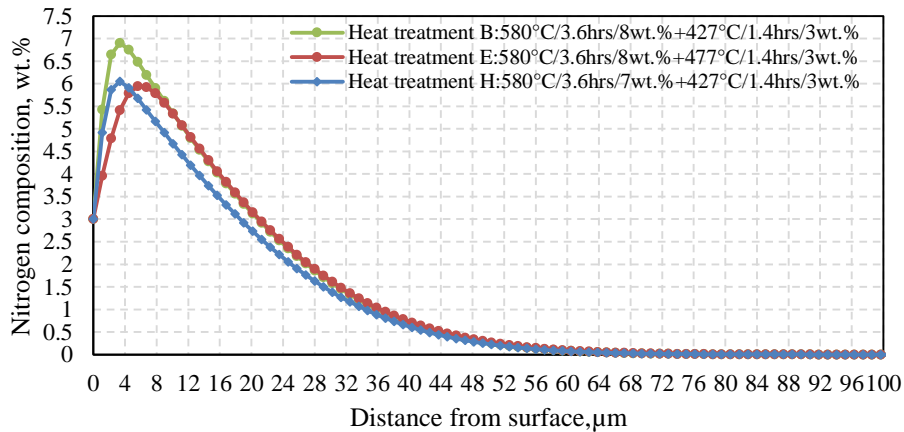
Figure 6.13: Predicted N composition-depth profile for heat treatment ‘C’ and ‘F’ (565°C/3.6hrs/8wt.%+477°C/1.4hrs/3wt.%).

6.5.3 Composition-depth profile results – varying the 1st step N wt. %

The third batch of heat treatments G, H and I involves changing the nitrogen composition (from 8 to 7 wt. %) of the 1st step nitrocarburizing treatment. Decreasing the N composition (from 8 to 7 wt. %) resulted in the smallest compound layer thickness compared to the other heat treatments. The heat treatment I has the lowest $\gamma'_{\text{diff.zone}}$ thickness in the diffusion zone; therefore it results in lower distortion than for heat treatments G and H. Figures 6.14 (a & b) and 6.15 compare the simulated composition-depth profiles for heat treatments G, H and I with A&D, B&E and C&F.



(a)



(b)

Figure 6.14: Predicted N composition-depth profiles for heat treatment ‘G’ (595°C/3.6hrs/7wt.%+427°C/1.4hrs/3wt.%) and heat treatment ‘H’ (580°C/3.6hrs/7wt.%+427°C/1.4hrs/3wt.%).

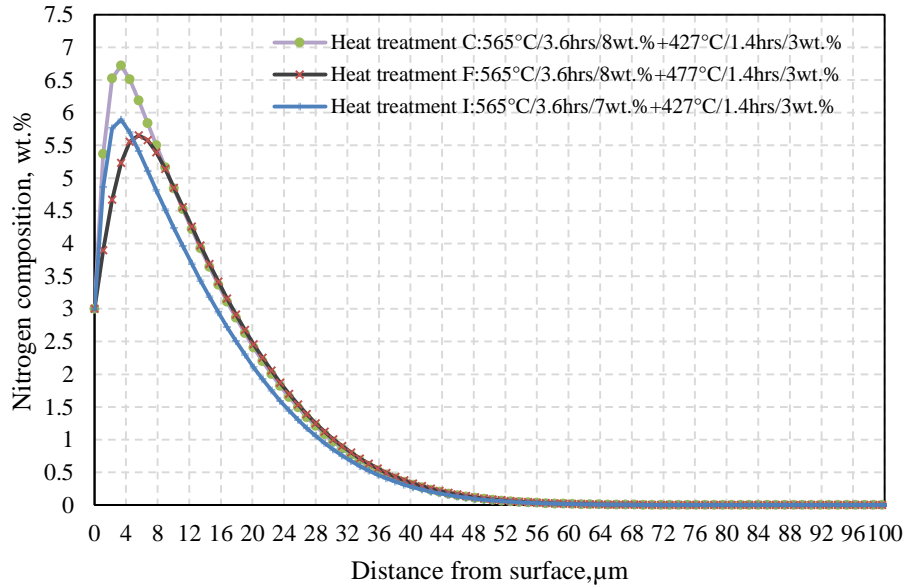


Figure 6.15: Predicted N composition-depth profile for heat treatment ‘I’ (565°C/3.6hrs/7wt.%+427°C/1.4hrs/3wt.%).

6.5.4 Composition-depth profile results – increased process time

Due to longer process times, the nitrogen penetration from the atmosphere to the steel surface was higher for last heat treatment batch J, K and L (see Figs. 6.16, 6.17 and 6.18). After reaching a peak composition in the compound layer region, the heat treatments G, H and I (purple lines) have the highest nitrogen wt. % drop while the heat treatments J, K and L exhibited lowest nitrogen wt. % drop. The decrease in nitrogen intake (8 to 7wt. %) caused the lowest nitrogen penetration in the compound layer and diffusion zone of G, H and I. The nitrogen rate of drop is therefore influenced by the nitrogen intake (from 8 to 7 wt. %) and process times.

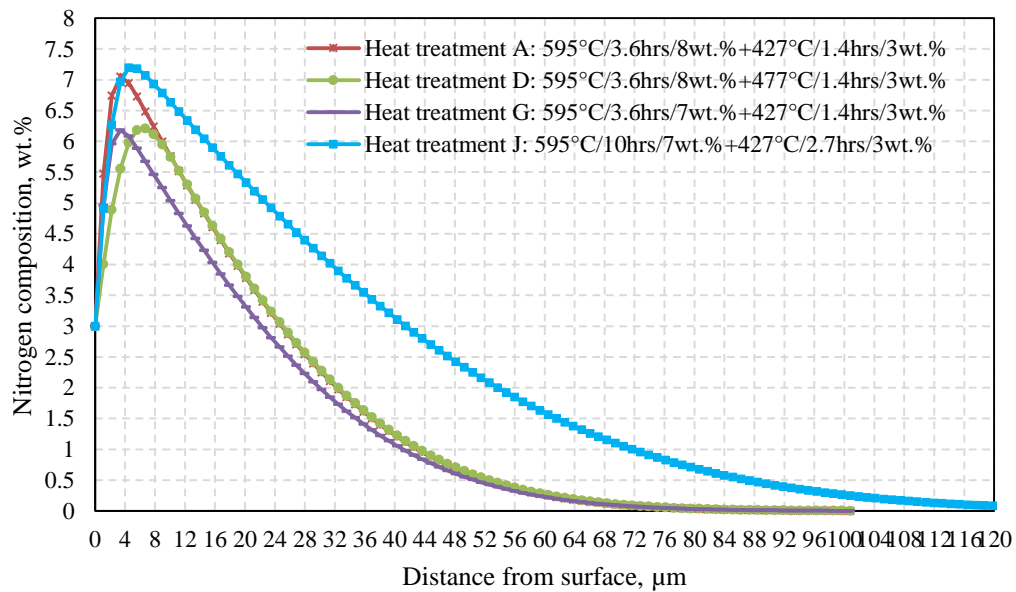


Figure 6.16: Predicted N composition-depth profile for heat treatment ‘J’ (595°C/10hrs/8wt.%+427°C/2.7hrs/3wt.%).

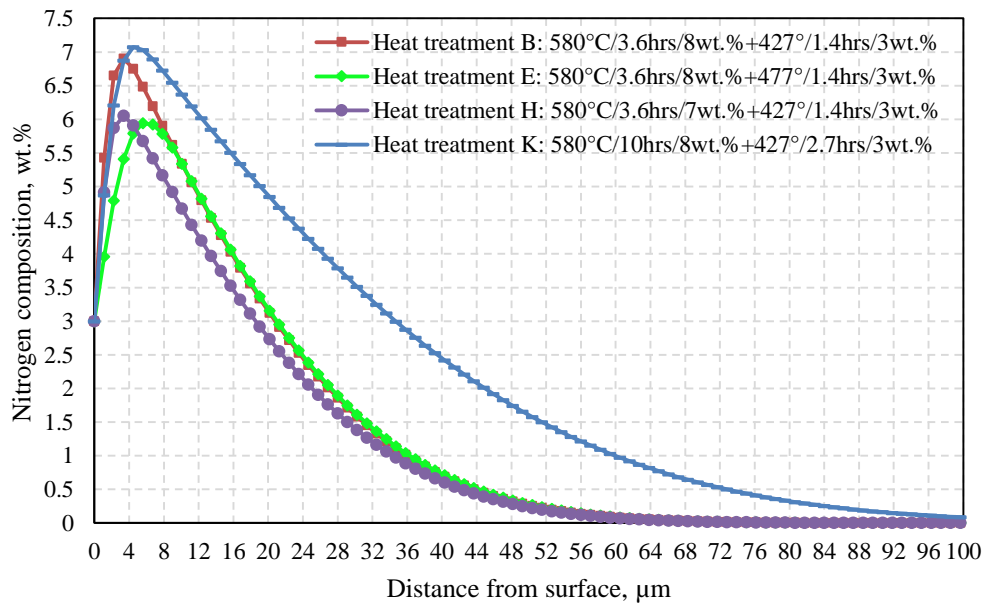


Figure 6.17: Simulated nitrogen composition-depth profile due to two-step nitrocarburizing process (580°C/10hrs/8% + 427°C/2.7hrs/3%).

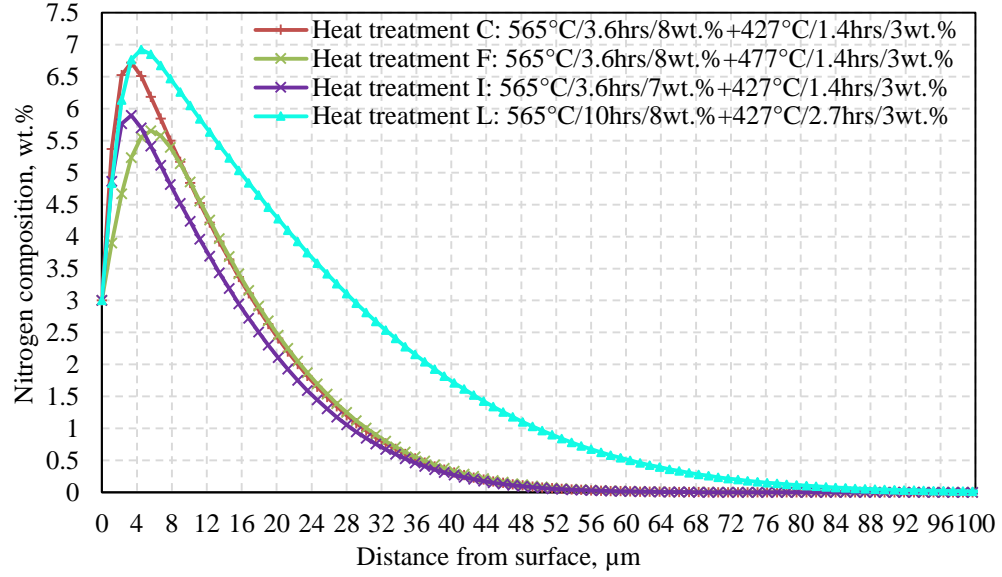


Figure 6.18: Simulated nitrogen composition-depth profile due to two-step nitrocarburizing process (565°C/10hrs/8% + 427°C/2.7hrs/3%).

The distortion due to the two-step nitrocarburizing treatments were predicted as follows:

Distortion due to $\alpha+N+C \rightarrow \gamma'_{\text{diff.zone}}$ phase transformation,

$$\Delta l_{\gamma'} (\text{in diff. zone}) = \frac{\Delta V_{\gamma'-\alpha}}{V_{\gamma'}} I_{\gamma'_{\text{diff. zone}}} \quad (6.22)$$

Distortion due to $\gamma'_{\text{diff.zone}}+N+C \rightarrow \epsilon$ phase transformation,

$$\Delta l_{\epsilon} = \frac{\Delta V_{\epsilon-\gamma'}}{V_{\epsilon}} I_{\epsilon} \quad (6.23)$$

Distortion due to $\epsilon+N+C \rightarrow \gamma'$ phase transformation,

$$\Delta l_{\gamma'} = \frac{\Delta V_{\gamma'-\epsilon}}{V_{\gamma'}} I_{\gamma'} \quad (6.24)$$

where V_{ε} and $V_{\gamma'}$ are the partial molar volumes of ε & γ' phases; l_{ε} and $l_{\gamma'}$ are the thickness of ε and γ' phases. $\Delta V_{\gamma'-\alpha}$, $\Delta V_{\varepsilon-\gamma'}$, and $\Delta V_{\gamma'-\varepsilon}$ are the change in partial molar volumes due to $\alpha \rightarrow \gamma'_{\text{diff.zone}}$, $\gamma'_{\text{diff.zone}} \rightarrow \varepsilon$ and $\varepsilon \rightarrow \gamma'$ phase transformations. The total distortion was calculated by adding together all three distortions ($\Delta l_{\gamma'}$, Δl_{ε} , and $\Delta l_{\gamma' \text{ (in diff. zone)}}$).

Table 6.6 lists the predicted compound layer (CL) thicknesses and distortion due to the CL ($\gamma'+\varepsilon$) & diffusion zone ($\gamma'_{\text{diff.zone}}$). The results showed that the heat treatment J (595°C/10hrs/8wt.%N+427°C/2.7hrs/3wt.%N) has the thickest compound layer whereas the heat treatment I (565°C/3.6hrs/7wt.%N+427°C/1.4hrs/3wt.%N) has the thinnest compound layer. The heat treatments C, F and I with low 1st step process temperature resulted in minimum distortion. Heat treatments J, K and L, with longer nitrocarburizing times, have the highest size distortion.

The local distortion due to γ' in the 2-phase compound layer is almost constant for all series of heat treatments except batch DEF. In the compound layer, the distortion due to ε -phase was higher than the γ' phase. The total distortion was mostly dominated by the $\Delta l_{\gamma'_{\text{diff.zone}}}$, this could be due to a significant volumetric mismatch between the $\gamma'_{\text{diff.zone}}$ and α phases in the diffusion zone.

Table 6.6: Predicted local distortions for two-step nitrocarburizing treatments

Heat treatment	Predicted phase thickness, μm			Predicted local distortion, μm				
	2-phase CL ($\gamma'+\epsilon$)			$l_{\gamma'}^{\text{diff. zone}}$	2-phase CL ($\gamma'+\epsilon$)		$\Delta l_{\gamma'}^{\text{diff. zone}}$	Total
	$l_{\gamma'}$	l_{ϵ}	Total		$\Delta l_{\gamma'}$	Δl_{ϵ}		
A	2	10	12	60	0.036	0.179	7.883	8.098
B	2	8	10	50	0.036	0.143	6.569	6.748
C	2	6	8	42	0.036	0.108	5.518	5.662
D	4	8	12	60	0.073	0.143	7.883	8.099
E	4	6	10	50	0.073	0.108	6.569	6.750
F	4	4	8	43	0.073	0.072	5.649	5.794
G	2	6	8	63	0.036	0.108	8.277	8.421
H	2	5	7	52	0.036	0.089	6.832	6.957
I	2	3	5	44	0.036	0.054	5.781	5.871
J	2	17	19	100	0.036	0.304	13.138	13.478
K	2	14	16	83	0.036	0.251	10.905	11.192
L	2	11	13	70	0.036	0.197	9.197	9.430

6.6 Residual stress determination – 2-step nitrocarburizing

The residual stress distribution for two-step nitrocarburizing treatment was predicted in the same way as the residual stress distribution of 1-step nitrocarburizing treatment (refer section 6.4), except an additional stress jump at the γ'/ϵ interface was included in the calculation. The residual stress distribution was calculated according to the model developed by Kolozsvary et al. [96]:

$$\Delta\sigma_{\gamma'_{\text{diff. zone}}-\alpha} = \frac{4G}{1 + \frac{4}{3} \cdot G \cdot K} \cdot \varepsilon_{\gamma'} \cdot M \quad (6.25)$$

$$\Delta\sigma_{\varepsilon-\gamma'} = \frac{4G}{1 + \frac{4}{3} \cdot G \cdot K} \cdot \varepsilon_{\varepsilon} \cdot M \quad (6.26)$$

$$\Delta\sigma_{\gamma'-\varepsilon} = \frac{4G}{1 + \frac{4}{3} \cdot G \cdot K} \cdot \varepsilon_{\gamma'} \cdot M \quad (6.27)$$

The residual stress within the compound layer is constant (Eqn. 6.14), similarly the residual stress values do not vary for diffusion zone and bulk material. Since the stress is zero for bulk phase (α), the residual stress for $\gamma'_{\text{diff. zone}}$ is initially calculated from Equation 6.25. Using the $\gamma'_{\text{diff. zone}}$ stress, the residual stress due to ε -phase is then calculated from Equation 6.26. The residual stress for γ' is finally calculated from the stress due to ε phase (Eqn. 6.27).

Two-step nitrocarburizing model results in lower surface (tensile) residual stress when compared to the surface residual stress in single-step nitrocarburizing process. The surface residual stress (γ') was found to be 25.9 MPa and the residual stress of ε was 297.9 MPa. The residual stress for $\gamma'_{\text{diff. zone}}$ (in the diffusion zone) was 25.9 MPa. Figure 6.19 presents the residual stress distribution for 2-step nitrocarburizing treatments C, D and J. The residual stress distribution changes with the change in compound layer thicknesses but the pattern remains the same for all heat treatments.

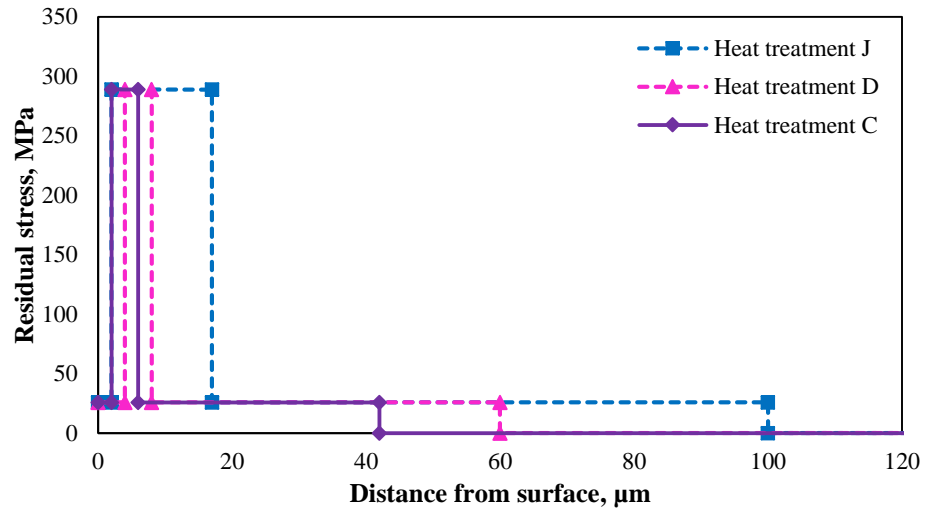


Figure 6.19: Residual stress distribution due to 2-step nitrocarburizing process.

CHAPTER 7 CONCLUSIONS AND FUTURE WORK

This dissertation presents the FEM simulation results for nitrocarburized Navy C-rings and torque converter piston specimens. The study examined the effect of geometry, heat treatment and nitrogen composition on the distortion of nitrocarburized SAE 1010 plain carbon steel. The developed FEM models can predict the small distortions associated with the nitrocarburizing treatment.

Using finite difference method, N profile simulation models were then developed for 1-step and 2-step nitrocarburizing treatments to calculate the local distortion due to the ϵ and γ' phases.

7.1 Conclusions

The following conclusions were drawn from this study:

- The microstructure for 1-step nitrocarburizing revealed a single phase compound layer (ϵ) followed by diffusion zone containing γ' and core material (phase sequence: $\epsilon / \gamma' / \alpha$). The microstructure of the nitrocarburized surface revealed porosity in the compound layer. The residual stress of the ϵ -phase was reported to be tensile for SAE 1010 Navy C-rings and torque converter piston specimens. The FNC process should properly balance the surface residual stress and distortion so that the surface characteristics remains unaltered with the heat treatment that produces minimum distortion.
- The microstructure for 1-step nitrocarburizing also revealed porosity in the compound layer. The porosity in the compound layer will also affect the surface residual stresses.

- Coupled thermo-elastic FEM models were developed to predict the distortion in C-rings and torque converter pistons. The computed values of ID, OD and GW distortions underestimates the measured ID,OD and GW distortions of SAE 1010 C-rings and torque converter pistons.
- Based on the obtained distortions, the thickness of the C-ring probe becomes an important factor in comparing the distortions in the C-rings with those in an actual component (TC piston). For specimen C1 (19mm thick), the nitrocarburized layer in the FEM model has no significant effect on distortion leading to high error. One possible reason for this effect is the heat treatment induced bulk modification along with the intended surface modification. For thinner samples like torque converter (TC) piston and C3 (Navy C-ring) specimens, the model seems to compare favorably with the measured values because the nitrocarburized volume (smaller V/V_N ratio) is dominant over the bulk material volume. The reduction of the bulk volume to nitrocarburized volume (V/V_N) ratio led to a decrease in ID & GW distortion and an increase in OD distortion.
- The predicted error is high, because the diffusion zone and quantification of bulk phases are not included in the FEM models of C-rings and TC pistons.
- The gap width (GW) distortion profiles of the C-rings were similar in both experimental and numerical methods as the C-ring gap tends to contract after heat treatment. The gap width of C2 specimen shrank more than C1 and C3 specimens. By comparing the measured and predicted GW distortions (at three different locations: top, middle, & bottom), it was found that the GW relative error varied from 10% to 330%.

- The measured OD distortion of C-rings (OD expanded after FNC) behaved differently than the TC pistons (OD contracted after FNC).
- Although the C-ring acts as a probe to examine the heat treatment stability, the geometry of C-rings should be carefully selected to match the actual component of interest for better distortion comparison.
- A composition-depth profile model was developed for predicting the local distortion due to the ϵ , γ' phases. The measured and predicted nitrogen composition-depth profiles of torque converter pistons were successfully validated. The measured distortions are calculated from the change in specimen dimensions and are therefore restricted to a specific geometry. But the local distortion, estimated from the composition profile model, is not restricted to any particular material geometries such as C-rings or TC pistons. The local distortion model also helped to better understand the distortion behavior caused by the nitrocarburizing treatment.
- The residual stress distributions due to 1-step nitrocarburizing treatments were successfully developed. Although the stress distributions slightly change with the phase thickness values, the trend profile is similar for 580°C/10hrs and 565°C/5hrs FNC treatments. The predicted surface (tensile) residual stress ($\sigma_{\epsilon} = 297.9$ MPa) was found to be in close agreement with the experimentally determined values (242-294 MPa).
- Using the composition-depth profile model, the nitrogen composition-depth profiles for 2-step nitrocarburizing treatments were optimized to further reduce the tensile stresses and distortion. The nitrogen composition range for 2-step

nitrocarburizing revealed a two-phase (γ' and ϵ) region in the compound layer. The predicted distortion results showed that the diffusion zone in nitrocarburized plain carbon steels play a major role in minimizing distortion. This could be due to a significant volumetric mismatch between the $\gamma'_{\text{diff.zone}}$ and α phases in the diffusion zone. The predicted residual stress (tensile) distribution showed a notable stress reduction at the surface due to an additional γ' phase in the compound layer, which in fact can result in better fatigue life.

7.2 Major advances

- Use of Navy C-rings: consideration of V/V_N ratio with respect to the size of C-ring and actual component.
- Two-step nitrocarburizing process to obtain γ' -Fe₄N phase at the surface and reduce tensile residual stress.

Potential routes for obtaining desired microstructure

- $\gamma' / \epsilon / \gamma'_{\text{diff.zone}} / \alpha$ (2-step nitrocarburizing - present work).
- $\gamma' / \epsilon / \alpha$ (1-step nitriding) [101].

7.3 Suggestions for future work

1. In the present work, the heat transfer coefficient was assumed to not vary with temperature. The change in heat transfer coefficient with temperature can be estimated in future to improve the model predictions.
2. Experimental nitrogen composition-depth profiles for 2-step nitrocarburizing treatments can be measured using EPMA to validate the N profile model for 2-step treatments.

3. The effect of porosity on material properties (such as Young's modulus) and residual stress of the compound layer could be studied for different heat treatment conditions.
4. The temperature effects on the material properties (such as $E(T)$, $\sigma(T)$) could be estimated to further refine the input data of the FEM models.

REFERENCES

- [1] Burakowski, T., and Wierzchon, T., 1999, "Formation of technological surface layers," in 'Surface engineering of metals: principles, equipment, technologies', CRC Press LLC, Boca Raton, FL, pp. 235-251.
- [2] Campagna, V., Bowers, R., Northwood, D. O., Sun, X., and Bauerle, P., 2011, "Comparison of carbonitriding and nitrocarburising on size and shape distortion of plain carbon SAE 1010 steel," *Surface Engineering*, 27(2), pp. 86-91.
- [3] Sinha, A. K., 1991, "Defects and Distortion in Heat-Treated Parts," in 'ASM Handbook', Vol.4, Heat Treating, ASM International, Materials Park, OH, pp. 601-619.
- [4] Wolff, M., Böhm, M., Bökenheide, S., and Dalgiç, M., 2012, "Some recent developments in modelling of heat-treatment phenomena in steel within the collaborative research centre SFB 570 "distortion Engineering"," *Materialwissenschaft und Werkstofftechnik*, 43(1-2), pp. 136-142.
- [5] Simsir, C., 2014, "Modeling and simulation of steel heat treatment: prediction of microstructure, distortion, residual stresses, and cracking," in 'ASM Handbook', Vol. 4B, Steel Heat Treating Technologies, ASM International, Materials Park, OH, pp. 409-466.
- [6] Epler, L. J., 2000, "Ferritic nitrocarburizing gears to increase wear resistance and reduce distortion," *Gear Technology*, 17(2), pp. 24-25.
- [7] Bell, T., 1976, "Ferritic nitrocarburizing," *Metals Engineering Quarterly*, 16(2), pp. 1-13.
- [8] Herring, D. H., Otto, F. J., and Specht, F. R., 2012, "Gear Materials and their Heat Treatment," *Industrial Heating*, pp. 77-84.

- [9] Leineweber, A., Gressmann, T., and Mittemeijer, E. J., 2012, "Simultaneous control of the nitrogen and carbon activities during nitrocarburising of iron," *Surface and Coatings Technology*, 206(11–12), pp. 2780-2791.
- [10] Bell, T., Sun, Y., and Suhadi, A., "Environmental and technical aspects of plasma nitrocarburising," *Proc. Second International Symposium on Applied Plasma Science (ISAPS'99)*, 20-24 Sept. 1999, Elsevier, pp. 14-23.
- [11] Mittemeijer, E. J., 2013, "Fundamentals of nitriding and nitrocarburizing," *ASM Handbook, Volume 4A, Steel Heat Treating Fundamentals and Processes*, J. Dossett, and G. E. Totten, eds., ASM International, Materials Park, OH, pp. 619-646.
- [12] Chen, W. L., Wu, C. L., Liu, Z. R., Ni, S., Hong, Y., Zhang, Y., and Chen, J. H., 2013, "Phase transformations in the nitrocarburizing surface of carbon steels revisited by microstructure and property characterizations," *Acta Materialia*, 61(11), pp. 3963-3972.
- [13] Slycke, J., Sproge, L., and Agren, J., 1988, "Nitrocarburizing and the ternary Fe-N-C phase diagram," *Scandinavian Journal of Metallurgy*, 17(3), pp. 122-126.
- [14] Yang, M., and Sisson, R. D., 2013, "Gaseous nitriding process control: Application of customised lehrer diagrams," *International Heat Treatment and Surface Engineering*, 7(4), pp. 164-171.
- [15] Liapina, T., Leineweber, A., and Mittemeijer, E. J., 2003, "Nitrogen redistribution in ϵ/γ' -iron nitride compound layers upon annealing," *Scripta Materialia*, 48(12), pp. 1643-1648.
- [16] Nan, C., 2009, "Ferritic nitrocarburizing process development for minimization of distortion," M.A.Sc Thesis, Mechanical, Materials and Automotive Engineering Department, University of Windsor, Windsor ON.

- [17] Alasaran, A., and Çelik, A., 2001, "Structural characterization of ion-nitrided AISI 5140 low-alloy steel," *Materials Characterization*, 47(3-4), pp. 207-213.
- [18] Fernandes, F. A. P., Neto, A. L., Oliveira, A. M., and Totten, G. E., 2008, "Stainless steel property improvement by ion nitriding and nitrocarburizing," *Heat Treating Progress*, ASM International, Materials Park, OH, p. 41.
- [19] Cherian, K., 2006, "Microwave carburizing shows promise," *Heat Treating Progress*, ASM International, Materials Park, OH, pp. 46-47.
- [20] Pye, D., 2003, *Practical nitriding and ferritic nitrocarburizing*, ASM International, Materials Park, OH, pp. 111-118.
- [21] Aliev, A. A., 2004, "Updating of equipment for thermochemical treatment of steel parts in a fluidized bed," *Met Sci Heat Treat*, 46(11-12), pp. 559-562.
- [22] Schwartz, M., 2011, "New innovative heat treating processes," *Manufacturing, fabrication and environmental safety*, Taylor & Francis Group, LLC, Boca Raton, FL, pp. 483-502.
- [23] Boblet, J., Retrieved from http://www.durferrit.de/media/pdf/Tenifer_QPQ_eng.pdf on April 10, 2015.
- [24] Korwin, M. J., Morawski, C. D., Tymowski, G. J., and Liliental, W. K., 2004, "Design of nitrided and nitrocarburized materials," *Handbook of metallurgical process design*, G. E. Totten, K. Funatani, and L. Xie, eds., Marcel Dekker, Inc., NY, USA, pp. 545-590.
- [25] Jordan, D., 2009, "Vacuum gas-nitriding furnace produces precision nitrided parts," *Heat Treating Progress*, ASM International, Materials Park, OH, pp. 45-48.

- [26] Ericsson, T., 1987, "Residual stresses caused by thermal and thermochemical surface treatments," *Advances in Surface Treatments*, A. Niku-Lari, ed., Pergamon Press, Oxford, England, pp. 87-113.
- [27] Somers, M. A. J., and Mittemeijer, E. J., 1990, "Development and relaxation of stress in surface layers; composition and residual stress profiles in γ' -Fe₄N_{1-x} layers on α -Fe substrates," *Metallurgical Transactions A (Physical Metallurgy and Materials Science)*, 21A(1), pp. 189-204.
- [28] Nan, C., Northwood, D. O., Bowers, R. J., Sun, X., and Bauerle, P., 2009, "Residual stresses and dimensional changes in ferritic nitrocarburized navy C-rings and prototype stamped parts made from SAE 1010 steel," *SAE International Journal of Materials and Manufacturing*, 2(1), pp. 219-233.
- [29] Leskovšek, V., Podgornik, B., and Nolan, D., 2008, "Modelling of residual stress profiles in plasma nitrided tool steel," *Materials Characterization*, 59(4), pp. 454-461.
- [30] Watkins, T. R., England, R. D., Klepser, C., and Jayaraman, N., 2000, "Measurement and analysis of residual stress in ϵ -phase iron nitride layers as a function of depth," *Advances in X-ray Analysis - 49th Denver X-ray Conference*, JCPDS-International Centre for Diffraction Data 2000, Denver, CO, pp. 31-38.
- [31] Fares, M. L., Touhami, M. Z., Belaid, M., and Bruyas, H., 2009, "Surface characteristics analysis of nitrocarburized (Tenifer) and carbonitrided industrial steel AISIO2 types," *Surface and Interface Analysis*, 41(3), pp. 179-186.
- [32] Thomas, D. H., and Bell, T., 1980, "Fatigue behaviour of aged gas-nitrocarburized low-carbon steel," *Metal Science*, 14(2), pp. 73-78.

- [33] Zoch, H. W., 2009, "Distortion engineering: vision or ready to application?," *Materialwissenschaft und Werkstofftechnik*, 40(5-6), pp. 342-348.
- [34] Zoch, H. W., 2012, "Distortion engineering - Interim results after one decade research within the Collaborative Research Center," *Materialwissenschaft und Werkstofftechnik*, 43(1-2), pp. 9-15.
- [35] Holly, M. L., Devoe, L., and Webster, J., 2011, "Ferritic nitrocarburized brake rotors," SAE 2011 World Congress & Exhibition ,New York.
- [36] Brinksmeier, E., Sölter, J., and Grate, C., 2007, "Distortion engineering - identification of causes for dimensional and form deviations of bearing rings," *CIRP Annals - Manufacturing Technology*, 56(1), pp. 109-112.
- [37] French, H. J., 1930, "A study of the quenching of the steels," *Transactions of the American Society for Steel Treating*, 17(6), pp. 798-888.
- [38] Webster, H., and Laird, W. J., 1991, "Martempering of steel," in 'ASM Handbook', Vol. 4, Heat Treating, ASM International, Materials Park, OH, pp. 137-151.
- [39] Leskovsek, V., Licic, B., and Ule, B., "Some aspects of sub-zero tempering at vacuum heat-treatment of hss," *Proc. Heat Treating: Proceedings of the 21st Conference*, November 5, 2001 - November 8, 2001, ASM International, pp. 25-31.
- [40] Bates, C. E., Totten, G. E., and Brennan, R. L., 1991, "Quenching of steel," in 'ASM Handbook', Vol. 4, Heat Treating, ASM International, Materials Park, OH, pp. 67-120.
- [41] Leskovsek, V., and Ule, B., 2002, "Influence of deep cryogenic treatment on microstructure, mechanical properties and dimensional changes of vacuum heat-treated high-speed steel," *Heat Treatment of Metals*, 29(3), pp. 72-76.

- [42] Nan, C., Northwood, D. O., Bowers, R. J., and Sun, X., 2010, "Study on the dimensional changes and residual stresses in carbonitrided and ferritic nitrocarburized SAE 1010 plain carbon steel," *Materials Science Forum*, pp. 829-834.
- [43] Nan, C., Northwood, D. O., Bowers, R. J., and Sun, X., "Distortion in ferritic nitrocarburized SAE 1010 plain carbon steel," *Proc. SEM Annual Conference and Exposition on Experimental and Applied Mechanics 2009*, pp. 1630-1638.
- [44] Nan, C., Northwood, D. O., Bowers, R. J., Sun, X., and Bauerle, P., "The use of navy C-ring specimens to study distortion in ferritic nitrocarburized 1010 steel," *Proc. 9th International Conference on Surface Effects and Contact Mechanics - Computational Methods and Experiments, Contact/Surface 2009, Algarve, 62*, pp. 13-25.
- [45] Leskovsek, V., 1999, "Optimisation of the vacuum heat treatment of high-speed steels," PhD dissertation, University of Zagreb, Zagreb, Croatia.
- [46] Campagna, V., Bowers, R., Northwood, D. O., Sun, X., and Bauerle, P., "The nitrocarburizing of plain carbon steel automotive components," *Proc. 24th ASM International Heat Treating Conference and Exposition*, pp. 239-244.
- [47] Northwood, D. O., He, L., Boyle, E., and Bowers, R., 2007, "Retained austenite - Residual stress - Distortion relationships in carburized SAE 8620 steel," *Materials Science Forum*, 539-543, pp. 4464-4469.
- [48] Boyle, E., Bowers, R., and Northwood, D. O., "The use of navy C-ring specimens to investigate the effects of initial microstructure and heat treatment on the residual stress, retained austenite, and distortion of carburized automotive steels," *Proc. 2007 World Congress, April 16, 2007 - April 19, 2007, SAE International*, pp. 31-39.

- [49] Clark, A., Bowers, R. J., and Northwood, D. O., 2014, "Heat treatment effects on distortion, residual stress, and retained austenite in carburized 4320 steel," *Materials Science Forum*, 783-786, pp. 692-697.
- [50] Campagna, V., Northwood, D. O., Bowers, R., Sun, X., and Bauerle, P., 2009, "The analysis and control of distortion in carbonitrided and nitrocarburized thin-shelled plain carbon steel automotive powertrain components," *Journal of ASTM International*, 6(3), pp. 1-17.
- [51] Boyle, E., Northwood, D. O., Bowers, R., Sun, X., and Bauerle, P., 2009, "Microstructural effects on residual stress, retained austenite, and case depth of carburized automotive steels," *SAE International Journal of Materials and Manufacturing*, 1(1), pp. 697-708.
- [52] Kurowski, P., 1994, "Avoiding pitfalls in FEA," *Machine Design*, pp. 78-86.
- [53] Inoue, T., and Tanaka, K., 1975, "An elastic-plastic stress analysis of quenching when considering a transformation," *International Journal of Mechanical Sciences*, 17(5), pp. 361-367.
- [54] Inoue, T., Arimoto, K., and Ju, D. Y., 1991, 3rd International Conference on 'Residual Stresses', Society of Materials Science, Tokushima, Japan, pp. 226-231.
- [55] Inoue, T., 1996, "Metallo-thermo-mechanics: application to phase transformation incorporated processes," *Transactions of Joining and Welding Research Institute*, 25, pp. 69-87.
- [56] Inoue, T., and Arimoto, K., 1995, "Implementation of program for simulating heat treatment processes and some results," *Industrial Heating*, 62(4), pp. 41-45.

- [57] Inoue, T., and Arimoto, K., 1997, "Development and implementation of CAE system 'HEARTS' for heat treatment simulation based on metallo-thermo-mechanics," *Journal of Materials Engineering and Performance*, 6(1), pp. 51-60.
- [58] Thuvander, A., 2002, "Numerical simulation of gas quenching of tool steels and the influence of hardenability on distortion," 6th International Tooling Conference, Karlstad, Sweden, pp. 625-642.
- [59] Thuvander, A., 1996, "Calculation of distortion of tool steel dies during hardening," *Proceedings of the 2nd International Conference on Quenching and Control of Distortion*, ASM International, Cleveland, Ohio, USA, pp. 297-303.
- [60] da Silva, A. D., Pedrosa, T. A., Gonzalez-Mendez, J. L., Jiang, X., Cetlin, P. R., and Altan, T., 2012, "Distortion in quenching an AISI 4140 C-ring – Predictions and experiments," *Materials & Design*, 42(0), pp. 55-61.
- [61] Hernández-Morales, B., Barba-Méndez, O., Ingalls-Cruz, A., and Barrera-Godínez, J. A., 2005, "Mathematical modelling of temperature and stress evolution during cooling of a stainless steel Navy C-ring probe," *International Journal of Materials and Product Technology*, 24(1-4), pp. 306-318.
- [62] Li, Z., Lynn Ferguson, B., Sun, X., and Bauerle, P., "Experiment and simulation of heat treatment results of C-Ring test specimen," *Proc. ASM Proceedings: Heat Treating*, 2006, pp. 245-252.
- [63] Nicolas, C., Baudouin, C., Leleu, S., Teodorescu, M., and Bigot, R., 2008, "Dimensional control strategy and products distortions identification," *International Journal of Material Forming*, 1(1), pp. 1039-1042.

- [64] Freborg, A., Ferguson, B., and Li, Z., "Predicting distortion and residual stress in a vacuum carburized and gas quenched steel coupon," Proc. Quenching Control and Distortion - Proceedings of the 6th International Quenching and Control of Distortion Conference, Including the 4th International Distortion Engineering Conference, 2012, pp. 22-33.
- [65] Li, Z., Ferguson, B. L., and Freborg, A., "Modeling application to reduce distortion of a carburized and quenched steel gear," Proc. Quenching Control and Distortion - Proceedings of the 6th International Quenching and Control of Distortion Conference, Including the 4th International Distortion Engineering Conference, 2012, pp. 200-211.
- [66] Depouhon, P., Sprael, J. M., Mailh, M., and Mermoz, E., 2015, "Modeling of distortions induced by the nitriding process," *Mechanics and Industry*, 16(1).
- [67] Mukai, R., Matsumoto, T., Ju, D. Y., Suzuki, T., Saito, H., and Ito, Y., 2006, "Modeling of numerical simulation and experimental verification for carburizing-nitriding quenching process," *Transactions of Nonferrous Metals Society of China (English Edition)*, 16(SUPPL.), pp. s566-s571.
- [68] Du, H., Somers, M. A. J., and Ågren, J., 2000, "Microstructural and compositional evolution of compound layers during gaseous nitrocarburizing," *Metallurgical and Materials Transactions A: Physical Metallurgy and Materials Science*, 31(1), pp. 195-211.
- [69] Gräfen, W., and Edenhofer, B., 2005, "New developments in thermo-chemical diffusion processes," *Surface and Coatings Technology*, 200(5–6), pp. 1830-1836.
- [70] Yang, M., and Sisson Jr, R. D., 2012, "Modeling the nitriding process of steels," *Advanced Materials and Processes*, 170(7), pp. 33-36.

- [71] Keddam, M., 2007, "Surface modification of the pure iron by the pulse plasma nitriding: Application of a kinetic model," *Materials Science and Engineering: A*, 462(1–2), pp. 169-173.
- [72] Yan, M., Yan, J., and Bell, T., 2000, "Numerical simulation of nitrided layer growth and nitrogen distribution in ϵ -Fe 2-3 N, γ '-Fe 4 N and α -Fe during pulse plasma nitriding of pure iron," *Modelling and Simulation in Materials Science and Engineering*, 8(4), pp. 491-496.
- [73] Gu, X., Michal, G. M., Ernst, F., Kahn, H., and Heuer, A. H., 2014, "Numerical simulations of carbon and nitrogen composition-depth profiles in nitrocarburized austenitic stainless steels," *Metallurgical and Materials Transactions A: Physical Metallurgy and Materials Science*, 45(10), pp. 4268-4279.
- [74] Ozisik, M. N., 1994, *Finite difference methods in heat transfer*, CRC Press LLC, Boca Raton, FL, pp. 118-120.
- [75] Fausett, L. V., 2008, *Applied numerical analysis using MATLAB*, Pearson Education, Inc., Upper Saddle River, NJ, pp. 608-610.
- [76] Moskalioviene, T., Galdikas, A., Riviere, J. P., and Pichon, L., 2011, "Modeling of nitrogen penetration in polycrystalline AISI 316L austenitic stainless steel during plasma nitriding," *Surface and Coatings Technology*, 205(10), pp. 3301-3306.
- [77] Torres, J. L., Chuzhoy, L., Burns, K. W., Meng, C., Krzyaniak, B., Horrocks, S., and El-Darazi, D., "Ferritic nitro-carburizing of ductile iron parts," *Proc. International Surface Engineering Congress - Proceedings of the 1st Congress*, pp. 75-79.

- [78] Depouhon, P., Sprael, J. M., Mailhé, M., and Mermoz, E., 2014, "Mathematical modeling of residual stresses and distortions induced by gas nitriding of 32CrMoV13 steel," *Computational Materials Science*, 82(0), pp. 178-190.
- [79] Prantil, V. C., Callabresi, M. L., Lathrop, J. F., Ramaswamy, G. S., and Lusk, M. T., 2003, "Simulating distortion and residual stresses in carburized thin strips," *Journal of Engineering Materials and Technology, Transactions of the ASME*, 125(2), pp. 116-124.
- [80] Larson, D., 1990, "Finite element analysis of residual stress and distortion in forged and carburized gear steel," M.S Thesis T-3932, Colorado School of Mines, Golden, CO.
- [81] Kurz, S. J. B., Meka, S. R., Schell, N., Ecker, W., Keckes, J., and Mittemeijer, E. J., 2015, "Residual stress and microstructure depth gradients in nitrided iron-based alloys revealed by dynamical cross-sectional transmission X-ray microdiffraction," *Acta Materialia*, 87, pp. 100-110.
- [82] Nan, C., Northwood, D. O., Sun, X., and Bauerle, P., 2008, "TMP Current 254 mm 45 RFE T/C Piston Production Report," University of Windsor, Windsor, ON, pp. 1-12.
- [83] Boyle, E., 2007, "Microstructural effects on the mechanical properties of carburized low-alloy steels," M.A.Sc Thesis, Mechanical, Automotive and Materials Engineering Department, University of Windsor, Windsor ON.
- [84] Retrieved from <http://www.es.utoronto.ca/microprobe> on March 27, 2015.
- [85] Stringfellow, R., 1995, "Prediction and control of heat treat distortion of helicopter gears (final report)," Aviation Applied Technology Directorate, Fort Eustis, VA, p. 192.
- [86] Rothman, M. F., 1988, "High-Temperature Property Data: Ferrous Alloys," ASM International, Materials Park, OH, pp. 2.7-2.8.

- [87] Somers, M. A. J., van der Pers, N. M., Schalkoord, D., and Mittemeijer, E. J., 1989, "Dependence of the lattice parameter of γ' iron nitride, $\text{Fe}_4\text{N}_{1-x}$, on nitrogen content; accuracy of the nitrogen absorption data," *Metallurgical Transactions A (Physical Metallurgy and Materials Science)*, 20A(8), pp. 1533-1539.
- [88] Lyman, T., Boyer, H. E., Unterweiser, P. M., Hontas, J. P., Mehlman, L. R., Carnes, W. J., and Lawton, H., 1964, *Metals Handbook*, American Society for Metals, Metals Park, OH, 2, pp. 52-55.
- [89] Franssen, J. M., and Real, P. V., 2010, "Fire design of steel structures," Wiley-VCH GmbH & Co. KGaA, Weinheim, Germany, p.452.
- [90] Bauccio, M., Harvey, P. D., Boyer, H. E., and Giancoli, D. C., 1993, "AISI 1010 steel, cold drawn bar, 19-32mm round or thickness," Retrieved from <http://www.matweb.com/search/datasheet.aspx?MatGUID=4b64586941754ec2a4a8ef0fd e2299db> on May 20, 2015.
- [91] "Young's modulus of elasticity for metals and alloys," Retrieved from http://www.engineeringtoolbox.com/young-modulus-d_773.html on May 20, 2015.
- [92] Lakhtin, Y. M., and Kogan, Y. D., 1976, *Nitriding of Steel*, Mashinostroenie, Moscow.
- [93] Campos, I., Torres, R., Bautista, O., Ramírez, G., and Zuñiga, L., 2005, "Evaluation of the diffusion coefficient of nitrogen in $\text{Fe}_4\text{N}_{1-x}$ nitride layers during microwave post-discharge nitriding," *Applied Surface Science*, 249(1-4), pp. 54-59.
- [94] Du, H., and ågren, J., 1996, "Theoretical treatment of nitriding and nitrocarburizing of iron," *Metall and Mat Trans A*, 27(4), pp. 1073-1080.

- [95] Jordan, D., 2010, "Controlling compound (white) layer formation during vacuum gas nitriding," Retrieved from <http://solaratm.com/white-layer-formation-paper.pdf> on April 09, 2015.
- [96] Kolozsvary, Z., Plasmatern, S. C., and Mures-Tg, 2002, "Residual stresses in nitriding," Handbook of residual stress and deformation of steel, G. E. Totten, M. Howes, and T. Inoue, eds., ASM International, Materials Park, Ohio, USA, pp. 209-219.
- [97] Kong, Y., Diao, X., Yang, J., and Li, F., 1997, "Evaluation of the compressibility of iron-nickel nitrides," Journal of Magnetism and Magnetic Materials, 172(1–2), pp. L15-L18.
- [98] Gressmann, T., 2007, "Fe-C and Fe-N compound layer: growth kinetics and microstructure," PhD dissertation, Max Planck Institute for Metals Research, Institute for Materials Science, University of Stuttgart, Germany.
- [99] Yin, W., Lei, L., Jiang, X., Liu, P., Liu, F., Li, Y., Peng, F., and He, D., 2014, "High pressure synthesis and properties studies on spherical bulk ϵ -Fe₃N," High Pressure Research, 34(3), pp. 317-326.
- [100] Niewa, R., Rau, D., Wosylus, A., Meier, K., Hanfland, M., Wessel, M., Dronskowski, R., Dzivenko, D. A., Riedel, R., and Schwarz, U., 2009, "High-pressure, high-temperature single-crystal growth, ab initio electronic structure calculations, and equation of state of ϵ -Fe₃N_{1+x}," Chemistry of Materials, 21(2), pp. 392-398.
- [101] Maeda, S., Kobayashi, A., Shimizu, Y., Kanayama, M., Yuya, M., and Imataka, H., 2015, "Development of γ' -Fe₄N Phase Control Technology and Low-Carbon Alloy Steel for High-Strength Nitrided Gear," SAE International Journal of Materials and Manufacturing, 8(3), pp. doi:10.4271/2015-4201-0519.

PUBLICATIONS

1. Manivannan, M., Stoilov, V., and Northwood, D.O., 2015, "Ferritic nitrocarburizing of SAE 1010 plain carbon steel parts," SAE International Journal of Materials and Manufacturing, 8(2), 482-486.
2. Manivannan, M., Stoilov, V., and Northwood, D.O., 2015, "Numerical model of the ferritic nitrocarburizing of SAE 1010 plain carbon steel," European Conference on Heat Treatment 2015 & 22nd IFHTSE Congress, May 20-22, 2015, Venice, Italy (accepted for presentation).
3. Manivannan, M., Northwood, D.O., and Stoilov, V., 2014, "Use of Navy C-rings to study and predict distortion in heat treated components: experimental measurements and computer modelling," International Heat Treatment and Surface Engineering, 8(4), 168-175.
4. Manivannan, M., Stoilov, V., and Northwood, D.O., 2014, "Finite element simulations of geometric distortions in ferritic nitrocarburized SAE 1010 plain carbon steel," Proceedings of the 5th International Conference on Thermal Process Modeling and Computer Simulation," 139-144, June 16, 2014, Orlando, FL, USA.

APPENDICES

Appendix A

An explicit time integration scheme was used to solve the finite difference simulations involving the one-dimensional diffusion equation for 1-step and 2-step ferritic nitrocarburizing treatments in TC pistons.

A.1 MATLAB program files for a single-step nitrocarburizing treatment

```
function [x,z]=heat(T,n,m,L)
h=L/n;
k=T/m;
x=0:h:L;
t=0:k:T;
u(1:n+1,1)=fx(x)'; % initial condition
u(1,1:m+1)=g0(t);
u(n+1,1:m+1)=g1(t); % boundary conditions
for j=1:m
c=Dcoef(u,j);
r=c*k/h^2;
s=1-2*r;
r1=r(1:n-1);
r2=r(3:n+1);
s1=s(2:n);
u(2:n,j+1)=r1.*u(1:n-1,j)+s1.*u(2:n,j)+r2.*u(3:n+1,j);
end
z=u;

% boundary conditions
function g=g1(t)
```



```

g=8;
end

function g=g0(t)
g=8;
end

% initial condition (N composition)
function f=fx(x)
f=0;
end

% calculation of N diffusivities
function c=Dcoef(u_conc,n)
[m,k]=size(u_conc);
c=zeros(m,1);
T=838.15;
    for(i=1:m)
        if(u_conc(i,n)>=0)
            if(u_conc(i,n)<=8)
                c(i)=0.227e-4*exp(-147600/(8.32*T));
            elseif(u_conc(i,n)<=5.56)
                c(i)=exp((-73274/(8.32*T))-18.775);
            elseif(u_conc(i,n)<=0.0876)
                c(i)=4.67e-8*exp(-75150/(8.32*T));
            end % if
        end % if
    end %for loop
end %function Dcoef

end

```

```
% Running the heat function file
```

```
clc;
```

```
n=300;m=8000;T=18000;L=0.0028;
```

```
[x1,z1]=heat(T,n,m,L)
```

where n and m represents the total number of spatial and time subdivisions, L represents the thickness of the torque converter piston and T (in the 'heat' file) denotes the total heat treatment time.

A.2 MATLAB program files for a two-step nitrocarburizing treatment

The MATLAB program files of 1-step nitrocarburizing treatment were modified to solve the nitrogen composition-depth profile in 2-step nitrocarburizing treatments:

```
function [distr]=heat_new(t1,T1,T2)
```

```
n=2500;
```

```
m=8000;
```

```
L=0.0028;
```

```
Ttime=45720;
```

```
h=L/n;
```

```
k=Ttime/m;
```

```
x=0:h:L;
```

```
t=0:k:Ttime;
```

```
u(1:n+1,1)=fx(x)'; % initial condition
```

```
u(1,1:m+1)=g0(t,t1);
```

```
u(n+1,1:m+1)=g1(t,t1); % boundary conditions
```

```
for j=1:m
```

```
    c=Dcoef_new(u,j,k,t1,T1,T2);
```

```

r=c*k/h^2;
s=1-2*r;
r1=r(1:n-1);
r2=r(3:n+1);
s1=s(2:n);
u(2:n,j+1)=r1.*u(1:n-1,j)+s1.*u(2:n,j)+r2.*u(3:n+1,j);
end
z=u;

```

% Nitrogen composition (wt. %) input at one end of the TC specimen

```

function g=g1(t,t1)
m=length(t);
for(i=1:m)
    if(t(i)<=t1)
        g(i)=8;
    else
        g(i)=3;
    end
end
end

```

% Nitrogen composition (wt. %) input at the other end of the TC specimen

```

function g=g0(t,t1)
m=length(t);
for(i=1:m)
    if(t(i)<=t1)
        g(i)=8;
    else
        g(i)=3;
    end
end
end

```

```
end
```

```
% Initial composition (wt. %) of nitrogen in the bulk
```

```
function f=fx(x)
```

```
f=0;
```

```
% Nitrogen diffusion coefficients
```

```
function c=Dcoef_new(u_conc,n,k,t1,T1,T2)
```

```
[m,kk]=size(u_conc);
```

```
c=zeros(m,1);
```

```
if(n*k<t1)
```

```
    T=T1;
```

```
else
```

```
    T=T2;
```

```
end
```

```
for(i=1:m)
```

```
    if(u_conc(i,n)>=0)
```

```
        if(u_conc(i,n)<=8)
```

```
            c(i)=0.227e-4*exp(-147600/(8.32*T));
```

```
        elseif(u_conc(i,n)<=5.56)
```

```
            c(i)=exp((-73274/(8.32*T))-18.775);
```

```
        elseif(u_conc(i,n)<=0.0876)
```

```
            c(i)=4.67e-8*exp(-75150/(8.32*T));
```

```
        end
```

```
    end
```

```
end
```

```
% Running the heat_new function file
```

```
clc;
```

```
t1=36000;T1=868.15;T2=700.15;  
[distortion]=heat_new(t1,T1,T2)
```

The heat treatment temperature was reported in Kelvin, where T1 represents the 1-step heat treatment temperature & T2 represents the second step temperature and the heat treatment time was used in seconds (Ttime). The nitrogen composition was used in wt. %.

VITA AUCTORIS

NAME: Madhavan Manivannan

PLACE OF BIRTH: Chennai, India

YEAR OF BIRTH: 1985

EDUCATION: Anna University, B. Tech., (Chemical & Electrochemical Engineering) Chennai, India, 2002-2006

University of Windsor, M.A.Sc., (Engineering Materials) Windsor, ON, 2007-2009

University of Windsor, PhD., (Engineering Materials) Windsor, ON, 2010-2015